Quantum gases are forever:
Achieving continuous Bose-Einstein condensation

ACADEMISCH PROEFSCHRIFT

ter verkrijging van de graad van doctor
aan de Universiteit van Amsterdam
op gezag van de Rector Magnificus
prof. dr. ir. K. I. J. Maex
ten overstaan van een door het College voor Promoties ingestelde
commissie, in het openbaar te verdedigen in de Agnietenkapel
op [to be determined]

door

Rodrigo González Escudero

geboren te Madrid

Promotiecommissie

Promotor	prof. dr.	F.E. Schreck	Universiteit van Amsterdam
Co-promotor	dr.	B.B. Pasquiou	Universiteit van Amsterdam
Overige leden	prof. dr.	W. von Klitzing	Institute of Electronic Structures and Lasers
	prof. dr.	P. van der Straten	Universiteit Utrecht
	prof. dr.	J.S. Caux	Universiteit van Amsterdam
	prof. dr.	J.T.M. Walraven	Universiteit van Amsterdam
	dr.	R. Gerritsma	Universiteit van Amsterdam

Faculteit der Natuurwetenschappen, Wiskunde en Informatica
The author can be reached at rodrigo.g.escudero@gmail.com

Summary

In this thesis, I report on my work, under the supervision of prof. dr Florian Schreck and dr. Benjamin Pasquiou, on the atom laser experiment at the University of Amsterdam. The work presented here revolves around a single theme, the development of new tools to prepare ultracold gases in steady state. Here we reach unprecedented steady-state phase-space densities up to a continuously existing Bose-Einstein condensate, we provide new sources for continuously operating superradiant lasers, and develop tools to manipulate steady-state ultracold gases.

The main scientific goal of this project has been the production of a continuous-wave atom laser. While this goal has not yet been reached, we have realized a critical break-through, the production of a steady-state Bose-Einstein condensate. The experimental developments that allowed us to achieve this long-sought goal can be found in chapter 2 of this thesis. To produce a continuous-wave atom laser one just needs to outcouple the atoms in the condensate. The last months of my PhD work have been devoted to implementing the additional experimental components required to do so. The approach that we have taken and the most recent developments in the experiment are described in the outlook of this thesis (chapter 5). We hope that in short time, our experiment will reach its ultimate goal and produce the first steady-state atom laser.

In chapter 3 we show how to produce a steady-state magneto-optical trap of fermionic strontium atoms operating on a narrow-line transition. This chapter describes the key experimental developments that were required to obtain this result and contains an in-depth characterization of this system. While the core of this chapter is based on a peer-reviewed publication, it also contains additional information that might be useful for those trying to reproduce or expand the work presented here. This chapter represents around a year of work, from experimental development to publication. Triggered by the start of the *iqClock* project, this research aims to help the *iqClock* team in achieving their ultimate goal, the production of a steady-state superradiant laser and it is written with them in mind.

Finally, in chapter 4 we describe a novel laser cooling scheme inspired by a theoretical proposal designed to laser cool (anti)hydrogen. This technique was investigated as a tool to more efficiently slow the atoms in our system. Yet it will undoubtedly prove useful in other situations and it is an additional valuable tool for the atomic physics community.

Samenvatting

In dit proefschrift doe ik verslag van het atoomlaserexperiment dat ik heb gedaan onder supervisie van prof. dr. Florian Schreck en dr. Benjamin Pasquiou aan de Universiteit van Amsterdam. Het hier gepresenteerde werk draait om één thema: de ontwikkeling van nieuwe instrumenten om ultrakoude gassen in een stabiele toestand voor te bereiden. We behalen hier niet eerder vertoonde faseruimtedichtheden in stabiele toestand tot aan een voortdurend bestaand bose-einsteincondensaat, leveren nieuwe bronnen voor continu werkende superstralende lasers, en ontwikkelen instrumenten om ultrakoude gassen in stabiele toestand te manipuleren.

Het voornaamste wetenschappelijke doel van dit project was de productie van een continugolflaser. Hoewel dit doel nog niet is bereikt, hebben we een cruciale doorbraak gerealiseerd: de productie van een bose-einsteincondensaat in stabiele toestand. De experimentele ontwikkelingen die ons in staat stelden om dit langgezochte doel te bereiken, zijn te vinden in hoofdstuk 2 van dit proefschrift. Om een continugolflaser te produceren, hoeft men slechts de atomen in het condensaat te ontkoppelen. De laatste maanden van mijn promotiewerk waren gewijd aan het implementeren van de aanvullende experimentele componenten die daarvoor nodig zijn. Onze aanpak en de meest recente ontwikkelingen in het experiment worden beschreven in de discussie van dit proefschrift (hoofdstuk 5). We hopen dat ons experiment in korte tijd zijn uiteindelijke doel zal bereiken en de eerste atoomlaser in stabiele toestand zal opleveren.

In hoofdstuk 3 laten we zien hoe je een magneto-optische val van fermionische strontiumatomen in stabiele toestand kunt produceren die gebruik maakt van een smalle-lijnovergang. Dit hoofdstuk beschrijft de belangrijkste experimentele ontwikkelingen die nodig waren om tot dit resultaat te komen en bevat een diepgaande karakterisering van dit systeem. Hoewel de kern van dit hoofdstuk is gebaseerd op een peer-reviewed publicatie, bevat het ook aanvullende informatie die nuttig zou kunnen zijn voor diegenen die het hier gepresenteerde werk proberen te reproduceren of uit te breiden. Dit hoofdstuk beslaat ongeveer een jaar werk, van experimentele ontwikkeling tot publicatie. Dit onderzoek, getriggerd door de start van het *iqClock*-project, beoogt het *iqClock*-team te helpen bij het bereiken van hun uiteindelijke doel, de productie van een superstralende laser in stabiele toestand, en het is met hen in gedachten geschreven.

Ten slotte beschrijven we in hoofdstuk 4 een nieuw laserkoelingsschema dat is geïnspireerd op een theoretisch voorstel dat is ontworpen om (anti)waterstof te koelen met een laser. Deze techniek werd onderzocht als een instrument om de atomen in ons systeem efficiënter te vertragen. Maar het zal ongetwijfeld nuttig blijken te zijn in andere situaties en het is een waardevol aanvullend instrument voor de atoomfysicagemeenschap.

A mis padres

Contents

Chapter 1

Introduction

1.1 Overview

During the past decades, sensors using ultracold gases of neutral atoms have risen to be very powerful tools in physics. From the fundamental perspective, they enable searchers for dark matter [1–4] or measurements of gravitational waves [5–8]. In the more applied domain they are becoming increasingly useful tools in geology or geodesy [9–12]. Yet most of these devices suffer from a fundamental limitation, the need to execute each experimental step time sequentially.

For many of these ultracold quantum sensors, the time-sequential or pulsed mode of operation limits their performance, in terms of bandwidth, noise and dynamic range [13–15]. For example, optical clocks and atom interferometers [16, 17] suffer from the Dick effect [13, 18, 19]. The Dick effect results from the pulsed interrogation, and introduces aliasing of high-frequency noise down to frequencies lower than the sensor's interrogation frequency. Other novel types of sensors, such as active clocks based on the principle of superradiant lasing might dramatically improve their performance by operating continuously. In the future these continuously-operating clocks might achieve superior performance to their time-sequentially operating counterparts, while also simplifying the technical requirements [20, 21]. Overcoming the limits imposed by pulsed operation and enabling new types of continuously-operating quantum sensors requires the production of ultracold atomic gases in steady state. However, despite these very promising perspectives, comparatively little effort has been made in this direction.

In this thesis we aim to expand the set of tools available to the atomic physicists by providing new ways to prepare ultracold gases continuously. Here we reach unprecedented phase-space densities in steady-state up to a continuously existing Bose-Einstein condensate (BEC), we provide new sources for continuously operating superradiant lasers and develop new tools to manipulate steady-state ultracold gases. We hope that the tools presented here can be incorporated in state-of-the-art ultracold atom sensors to improve their performance.
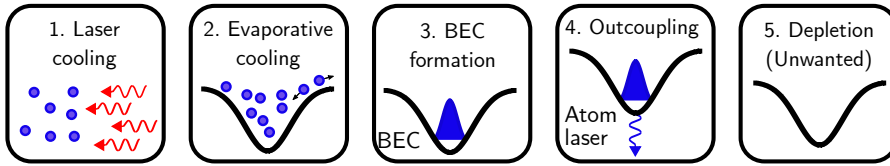
FIGURE 1.1: Typical experimental steps used in references [23–25] to produce atom lasers. First a laser-cooling stage is used to load atoms into a conservative trap (1). Then evaporation is performed inside the trap to produce a BEC (2 and 3). The BEC is outcoupled and an atom laser is formed (4). Finally, due to losses, the BEC is depleted and laser emission stops (5).

1.2   State of the art

Historically the development of ultracold gases in steady state has been closely tied to the pursuit of continuous-wave atom lasers [22]. As the name suggests, atom lasers are the atomic equivalent of the usual optical laser. An optical laser is a beam of photons described by a coherent, propagating electromagnetic wave. Similarly, an atom laser is a beam of atoms described by a coherent, propagating matter wave.

The early demonstrations of **pulsed** atom lasers [23–25] define a baseline on how they can be produced. The experimental steps used in these demonstrations are sketched in figure 1.1. First atoms are laser-cooled and loaded into a conservative trap. After an evaporative cooling step, atoms macroscopically occupy the ground state of the trap forming a BEC. Finally, the atoms are continuously, coherently, and irreversibly outcoupled from the trap to form a coherent beam of propagating atoms, i.e. an atom laser. For these demonstrations, the BEC was depleted over time, stopping the laser emission.

At the turn of the century, many groups took on the challenge to produce a steady-state atom laser, where emission could be sustained indefinitely, reaching the continuous-wave regime already achieved by optical lasers. Unfortunately, the scheme demonstrated in references [23–25] and described in figure 1.1 is not easily extendable to steady-state operation. The key problem is the incompatibility of laser cooling with BECs [26]. Indeed each photon-scattering event kicks at least one atom out of the BEC mode. Typically, in the presence of laser-cooling light, the lifetime of a BEC is shorter than a few ms.[1] What is required is a high-density low-temperature source of atoms that can continuously replenish the BEC.

So what properties must this source have? The key figure of merit is the phase-space density (PSD). The PSD relates the average particle distance in a gas with the size of its

---

[1]Some experiments have been able to reach compatibility by employing creative laser-cooling schemes [27–29]. Yet these techniques alone are unsuitable for steady-state operation due to their low scattering rate.
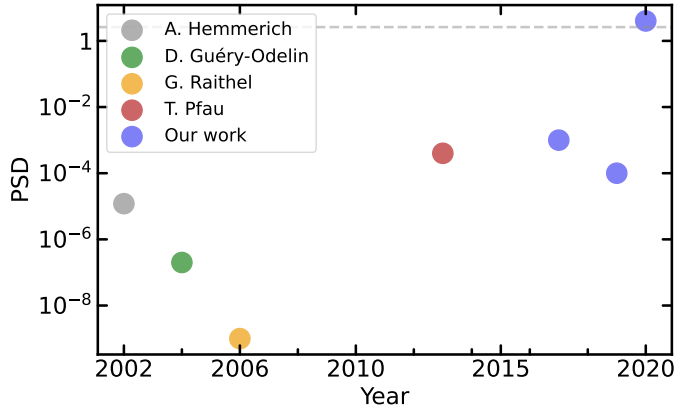
FIGURE 1.2: Towards a steady-state atom laser: The plot shows a selection of the achieved peak phase-space-density of different steady-state experiments. The grey dashed line shows the condition PSD = 2.6. For PSD > 2.6 a BEC is formed. The green, yellow, red, and blue data points show the results from the groups of A. Hemmerich [30] , D. Guéry-Odelin [31] , G. Raithel [32], T. Pfau [33, 34] and our group [35–37] respectively. This is an incomplete list mostly focused on experiments that aimed at producing a steady-state atom laser or that reported the highest PSD at the time.

matter-wave. For a trapped gas, it provides the average occupation of the lowest quantum state. Mathematically this condition is expressed as PSD $= n \cdot \lambda_{\mathrm{dB}}^3$, where λ_{dB} is the thermal de Broglie wavelength and n is the density of the gas. When the PSD is larger than 2.6 the waves of the individual particles start to overlap, and the motional state of the particles is described by one macroscopic matter wave. Laser-cooled clouds typically reach a PSD of only 10^{-6}. The stark difference to the PSD of 2.6 required for BEC illustrates the key challenge of producing a BEC or an atom laser in steady-state: atoms need to be continuously cooled in several stages, dramatically increasing their PSD by several orders of magnitude.

Despite this daunting task, many groups have endeavored to produce atomic sources suitable for a steady-state atom laser. An incomplete selection of different achieved steady-state PSDs is shown in figure 1.2. The group of D. Guéry-Odelin demonstrated a steady-state beam of ^{87}Rb in a magnetic guide. By inducing evaporation they achieved a peak steady-state PSD of 1×10^{-7} [31]. By loading rubidium atoms in a high-gradient magnetic guide the authors of reference [32] achieved a PSD of $\sim 1 \times 10^{-9}$. In these two experiments, a bent in the guide protects the atoms from laser-cooling light, therefore they are compatible with steady-state quantum degenerate gases.

The group of T. Pfau achieved a PSD of $\sim 4 \times 10^{-4}$ by continuously loading a beam

of chromium atoms into a conservative trap. This trap was formed by a combination of magnetic field and optical dipole traps. Here atoms underwent a Sisyphus-like process, that allowed them to achieve the low temperature of 50 μK and high PSD [33, 34].

Different steady-state high-PSD magneto-optical traps (MOTs) have also been reported. Bichromatic MOTs of calcium have achieved a steady-state PSD of 1.2×10^{-5} [30]. Exploiting the properties of narrow intercombination lines, different groups have also achieved very high PSDs [38, 39]. The highest PSD in a MOT was reported by our group in 2017 [35]. Here a combination of spatially-separated laser-cooling stages was used to achieve a PSD of 1×10^{-3}.

When I began this thesis the largest reported PSD in steady-state was the one achieved by our group. During the past years, we worked to bridge the remaining three orders of magnitude needed to achieve a steady-state BEC. Our efforts paid off and in December 2019 we managed to reach this goal [37]. We are closer than ever to achieve the ultimate goal of our experiment, a steady-state atom laser, with only one step remaining: The outcoupling of a beam of atoms from the BEC. Right now we are working on implementing these steps, see chapter 5, and my hope is that in the following years we will be able to produce the long sought continuous-wave atom laser.

1.3   Potential applications of this research

In this section, we aim to describe the potential applications that various steady-state sources of ultracold atoms might have. We focus on the field of precision sensing, in particular on cold-atom interferometry and optical atomic clocks. Other applications such as atomtronics [40–43] are not covered in this section.[2] In the opinion of the author, seeing how far state-of-the-art techniques can be pushed to achieve samples with even higher PSD in steady-state is another interesting question worth exploring. Moreover, in the process of pursuing this goal, we have developed novel laser-cooling techniques (see chapter 4) that might be useful for other applications in the future.

1.3.1   Atom interferometers

A fundamental principle of quantum mechanics is that particles propagate like waves. Similar to electromagnetic waves, matter waves can also interfere. This principle is exploited in atom interferometers [16, 45]. In these devices atoms coherently propagate along two

---

[2]For the reader interested in a more complete description, a very wide (perhaps overly optimistic) list of the potential applications that a high PSD steady-state source of atoms might have can be found in reference [44].

different paths.[3] After recombination, the relative phase acquired along each path becomes apparent in the output of the different ports of the interferometer. Precise measurement of this phase has a plethora of applications, from precise measurements of acceleration [51, 52] and rotation [53] with its implications in geology and geodesy [54, 55], to gravitational wave detection [5, 6, 56], searches for dark matter [57] or tests of the equivalence principle [58, 59]. Here we briefly outline how the work described in this thesis might help to realize some of these applications.

Atom interferometers have reached an outstanding stability, and are becoming increasingly competitive devices in the field of precision measurement. In the measurement of rotation for example they have reached an overall stability of $0.3\,\mathrm{nrad}\cdot\mathrm{s}^{-1}$ over $11\,\mathrm{h}$ of averaging [53]. While such performance is similar to commercial fiber-optic gyroscopes [60, 61], it represents an improvement of an order of magnitude in only two years from previous experiments [62]. Yet to fully realize many of the above applications further improvements in their performance are required [63].

Current state-of-the-art atom interferometers operate in a time-sequential mode, with different stages for sample preparation, interference, and population measurement. Unfortunately, this mode of operation limits their performance in terms of bandwidth and sampling rate and introduces noise through the Dick effect [18, 64]. Creative solutions, such as interleaving different measurements [53, 62] or hybridization with classical sensors [65] can partially solve these problems. A more direct approach to fully overcome them would be to operate the device fully continuously, using a steady-state source of atoms. Some sources demonstrated by our group already achieve high flux and low temperature [35–37] opening this possibility. In the future, these sources might be incorporated in a new class of atom interferometers that operate fully continuously, improving their performance.

Perhaps the ultimate source for atom interferometry would be a continuous-wave atom laser. The atom laser is the matter equivalent of an optical laser. Yet while most optical interferometers operate using laser sources, typically atom interferometers use thermal sources. It should be noted that operation with thermal sources imposes severe limitations on the performance of atom interferometers. For example, it increases the sensitivity to wave-front aberrations of the lasers used for the beam splitters or the Coriolis effect, both major limitations in state-of-the-art atom interferometers [22, 66–70]. On the other hand, current atom lasers suffer from long dead times and low average fluxes[4], which limits their applicability to atom interferometry. Because of its continuous operation, a continuous-wave atom laser would not suffer from any of these issues. Unfortunately, such an advantageous source, which could drastically improve the performance of matter-wave

---

[3]Here we pay exclusive attention to atom interferometry, yet the principle has also been demonstrated for other particles such as electrons [46], neutrons [47], and complex molecules [48–50].

[4]By average flux we mean the number of useful atoms per experimental loading period.

interferometers, has so far not been demonstrated. However, during this thesis, we have come closer than anyone before. My hope is that, in the following years, our steady-state BEC will be out-coupled, producing the first continuous-wave atom laser (see sections 1.2 and 2.4). The first demonstration will be a proof-of-principle experiment. However, with further improvements in its performance, it could become a competitive source for atom interferometry.

1.3.2   Optical atomic clocks

State-of-the-art atomic clocks [17] using fermionic strontium atoms have achieved a stability better than one part in 10^{18} [71, 72]. With such exceptional performance, they enable potential applications such as dark-matter detection [3, 4, 73] , measurements of variations in fundamental constants [74–76], geology, or geodesy [9–12]. Unfortunately, this exceptional performance comes at the cost of high experimental complexity limiting their range of applications.

State-of-the-art atomic clocks, such as the one demonstrated by Campbell et al. [72], are passive devices. First, a laser locked to a high-finesse cavity is used to periodically interrogate a narrow-linewidth transition, such as the mHz-wide $^1S_0 - {}^3P_0$ transition in ^{87}Sr. This atomic transition serves as a reference for a narrow-linewidth laser. The laser's frequency is then down-converted using a frequency comb and used as a reference to measure time. Unfortunately, the experimental complexity in the development of the high-finesse cavities [77–80] limits the potential applications of these devices. First, they are not easily transportable, so for those applications that require portability, such as geodesy, this is a strong issue. Perhaps more importantly, the development of these high-performance resonators is limited to a few groups in the world, which unavoidably slows down development and prevents their inclusion into wider areas of society.

A new class of optical atomic clocks hold the promise of achieving comparable or even superior performance while simplifying the experimental requirements. These are active optical clocks based on superradiant lasing [20, 21]. Active optical clocks are lasers[5] that use a cloud of ultracold atoms within the mode of a cavity as a gain medium. After being pumped to an excited state these atoms can emit into the cavity mode with a rate enhanced thanks to superradiance [81]. If the superradiant laser operates in the bad-cavity regime, the sensitivity of the outcoupled light to cavity-length changes can be greatly reduced.

---

[5]Saying that active optical clocks are lasers is an abuse of language that helps to illustrate the qualitative difference between passive and active optical clocks. The main difference is that in passive optical clocks the frequency of a laser is stabilized to an atomic transition and in an active optical clock the laser light is directly emitted by the atoms.

In the future, by reducing the requirements on high-finesse cavities, active clocks might outperform conventional ones in terms of portability and robustness.

Pulsed superradiant lasing using the mHz-wide $^1S_0 - ^3P_0$ transition of ^{87}Sr, has already been demonstrated [81, 82]. A natural next step is to incorporate steady-state sources into superradiant lasers [83, 84]. The goal is to sustain continuous superradiant emission by replenishing the atoms that have emitted light with new excited-state atoms. Naturally a source of ultracold ^{87}Sr atoms would be useful to achieve this replenishment. In principle, the bosonic isotopes of strontium could be used. However, the linewidth of their clock transition is naturally much weaker than for the fermionic isotope, which adds technical complexities to the already challenging goal suggested here. Indeed pulsed superradiant lasing using the $^1S_0 - ^3P_0$ transition has **only** been demonstrated in ^{87}Sr. Therefore, during this thesis we have developed a steady-state magneto-optical trap of ^{87}Sr atoms, see chapter 3. We hope that in the future, this MOT might be used to continuously feed atoms into the cavity of a superradiant laser.

Is our MOT appropriate for this goal? To reach it, MOT atoms must be transported into the cavity mode, which can be done using a moving optical lattice [85]. Moreover, the cavity region has to be protected against laser-cooling light. After being pumped to the clock state atoms can emit into the cavity mode. Finally the atomic population inside the cavity mode must be renewed by new excited-state atoms entering the cavity mode. We estimate that to achieve superradiance at least $\sim 10^6$ atoms/s at a temperature of $\sim 10\,\mu$K must be brought into the cavity mode. For ^{88}Sr, we are able to transport atoms ~ 4 cm away from the MOT region using a dipole guide with an efficiency of 25 % (see subsection 2.1.2). Taking into account these losses, the total required flux of the MOT must be superior to 4×10^6 atoms/s.

For the steady-state MOT described in chapter 3, we load $1.31(2) \times 10^7$ atoms/s at an average temperature of $12.0(1)\,\mu$K, so our MOT satisfies these requirements with a very reasonable margin. Even in the case of additional unaccounted losses, a potential steady-state superradiant laser experiment should still be possible. Moreover, the MOT flux might straightforwardly be increased by raising the temperature of the strontium oven. In the experiment described in chapter 3, the atomic oven operated at a temperature of $\sim 560\,°$C. We estimate that by increasing the temperature of the strontium oven to $650\,°$C the output flux will increase by more than an order of magnitude while maintaining a reasonable time till the strontium supply of the oven is exhausted. A higher flux might even be achieved by employing more efficient laser-cooling techniques, for example by employing the techniques used in references [86, 87]. Based on these requirements we conclude that our MOT might be used in the future as a source of atoms for a steady-state superradiant laser operating on the mHz-wide transition of ^{87}Sr.

1.4   Thesis outline

The experiment I have been working on these past four years is nicknamed the Strontium Perpetual Atom Laser experiment or SrPAL for short. Indeed, since its inception, the main scientific goal of this experiment has been the production of a steady-state atom laser. The experiment started in the year 2014, and almost eight years and several theses later [44, 86, 88, 89] we have not achieved this goal. Yet we have come closer than anyone before, and during this thesis we have reached a critical milestone, the production of a steady-state BEC.

This thesis covers the four years that the author has been working on the experiment. While our experiment focuses on the path to a steady-state atom laser, we have obtained additional results that might be useful for other purposes in the future. These results are also presented here.

This thesis is intended as a guide that the reader can follow to reproduce these results and to aid researchers working on the SrPAL experiment in the future. It focuses on providing additional information that can potentially be useful and clarifying those aspects that have not been well described elsewhere. The beginning of each chapter is intended as a "map" to help the reader go from a very general description of the research to a very specific technical solution. Each "map" follows the same structure, it starts with a general overview of the work being presented in the chapter and continues with a brief description of each section, briefly outlying its importance for the overall research. [6]

This thesis is structured as follows:

- In chapter 2 we describe how we created a BEC of strontium in steady state. We produce this BEC by laser-cooling atoms in consecutive spatially-separated laser-cooling stages until the gas reaches quantum degeneracy. The production of this BEC represents the accomplishment of a long-standing goal in atomic physics and a critical breakthrough of our experiment.

- In chapter 3 we describe a steady-state magneto-optical trap of fermionic strontium atoms operating on a narrow-line transition. This work was triggered by the formation of the *iqClock* consortium [83] and it aims to serve as a source of ultracold ^{87}Sr atoms for a superradiant laser. Reference [90] constitutes the core of this chapter. We have also included two addenda to this publication that might be useful for those who are trying to reproduce or expand on the results presented here.

- In chapter 4 we describe a novel laser-cooling scheme inspired by the work of Wu et al. [91] to laser cool anti-hydrogen. Our method relies on a spatial modulation of

---

[6]With the exception of chapter 4.

the energy of an excited state using an optical lattice and a narrow-line transition to selectively excite atoms at the bottom of this lattice. After excitation, atoms climb the lattice potential, thereby losing kinetic energy. Following spontaneous emission, atoms return to the ground state, completing one cooling cycle. Our method can, in principle, remove all the energy of the atoms with a single laser-cooling photon. In the future it might be instrumental to laser cool exotic species, such as anti-hydrogen and molecules [92].

- In chapter 5 we discuss the perspectives of producing a steady-state atom laser by outcoupling a beam of atoms from the steady-state BEC. Here we discuss potential outcoupling schemes and introduce the work currently being done in our lab to achieve this goal.

Chapter 2

Continuous-wave Bose-Einstein condensate

During this thesis, our main scientific goal was to achieve a continuous-wave (CW) Bose-Einstein condensate (BEC), a BEC that exists in steady-state for as long as desired. In this chapter, we describe the details required to produce and characterize such a BEC. The research presented here is the culmination of many years of work and spans across multiple publications [35, 36, 93] and theses [44, 86, 88, 89].

We begin our discussion in section 2.1 by describing the main experimental components used to produce a CW BEC. To briefly summarize, we realize such a BEC by continuously cooling a gas of strontium atoms in different spatially-separated laser cooling stages. Initially, atoms emanating from a high-temperature oven at $\sim 500\,°C$ are cooled down to the µK regime. These µK-cold atoms arrive in a cross-beam optical dipole trap formed by a "reservoir" trap and a "dimple" beam (see figure 2.4). Here, as atoms continuously load the larger reservoir trap their entropy is removed by laser cooling light. At the center of the reservoir trap, the tightly focused dimple beam increases the density of the gas, while a "transparency" beam renders the dimple transparent to laser-cooling light. The entropy of the dimple atoms is removed by thermal exchange with atoms in the reservoir. In the dimple trap, a CW BEC can be formed.

These three laser beams, the dimple, the reservoir, and the transparency, are key elements that allow us to form a CW BEC, so in the following sections we describe them in more detail. In section 2.2 we describe the transparency mechanism and laser system, and in section 2.3 we show how efficient cooling and loading of the reservoir is attained.

The goal of the above introduced sections is to describe in detail the key elements required to produce a CW BEC. Therefore they do not include some key characterizations of the system. They do not include answers to important questions such as: How is the atomic cloud characterized? How is the BEC atom number measured? What is the BEC

atom number evolution? What are the BEC atom number fluctuations? What is the BEC formation timescale? What is the timescale to reach steady-state? These questions are answered in reference [37], which is reproduced in section 2.4

2.1 Experiment overview

In this section we briefly describe the key components of the experimental apparatus required to produce steady-state ultracold and quantum degenerate gases. This section is structured as follows: In subsection 2.1.1 we describe a steady-state MOT on the 7.5 kHz-wide $^1S_0 - {}^3P_1$ transition. This MOT is produced by a series of spatially-separated laser cooling stages. Starting from a sample at 550 °C, atoms are cooled down to the µK regime and trapped in this MOT. Here, the phase-space density (PSD) is limited by the high light intensity required to slow and trap the atoms.

To produce samples with higher PSD, we transfer the atoms away from the MOT location to a darker region. In subsection 2.1.2 we describe how the atom transfer is achieved. A combination of a dipole guide and laser cooling beams transfers the atoms away from the MOT location into this dark region. The result is a steady-state strontium beam with high PSD (10^{-4}). This beam could be used as a source for atom interferometry or superradiant lasers [36]. In our case, it represents an ideal source for the production of quantum degenerate gases.

A steady-state quantum degenerate gas can be created by combining two key experimental techniques. Firstly the high-PSD atomic beam described above can be used to continuously load a reservoir trap at sub-µK temperatures. Secondly a 2013 technique recorded in reference [27] can be used in such a reservoir trap to achieve a degenerate cloud of atoms in the presence of the laser cooling light [27]. In subsection 2.1.3 we show how to continuously load the atoms from the beam into the reservoir trap. Finally, in subsection 2.1.4 we show how we implement the *laser cooling to quantum degeneracy* technique in the continuously loaded reservoir trap to produce a CW BEC.

2.1.1 A steady-state magneto-optical trap on a narrow-line transition

The starting point of our experiment is a steady-state narrow-line magneto-optical trap operating on the $^1S_0 - {}^3P_1$ transition. Here, we briefly describe how this MOT is produced.

A sketch of the experimental architecture used to produce the MOT is shown in figure 2.1. Starting from a high-temperature oven at ~ 550 °C we cool the atoms in different spatially-separated laser cooling stages finally reaching the µK regime. Atoms emanating from an oven are first radially cooled and then slowed down by laser beams addressing the
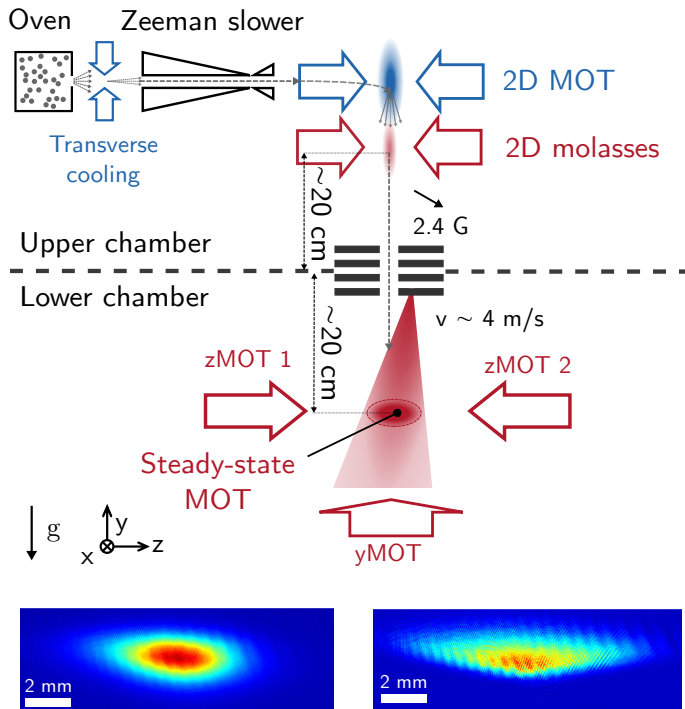
FIGURE 2.1: (Top) Sketch of the experimental architecture used to produce steady-state narrow-line MOTs of strontium. The dashed arrows highlight the path that atoms follow. (Bottom) Example of absorption images of MOTs of ^{87}Sr (left) and of ^{88}Sr (right).

$^1S_0 - {}^1P_1$ transition. Slowed atoms are then funneled by a 2D MOT using the same transition and transferred to a lower chamber through an 8 mm baffle. Transferred atoms then accumulate in a steady-state narrow-line 3D MOT addressing the $^1S_0 - {}^3P_1$ transition.

The final goal of the presented architecture is to achieve steady-state quantum degenerate gases. To achieve this goal we need to protect the atoms against resonant light [94]. To protect quantum degenerate atoms from the highly destructive effects of the $^1S_0 - {}^1P_1$ transition, our experiment relies on the two-chamber design previously introduced, with an upper chamber and a lower chamber. Atoms in the upper chamber, where the 2D MOT is produced, can be addressed by any transition at our disposal. In the lower chamber, where atoms accumulate in a narrow-line 3D MOT, we only use far-off-resonant laser light or light addressing the narrow-line $^1S_0 - {}^3P_1$ transition.

The destructive effects of the $^1S_0 - {}^3P_1$ transition can be overcome by inducing a light-shift on the $^3P_1$ state, locally shifting the $^1S_0 - {}^3P_1$ transition out of resonance. In such a way a BEC can be produced in the presence of $^1S_0 - {}^3P_1$ laser-cooling light [27, 37]. Note that, due to its broad linewidth, using the same technique on the 30 MHz-wide $^1S_0 - {}^1P_1$ transition has not been shown to be possible.

Due to the high radial velocity of atoms exiting the 2D MOT, collimation right after it is imperative. This collimation could be achieved by accelerating the atoms in the propagation direction to high velocities. However, due to the low scattering rate of the $^1S_0 - {}^3P_1$ transition, we would not be able to capture these high-velocity atoms in the lower chamber. Therefore, in our experiment, we employ a 2D molasses addressing the $^1S_0 - {}^3P_1$ transition to radially cool the atomic beam. This molasses is a key component of the experiment, as it increases the atomic flux captured in the lower chamber by more than two orders of magnitude.

In Figure 2.1 we show absorption images of the MOT for ^{88}Sr and ^{87}Sr respectively. For ^{88}Sr, the most abundant isotope of strontium, we can routinely produce steady-state MOTs of $\sim 10^9$ atoms, with temperatures of $\sim 10\,\mu$K and loading rates of more than 10^8 atoms/s. As a general rule, for the other isotopes of strontium, the flux and atom numbers are mostly limited by the natural isotopic abundance, while the temperature remains similar.

There are several shortcomings to the architecture just presented. Firstly, the achieved temperature is too high to achieve condensation. Secondly, the MOT is located in direct line of sight from the top chamber so atoms can still be addressed by photons resonant to the $^1S_0 - {}^1P_1$ transition. These photons could come, for example, from unwanted reflections of the laser beams in the upper chamber, or the fluorescence of the 2D MOT atoms. Overcoming these limitations is key to achieve steady-state quantum degenerate gases.

The temperature is limited by the high velocity of the atoms entering the lower chamber,
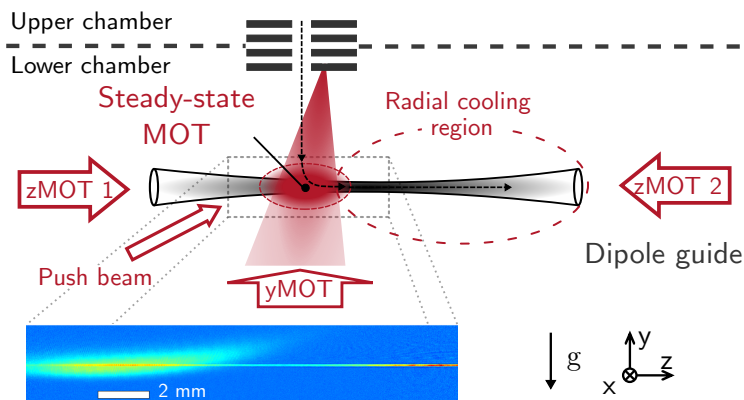
FIGURE 2.2: Sketch of the experimental architecture used to produce a steady-state ultracold beam of strontium. The dashed arrows sketch the direction that the atoms follow as they load the dipole guide. The dashed ellipse shows the approximate region where the atoms are addressed by the radial cooling beams. The inset shows a typical in-situ absorption image of the MOT loading the beam in steady state.

which limits the operation parameters of the MOT. Indeed due to this high velocity, atoms need to be slowed before they reach the MOT region. The vertical beam serves a dual purpose, it achieves this slowing and provides trapping for the MOT. Efficient slowing is achieved at the cost of a slightly higher temperature, by modulating the frequency of the vertical beam with a span of 2.55 MHz, and keeping the intensity of the laser beam high compared to the $^1S_0 - {}^3P_1$ transition's saturation intensity.

Despite these limitations, we find this narrow-line steady-state MOT to be an excellent source for the remaining cooling stages of the experiment, and it is a key component of the experimental architecture.

2.1.2 A guided strontium beam with high phase-space density

To achieve higher PSD the atoms must be transported away from the MOT, to a darker region where the red light is not as intense and where there is no direct line of sight to the 2D MOT addressing the $^1S_0 - {}^1P_1$ transition and the blue light fluorescing from it. From all of the approaches that were taken over the years, outcoupling the atoms using a dipole guide to produce a high PSD beam proved to be the most effective. Here we briefly describe how this high-PSD beam is produced. For an in-depth analysis of the atomic beam properties and a detailed description of how to produce it, see reference [36].[1]

---

[1]Since reference [36] was published, we have upgraded our 2D MOT system, increasing the atomic flux by more than an order of magnitude (see subsection 2.3.3).

A sketch of how this beam is produced can be found in figure 2.2. Starting from the previously described MOT, atoms are continuously loaded into a dipole guide. This guide is produced by a retro-reflected 12 W 1070 nm laser beam. This beam is focused at the MOT location, where the waist is 92 µm and the trap depth is 35 µK. The beam is retro-reflected, to flatten the potential landscape along the beam's axis, and 37 mm away from the MOT center the trap depth is 25 µK and the radial trap frequency is $2\pi \times 180$ Hz.

To control the velocity of the outcoupled atoms, an additional laser beam is used. This beam addresses the $^1S_0 - {}^3P_1$ transition and "pushes" the atoms away from the quadrupole center of the MOT. The power of this beam controls the mean atomic velocity of the outcoupled atoms. For typical powers of 30 nW the mean velocity of atoms traveling through the guide is around $8 - 9 \, \text{cm} \cdot \text{s}^{-1}$.

As shown in figure 2.2, the dipole guide is overlapped and copropagating with the MOT beam pair propagating along the z-axis. The restoring force of the MOT is reduced thanks to the detuning induced by the dipole trap's differential light-shift. However, to efficiently outcouple atoms into the guide, further reduction of this restoring force is required. To do so, we image a 20 cm long 600 µm wide cylinder into the two MOT beams that co-propagate with the dipole guide [36, 95]. This cylinder attenuates the MOT light in the region where the MOT beams overlap with the guide, and allows outcoupling from the MOT atoms into the dipole guide.

As atoms travel through the guide, a set of three beams (two on the horizontal plane and one in the vertical direction) radially cools the atoms. The approximate region of interaction of these three radial-cooling beams with the atoms is sketched as a red dashed ellipse in figure 2.2. To avoid unnecessary heating the power must be set as low as possible. These three beams are slightly blue detuned from the unperturbed $^1S_0 - {}^3P_1$ π transition, to account for the differential light shift produced by the guide. Because we address the nonmagnetic π transition, radial cooling is not affected by the magnetic gradient of the MOT.

The $1/e^2$ diameters of these laser-cooling beams are 36 mm and 48 mm for the vertical and horizontal beams respectively. Typically these beams operate with $1 - 10$ µW of laser power and are blue detuned by about $20 - 80$ kHz. This choice of detuning is smaller than the differential light-shift created by the dipole guide, so at the trap center atoms are red detuned from the cooling transition. 37 mm away from the quadrupole center, the right experimental parameters can result in high-density sub-µK strontium beams.

An absorption picture of the MOT atoms loading into the guide is shown in figure 2.2. At the location of a reservoir trap (see the following section), ~ 4 cm away from the MOT center, we measure a flux of atoms through the guide of $9(1) \times 10^6$ atoms/s with a radial temperature of ~ 1 µK and an average axial velocity of $9(1) \, \text{cm} \cdot \text{s}^{-1}$. The PSD
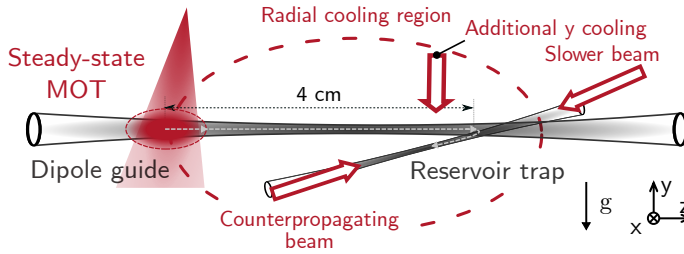
FIGURE 2.3: Sketch of the experimental scheme used to load the reservoir. The dashed arrows sketch the trajectory of the atoms that load the reservoir. The dashed ellipse shows the region of interaction between the atoms and the radial cooling beams. For clarity, the reservoir is not shown to scale.

of the guided atoms peaks around $\sim 10^{-4}$.[2] This high phase-space-density beam could be used for applications ranging from superradiant lasers to atom interferometry. In the following sections, we will describe how this source was used to produce a CW Bose-Einstein condensate.

2.1.3 Reservoir loading

To achieve a CW BEC a PSD increase of more than three orders of magnitude is required. To do so we load the atoms from the beam into a reservoir trap. In this reservoir, we implement the *laser cooling to quantum degeneracy* technique demonstrated by Stellmer et al. [27], to further increase the PSD and achieve condensation. Here we describe how the guided atoms are loaded into the reservoir trap.

A sketch of the experimental scheme used to load the reservoir trap is shown in figure 2.3. Atoms are transported $\sim 4\,$cm away from the MOT to a darker region where MOT light is not as intense. Atoms propagating through the dipole guide are first slowed down by a "slower beam" addressing the $^1S_0 - {}^3P_1\ \sigma^-$ transition.[3] After stopping the atoms travelling in the positive $\vec{z}$-direction, the beam accelerates them in the opposite, negative $\vec{z}$-direction, and they fall into the reservoir. Since the reservoir is a conservative trap, atoms must be slowed and cooled to create irreversible loading. A set of four beams achieves this irreversible loading. First, a counter-propagating beam addressing the $^1S_0 - {}^3P_1\ \sigma^-$ transition slows the atoms propagating in the negative $\vec{z}$-direction. Then a set of four beams radially cools the atoms inside the reservoir.

---

[2]Here we quote the PSD from reference [36]. Fortunately, due to upgrades in the 2D MOT system, the PSD now achievable in the experiment is around an order of magnitude higher (see subsection 2.3.3).

[3]In previous theses and publications of our group, this beam is labeled "Zeeman slower beam", because of its operating principle. However here we name it "slower beam" to avoid confusion with the Zeeman slower beam shown in figure 2.1

The reservoir trap forms a sheet, i.e. the confinement is much stronger in the vertical direction than in the horizontal plane. Indeed the vertical beam waist is 17 μm and the horizontal beam waist is 110 μm, the trapping frequencies are $(\omega_x, \omega_y, \omega_z)/2\pi = (95\,\text{Hz}, 740\,\text{Hz}, 15\,\text{Hz})$ and the reservoir trap depth is 11.5 μK.

The slower beam itself exploits the magnetic field gradient of the MOT quadrupole field to compensate for the Doppler shift of the incoming atoms and to select the region where they are slowed. To avoid unnecessary heating the power of this beam is set as low as possible. In steady-state we find that a light intensity of $\sim 6\,\mu\text{W}\cdot\text{cm}^{-2}$ is enough to efficiently load the reservoir.

The counter-propagating beam addresses the $^1S_0 - {}^3P_1$ σ^- transition and also exploits the magnetic field gradient of the MOT to spatially select the region where it addresses the atoms. Typically this beam operates with an intensity of $\sim 60\,\mu\text{W}\cdot\text{cm}^{-2}$. Its modulation and detuning are similar to the ones used for the slower beam.

Finally, three of the radial reservoir cooling beams are the same beams used for radial cooling of the high-PSD atomic beam. Therefore they couple the cooling conditions of the reservoir and the guide. As a consequence, the parameters of the guide, reservoir, and radial cooling beams cannot be tuned independently. An additional beam counterpropagating to the vertical radial cooling beam mostly overlapped with the reservoir is used to improve the laser cooling condition of the reservoir trap.

The result of the presented architecture is a continuously loaded reservoir that can be used to produce a CW BEC. In this reservoir, we can load more than $7(2) \times 10^5$ atoms at temperatures colder than $\sim 1\,\mu\text{K}$.

2.1.4 A continuous-wave Bose-Einstein condensate

For strontium, the narrow-line character of the $^1S_0 - {}^3P_1$ transition can be exploited to produce quantum degenerate gases where all the entropy is removed by laser-cooling light. This technique was first reported by Stellmer et al. [27] and can be used in our reservoir to produce a CW BEC.

To implement this technique, two additional key components are required: a "dimple" beam and a "transparency" beam (see figure 2.4). Firstly the tightly focused dimple beam crosses the reservoir trap at its center. The dimple beam boosts the density of the gas while the temperature remains similar thanks to elastic collisions with atoms in the reservoir. The resulting effect is a PSD enhancement at the center of the reservoir trap [96]. Secondly, a transparency beam shifts the laser cooling transition of atoms inside the dimple out of resonance. Therefore, the atoms inside the dimple region are rendered transparent to the laser-cooling light and protected from it. The resulting density increase combined with the
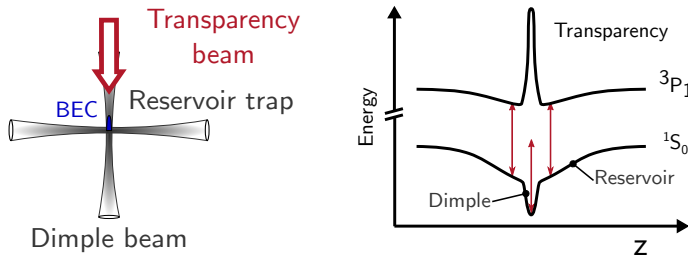
FIGURE 2.4: Laser cooling to BEC. The reservoir atoms are cooled down to $\sim 1\,\mu K$ by light addressing the $^1S_0 - {}^3P_1$ transition. The dimple beam locally increases the PSD. At the same location, atoms are rendered transparent to laser-cooling light thanks to the transparency beam. (Left) Sketch of the experimental scheme used in reference [27]. (right) Sketch of the resulting spatially-dependent energy levels.

transparency protection scheme can be used to produce a BEC by removing entropy from the gas by laser cooling light.

In our experiment, we implemented a dimple and a transparency beam in the continuously loaded reservoir to produce a BEC in steady state. Figure 2.4 (C) shows the key experimental components required to produce a CW BEC. First, the reservoir trap is loaded in steady state as described in subsection 2.1.3. Then reservoir atoms continuously load a dimple beam. This dimple beam is a vertically-propagating 1070 nm beam that crosses the reservoir trap at its center. The waist of the dimple beam is 27 μm measured by BEC center of mass oscillations and its power is 130 mW. As atoms load the dimple trap, their entropy is removed by heat exchange with the reservoir atoms. Therefore, in steady-state, the temperature of the reservoir and dimple atoms is similar. Finally, a transparency beam protects the atoms from the destructive effects of laser-cooling light and allows us to produce a CW BEC. This transparency beam is counter-propagating to the dimple beam and its waist is 22 μm. In this system BEC losses are continuously compensated by atoms arriving first into the reservoir, then into the dimple, and finally condensing by Bose-stimulated scattering. The inset of figure 2.4 (C) shows in-situ absorption pictures of the reservoir and dimple atoms.

In figure 2.6 we show time-of-flight images of this system taken at different loading times. To obtain this data, we switch on all of the laser beams at $t = 0$ and then wait for different times. Initially, as atoms load the reservoir and dimple the density of the gas increases ($t < 2.8\,s$). Then, as the density continues to increase, between $2.8 - 3.1s$ an elliptical feature appears. Such an elliptical profile shows that a CW BEC has formed. Finally, after $\sim 5\,s$ the system reaches steady state and no meaningful change can be observed and the system has
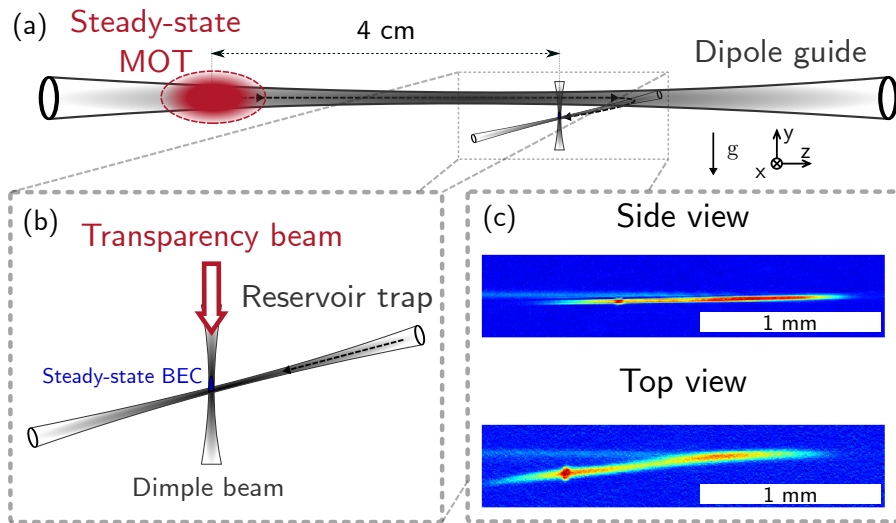
FIGURE 2.5: (a) Sketch of the experimental architecture used to create BECs in steady state. MOT atoms are loaded into the dipole guide and transported to the reservoir trap, located $\sim 4\,\mathrm{cm}$ away from the MOT in a darker region. (b) Zoom into the reservoir region. Two beams, the transparency, and the dimple beams cross the reservoir trap at its center. The result is an ultracold BEC in steady state. (c) In situ absorption pictures of the steady-state system, from above (along the negative $\vec{y}$-direction) and the side (along the negative $\vec{x}$-direction).
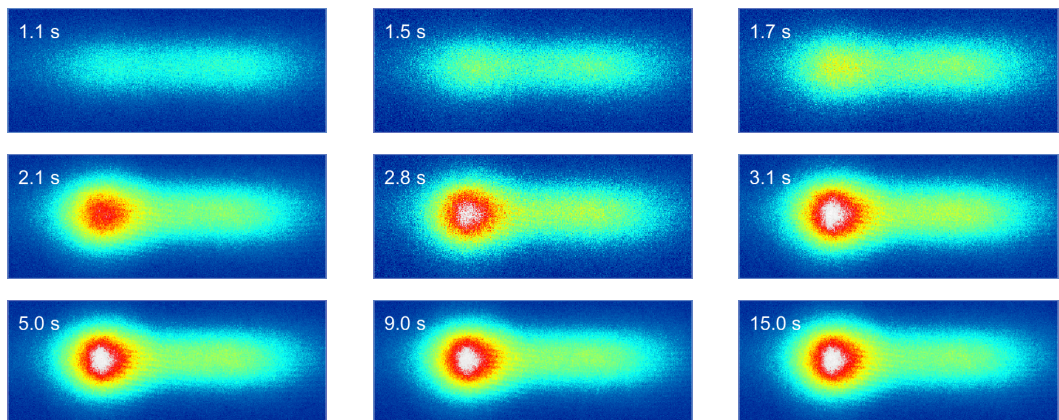
FIGURE 2.6: Time-of-flight images of the steady-state system at different loading times, shown in the top left corner of the images. At $t = 0$ all of the laser beams are turned on. Initially, the reservoir and dimple beam are loaded, and the density in this region increases. Around $t = 3.1\,\mathrm{s}$ an elliptical feature appears and a BEC is formed. Later, at $t > 5\,\mathrm{s}$ no further evolution of the cloud can be detected and the system has reached steady state. The presented data is an average of four different pictures.

reached steady-state. At steady state, we observe $6.9(4) \times 10^5$ atoms in the dimple at a temperature of $1.08\,\mu K$. From the atoms that load the dimple, only $74(23) \times 10^2$ atoms occupy the BEC mode.

The goal of this section has been to give a brief experimental description of the key elements required to produce a CW BEC. Here we have deliberately left some open questions: Have we truly formed a CW BEC, or can such an elliptical feature be understood with an alternative explanation? How is the BEC atom number determined? What are the BEC atom number fluctuations? Is it possible that the BEC disappears due to experimental fluctuations? Is the system in thermal equilibrium, or is it far away from equilibrium? These questions are covered in reference [37] and in section 2.4

2.2   BEC Protection

A BEC addressed by laser-cooling light will have a lifetime of, at most, several milliseconds. Indeed, each single-photon scattering event will remove at least one atom from the condensate, eventually destroying it. To produce a BEC in steady-state one needs to solve this incompatibility.

In strontium, one can address this problem by using a "transparency" beam to light-shift the laser-cooling transition out of resonance and allow a BEC to "survive" in the presence of laser light (see reference [97] and section 2.1.4). This transparency beam light-shifts the $^3P_1$ state out of resonance and renders the BEC transparent to laser cooling photons. It forms an integral part of the steady-state architecture and is required to produce steady-state quantum gases in presence of laser cooling light. In this section, we describe important aspects relevant to the functioning of this transparency beam. The reader should be aware that the protection system reported in references [44, 89] has been strongly improved (see section 2.8) and should consider these references, for this particular topic, outdated.

We start our discussion in subsection 2.2.1 with a brief theoretical analysis of the protection mechanism. We show that the light-shift achieved by the transparency beam using the configuration of reference [27] always saturates at high laser powers for one of the $^3P_1$ Zeeman sub-levels. This saturation arises from a two-photon coupling between states in the $^3P_1$ manifold and can be overcome by addressing the atoms with two frequency components at different polarizations.

We continue in subsection 2.2.2 by recalling the operational parameters used for the transparency light and describe the laser system used to generate such light.

Finally, in subsection 2.2.3 we benchmark the performance of the system. We measure the lifetime of a pulsed BEC in presence of the laser cooling light usually used for the generation of a CW BEC. We calibrate the magnetic field used in the experiment and
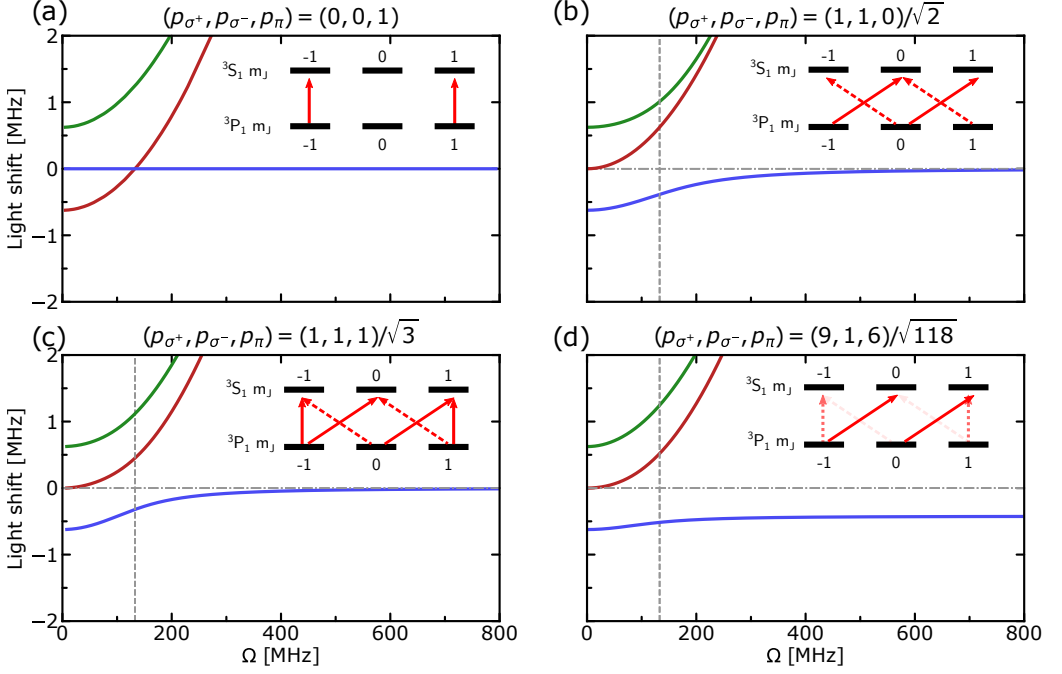
FIGURE 2.7: Calculations of the transparency induced light-shift for several beam polarizations when using single frequency light. (a) For pure π-polarized light. (b) For light addressing the σ^+ and σ^- transitions equally. (c) For light addressing the σ^+, σ^- and π transitions equally. (d) For the polarization vector used in the experiment. The vertical dashed lines show the condition $\Omega = \sqrt{\Delta \delta_z}$. For $\Omega \gg \sqrt{\Delta \delta_z}$, the two-photon coupling between states in the $^3P_1$ manifold becomes stronger than the single-photon coupling to the $^3S_1$ state. This two-photon coupling results in a state that does not shift in energy and the achieved light-shift always saturates at high Rabi frequencies within the $\pm \delta_z$ range.

measure the transparency beam waist by center of mass oscillations of a BEC trapped in the transparency beam. Finally, we compare the achieved light-shift with the theory of subsection 2.2.1 and show that the theory achieves qualitative agreement.

2.2.1   Protection theory

To protect a BEC from resonant light addressing the $^1S_0 - {}^3P_1$ transition each of the Zeeman sub-levels of the $^3P_1$ excited state needs to be shifted out of resonance. Unfortunately, the range of achievable light-shifts using a single frequency component for the transparency beam, as done by Stellmer et al. [27], is limited to a few MHz given by the Zeeman shift (δ_z). Indeed, at high Rabi frequencies, the light-shifts saturate within the $\pm \delta_z$ span, which is insufficient for our purposes. Note that in our experiment the control of the magnetic field is limited by requirements of the MOT, see section 2.1, and only the laser power and

polarization can be tuned freely. Here we show, with a brief theoretical analysis, the origin of this saturation and how it can be overcome.

We begin by analyzing some simple cases by which one could hope to achieve the desired light-shift. Addressing the atoms with pure π polarization, as shown in figure 2.7 (a), straightforwardly fails, as one Zeeman sub-level remains unaddressed.[4] A similar situation occurs when addressing the atoms with pure σ^+ or σ^- polarized light. A natural approach to overcome this limitation is to use a combination of σ^+ and σ^- light to achieve the desired shift, see figure 2.7 (b). However, at high Rabi frequencies, such that $\Omega/\sqrt{|\delta_z\Delta|} \gg 1$, the two-photon coupling between the $|^3P_1, m_J = +1\rangle$ and $|^3P_1, m_J = -1\rangle$ states becomes stronger than the single-photon coupling to the $^3S_1$ excited states. Here, Δ is the laser detuning from the $^3P_1 - {}^3S_1$ transition, and δ_z is the Zeeman shift. In this limit, the state $|D\rangle = |^3P_1, m_J = 1\rangle + |^3P_1, m_J = -1\rangle$ becomes an eigenstate of the Hamiltonian. This state has the same energy as the unperturbed $^3P_1$ $m_J = 0$ state and it can be addressed by laser-cooling light, potentially destroying the condensate. In the more general case, where one addresses the atoms with any possible combination of σ^+, σ^- or π polarizations, at high Rabi frequencies a two-photon coupling always gives rise to a state that does not shift in energy. The energy of this state will always be within the $\pm\delta_z$ range and it can be addressed by our laser-cooling light, see figures (c) and (d).

To achieve arbitrary shifts, the two-photon coupling between states of the $^3P_1$ manifold needs to be suppressed. To do so, we address the atoms with two different frequencies, ω_1, and ω_2 and with orthogonal polarizations. Choosing these frequencies such that $\Delta\omega = |\omega_1 - \omega_2| \gg \Omega_{max}^2/\Delta$, we can suppress the two-photon coupling between each of the states of the $^3P_1$ manifold and obtain much larger transparency shifts. Here Ω_{max} is the maximum Rabi frequency achievable in the experiment. In our experiment $\Delta\omega = 1.4\,\text{GHz}$, $\Omega_{max} = 2.1\,\text{GHz}$ and $\Delta = 30\,\text{GHz}$. Under these conditions, we are able to measure vacuum limited BEC lifetimes in presence of the light used in the CW BEC experiment, see subsection 2.2.3.

In the general case the light-shift of the $^3P_1$ Zeeman sub-levels can be calculated by solving the time-independent Schrödinger equation. Under the rotating-wave and dipole

---

[4]Note the vanishing Clebsch-Gordan coefficient of the $J = 1$ $m_J = 0$ to $J = 1$ $m_J = 0$ transition.

approximations the Hamiltonian describing the level structure shown in figure 2.7 becomes:

$$
H = \frac{\hbar}{2\sqrt{2}}
\begin{bmatrix}
-2\sqrt{2}\delta_z & 0 & 0 & -\Omega p_\pi & -\Omega p_{\sigma+} & 0 \\
0 & 0 & 0 & \Omega p_{\sigma-} & 0 & -\Omega p_{\sigma+} \\
0 & 0 & +2\sqrt{2}\delta_z & 0 & \Omega p_{\sigma-} & \Omega p_\pi \\
-\Omega p_\pi & \Omega p_{\sigma-} & 0 & -2\sqrt{2}\Delta & 0 & 0 \\
-\Omega p_{\sigma+} & 0 & \Omega p_{\sigma-} & 0 & -2\sqrt{2}\Delta & 0 \\
0 & -\Omega p_{\sigma+} & \Omega p_\pi & 0 & 0 & -2\sqrt{2}\Delta
\end{bmatrix}
\tag{2.1}
$$

Where $p_{\sigma+}$, p_π and $p_{\sigma-}$ are the polarization components of the laser light, Δ is the light's detuning from resonance, $\pm\delta_z$ is the Zeeman shift of the $^3P_1$ $m_J = \pm 1$ states and Ω is the Rabi frequency of the laser light. The $1/\sqrt{2}$ factor as well as the sign of the off-diagonal terms result from the Clebsh-Gordan coefficients of the transitions. Here we have approximated the Zeeman shift of the $^3S_1$ states Zeeman sub-levels to be much smaller than the detuning choice of the transparency beam.

Figure 2.7 shows the resulting light-shifts as a function of the Rabi frequency for different combinations of $p_\pi, p_{\sigma+}, p_{\sigma-}$.[5] Due to the coupling within states of the $^3P_1$ manifold, a state always exists whose energy lies in the $\pm\delta_z$ span. This region can be addressed by the laser-cooling light, potentially destroying the condensate.

2.2.2 Transparency laser system

To circumvent the highly destructive effects of the laser-cooling light, we use a single vertically-propagating "transparency" beam addressing the $^3P_1 - {}^3S_1$ transition to locally shift the $^3P_1$ state. This beam is focused at the BEC location with a beam waist of 23 µm and is blue-detuned by ~ 30 GHz from the $^3P_1 - {}^3S_1$ transition. To circumvent the two-photon coupling described in subsection 2.2.1, this beam uses two frequency components with two orthogonal polarizations. The relative frequency difference is 1.4 GHz and their polarization is set circular with opposite handedness. The atoms are addressed by a total power of 10 mW corresponding to 7 mW for the right-hand circular component and 3 mW for the left-hand circular component. At the BEC location we measure a magnetic field of $\{B_x, B_y, B_z\} = \{0.003(6), 0.414(3), 0.762(3)\}$G, see subsection 2.2.3. Given this field orientation, the right-hand circular component of the transparency beam addresses the atoms with a polarization vector of $\{p_{\sigma+}, p_\pi, p_{\sigma-}\} = \{1, 6, 9\}/\sqrt{118}$ and, for left-hand circular light, with $\{p_{\sigma+}, p_\pi, p_{\sigma-}\} = \{9, 6, 1\}/\sqrt{118}$.

A schematic of the laser system used to generate this light is shown in figure 2.8. The 688 nm light is initially generated by a home-made external-cavity diode laser (ECDL).

---

[5]The different choices of $p_\pi, p_{\sigma+}, p_{\sigma-}$ correspond to different laser light polarization.
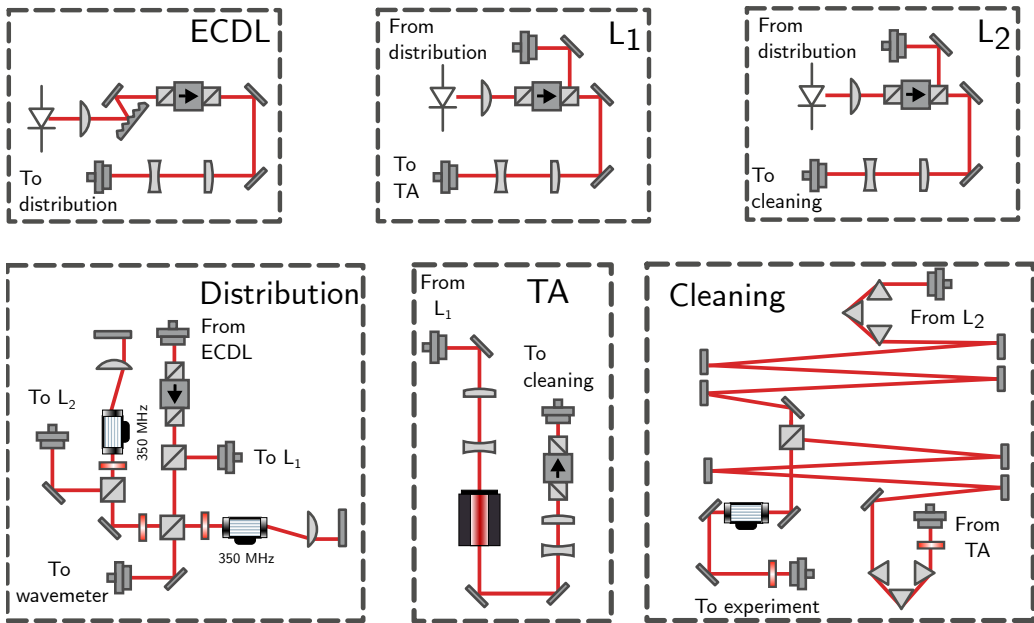
FIGURE 2.8: Simplified scheme of the laser system used to generate the transparency light. An ECDL is used as a frequency reference for two diode lasers, shown as laser$_1$ (L$_1$ and laser$_2$ (L$_2$) respectively. The reference light sent to L_2 is frequency shifted by 1.4 GHz while the light used for L_1 is not shifted (see distribution). To further increase the available power, L_2 is used to inject a TA. Finally, the light from L$_1$ and the TA is sent to a frequency cleaning system before being sent to the atoms. The dashed lines indicate the different breadboards used in the experiment.

The light of this ECDL is set $\sim 30\,\mathrm{GHz}$ blue-detuned from the $^3P_1 - ^3S_1$ transition. Since the short-term frequency drift of this ECDL is much smaller than the laser detuning from resonance, the laser is left free running and the frequency is monitored using a wave-meter (*WS7-30* from High-Finesse).

The ECDL light is used to injection lock two additional diode lasers. The seed of one of these lasers is frequency shifted by $1.4\,\mathrm{GHz}$ using two subsequent acousto-optic modulators (AOMs) in double-pass configuration. To further increase the available power, the light of the unshifted laser is used to inject a tapered amplifier (TA *EYP-TPA-0690-00500-2003-CMT02-0000*). In our configuration, this TA can produce up to $93.6\,\mathrm{mW}$ of laser power after a single mode optical fiber while the frequency-shifted slave laser delivers $38\,\mathrm{mW}$.

These two light sources, the TA and the slave laser, could be straight-forwardly combined with the desired orthogonal polarization using a polarizing beam splitter before sending it to the atoms. Unfortunately, the wavelengths of the $^1S_0 - ^3P_1$ transition and $^3P_1 - ^3S_1$ transition are only $1.5\,\mathrm{nm}$ apart and the spectrum of the TA and the diode lasers features broadband emission, resulting from amplified spontaneous emission (ASE) in the gain medium of the laser, that can address the $^1S_0 - ^3P_1$ transition. This undesired scattering on the $^1S_0 - ^3P_1$ transition reduces the lifetime of the condensate to less than $100\,\mathrm{ms}$.

This problem can be solved by cleaning the light using a dispersive element, such as a prism or a grating, followed by a long path length and an aperture. In our experiment we use two sets of three prisms each as dispersive elements, see figure 2.8, followed by a propagation path of $2.5\,\mathrm{m}$ for the left-hand circular light, and $3.9\,\mathrm{m}$ for the right-hand circular light. The two frequency components are then apertured using an iris and combined before being injected into an optical fiber to be sent to the atoms.

Several design considerations are crucial for the good performance of the filtering system:

- For high transmission efficiency the light incident on the prisms must do so under Brewster angle with the correct polarization. To satisfy this condition for both laser beams we use individual filtering stages, see figure 2.8. Our transmission efficiency after the three prisms can be up to 90%.

- For efficient cleaning, it is crucial to filter the spatial mode of the diode lasers before sending the light to the filtering system. This filtering can be straightforwardly done by injecting the light into a single-mode optical fiber before sending it to the cleaning system.

- The cleaning efficiency of the system was measured by using light at the undesired $689\,\mathrm{nm}$ wavelength using the shorter of the two cleaning paths. In this way, we obtain an upper limit on the ASE suppression efficiency of $\sim 30\,\mathrm{dB}$.

Finally, we combine both laser beams with orthogonal polarizations and send the light to the atoms.

2.2.3   Characterizations

So far, in subsection 2.2.1 we have described the protection theory required to calculate the light-shift of the relevant states, and in subsection 2.2.2 described the transparency beam operation parameters used in the experiment and shown how the required light was generated. We found this system to be optimal based on different experimental characterizations. Here we show those relevant experimental characterizations.

BEC lifetime. The lifetime of the BEC under the presence of transparency light and laser-cooling light is the most important figure-of-merit of the protection scheme. To measure it, we first time-sequentially create a BEC,[6] then we illuminate it with transparency light, and finally we switch the laser cooling beams on. Figure 2.9 (a) shows the resulting BEC decay (red circles). For comparison, we show the vacuum-limited BEC lifetime (blue squares) and the BEC lifetime under the presence of laser-cooling light (green circles). Additionally, as the BEC decays, we also observe a MOT forming about 4 cm away, see the inset of figure 2.9. This data clearly shows the effectiveness of the protection scheme.

Magnetic field calibration As mentioned in subsection 2.2.1, the achieved light-shift depends on the polarization decomposition, p_{σ^+}, p_π and p_{σ^-}, of the light. This decomposition depends on the light polarization and on the magnetic field orientation. Good knowledge of these parameters is crucial for the experiment. For example, if the magnetic field orientation is perpendicular to the transparency beam propagation axis, both right and left-hand circular components (see subsection 2.2.2) will address the atoms with the same polarization decomposition and the architecture proposed in 2.2.2 would not break the two-photon coupling (see subsection 2.2.1). Therefore, we calibrated the magnetic field orientation and amplitude.

To measure the magnetic field amplitude a cloud of ^{88}Sr atoms is loaded into the reservoir trap. We then take in situ images of this cloud using the $^1S_0 - {}^3P_1$ transition. We recorded the absorption spectra for the magnetic $^1S_0 - {}^3P_1$ transitions at different coil currents. An example of such data for a single coil is shown in figure 2.10 (a). The transition frequency is plotted in dependence of the magnetic field in figure 2.10 (b) for the three sets of coils used. Finally, the magnetic field amplitude and orientation can be extracted as $\{B_x, B_y, B_z\} = \{m_x \cdot (I_x - I_{x,0}), m_y \cdot (I_y - I_{y,0}), m_z \cdot (I_z - I_{z,0})\}$. Here $\{I_x, I_y, I_z\} = \{1.3, 1, 1.25\}$ A are the coil currents, $\{m_x, m_y, m_z\} = \{0.314(2), 0.414(2), 0.762(2)\}$ G $\cdot$ A^{-1} and

---

[6]Our experiment can produce a BEC in steady-state or time-sequentially, the latter using conventional evaporation ramps. The experimental complexity is much higher for the former than for the latter. Therefore we favor the time-sequential mode of operation for system characterization.
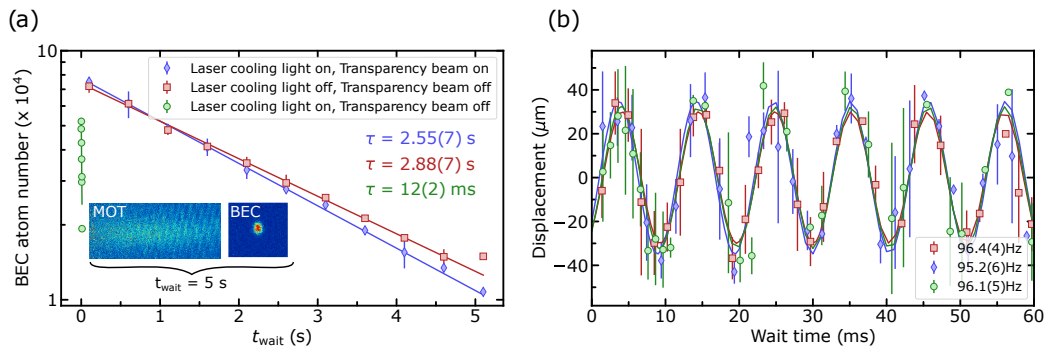
FIGURE 2.9: (a) BEC lifetime under the presence of transparency light and the laser-cooling light used in the CW BEC experiment (blue diamonds). The inset shows images of a BEC (left) and a red MOT (right). The red MOT loading starts at $t_{wait} = 0$, when the laser cooling light is switched on again after BEC creation. The MOT is separated from the BEC by a distance of ~ 4 cm. For comparison the vacuum lifetime is also shown (red squares). When the laser cooling light is on and the transparency light is off the lifetime of the BEC is shorter (green circles) (b) Horizontal trap frequency measurements of the transparency beam when used as a dipole trap. The trap frequency is determined by center of mass oscillations. Each of the shown measurements employs different drives or trapping potentials. Measuring under these conditions firstly ensures that the measured trap frequency corresponds to the radial waist of the transparency beam and not the trap created by the reservoir and secondly that the measurement does not depend on the modulation drive. The reservoir powers are 500 mW (green circles) and 700 mW (blue diamonds and red squares) and the center of mass oscillations are driven by modulating the reservoir power by 180 mW (green circles), 230 mW (blue diamonds) or modulating the transparency power (red squares). In both figures, the shown error bars give the standard deviation from averaging two to four data points.
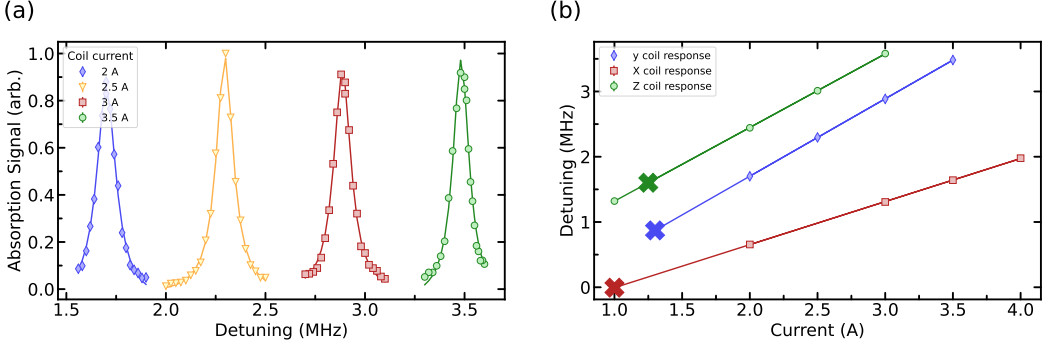
(a)

(b)

FIGURE 2.10: Magnetic field calibration protocol. (a) Absorption spectra of the magnetic $^1S_0 - {}^3P_1$ $m_J = +1$ transition at different vertical coil currents. (b) The measured current-frequency response for the three pairs of coils used. The crosses show the extrapolated Zeeman shift used in the steady-state configuration. The resulting magnetic field measurement is $\{B_x, B_y, B_z\} = \{0.003(6), 0.414(3), 0.762(3)\}$G, where the given errors reflect the statistical uncertainty of the data. Here we use a time-sequentially loaded cloud of ^{88}Sr atoms in the reservoir trap and three sets of coils in Helmholtz configuration that are mostly oriented along the x, y or z axis. The rest of the magnetic coils' currents are set to their steady-state value.

$\{I_{x,0}, I_{y,0}, I_{z,0}\} = \{1.01(1), 5.66(5), 1.69(6)\}$A are the currents needed to zero the magnetic field at the location of the BEC, see figure 2.10. For the typical currents of the experiment we obtain $\{B_x, B_y, B_z\} = \{0.003(6), 0.414(3), 0.762(3)\}$G. Note that the presented errors result from statistical uncertainty of the data. However, the magnetic field calibration suffers from systematic errors. These errors occur due to external long-term fluctuations of the magnetic field, frequency offsets on the probing lasers, or light-shifts of the resonance frequency due to the dipole trap. Finally for these measurements the three sets of coils used are well oriented along the relevant axes and assume that the field they create in the transverse directions is negligible.

Transparency beam waist The transparency beam's waist is measured by characterizing the dipole trap potential created by this beam. Specifically, we measure the radial trap oscillation frequency by exciting center-of-mass oscillations of a pure BEC. To do this measurement, we first load a BEC into the trap created by the transparency beam and the reservoir trap. The reservoir trap is required to provide confinement in the vertical axis. We then drive the BEC motion by modulating the intensity of one of the trapping beams for 30-50 periods at different powers. We then stop the drive and measure the resulting time-dependent velocity of the condensate. The velocity is measured by switching the laser beams off and taking time-of-flight images (TOF) of the falling atoms after 20 ms. The resulting data is shown in figure 2.9 for different reservoir trap depths. Note that, due to

an offset in the alignment between the transparency and dimple beams with the reservoir, modulating these beams' trap depth can excite motion in the horizontal plane. From these measurements we obtain a radial trap frequency of 95.9(6) Hz at the used power of 6.4 mW. The resulting excitation frequency can be translated into a beam waist of 22.0(6) µm using the following set of equations:

$$2\pi \cdot \omega_{x,y} = \sqrt{\frac{4 \cdot U_0(w)}{m \cdot w^2}}, \qquad\qquad 2\pi \cdot \omega_z = \sqrt{\frac{2 \cdot U_0(w)}{m \cdot Z_r(w)^2}},$$

$$Z_r(w) = \frac{\pi \cdot w^2}{\lambda}, \qquad\qquad U_0(w) = \frac{1}{4\pi\epsilon_0} \cdot \frac{4 \cdot \alpha \cdot P}{c \cdot w}.$$

Here P is the laser beam power, m is the mass of the atom, λ is the wavelength of the light (688 nm), α is the atomic polarizability at the given wavelength [98], c is the speed of light in vacuum, ϵ_0 is the vacuum permittivity, $Z_r(w)$ is the Rayleigh length and U_0 is the dipole trap depth at its center.

Transparency-induced light shifts Finally, we measure the differential light shift induced on the $^1S_0 - {}^3P_1$ transition by the transparency beam for different transparency beam powers. The resulting data is shown in figure 2.12 and it is compared with our theoretical results from subsection 2.2.1.

To obtain this data we load a cloud of ^{88}Sr atoms into the reservoir and dimple trap. We illuminate the atoms with the transparency beam at different powers and take in-situ absorption pictures using the $^1S_0 - {}^3P_1$ transition for varying detuning. An example of such a measurement is shown in figure 2.11. At low probe detuning the reservoir atoms are clearly visible, and a dark region can be observed at the location of the transparency beam. This dark region results from the transparency beam shifting the probe transition out of resonance. At higher detunings, the light is no longer resonant with atoms in the reservoir but with atoms in the transparency beam region. Finally, the atoms are no longer resonant and the whole cloud becomes dark. This data allows us to estimate the light-shift created by the transparency beam, at the location of its highest intensity.

The resulting maximum light-shift is shown in figure 2.11 (a) for each of the m_J states in the $^3P_1$ manifold when using a single frequency protection scheme. The solid lines show the calculated maximum light-shift using the theory presented in 2.2.1, the measured waist of the transparency beam, and the calibrated magnetic field shown above. This theory has no free parameters and has a good qualitative agreement with the experimental data. A clear saturation can be observed. This saturation is resolved when using the dual-frequency configuration described in subsection 2.2.2 (see figure 2.12 (b)).
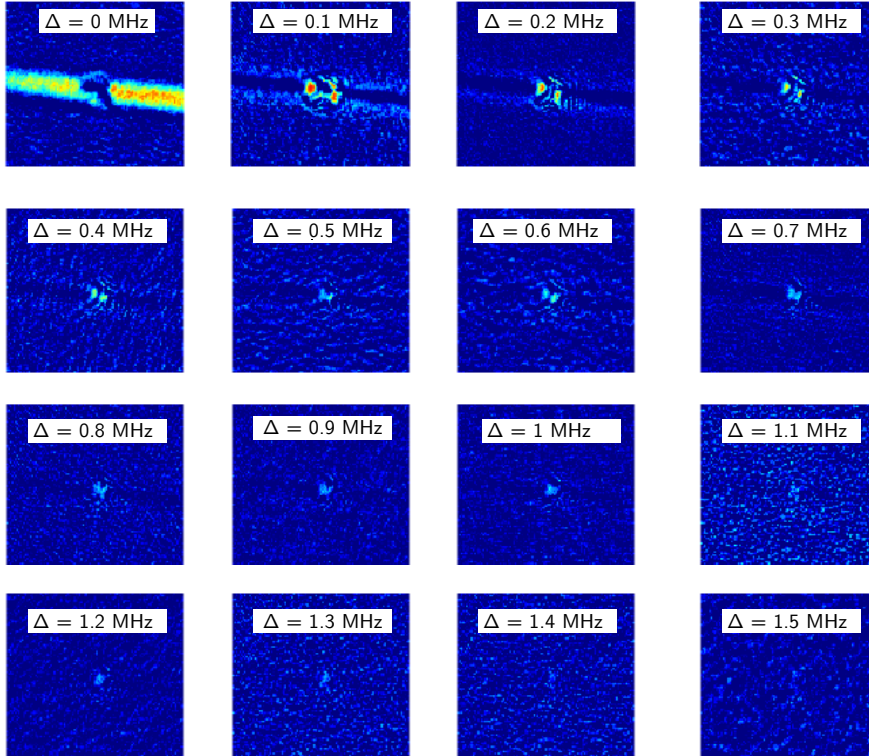
FIGURE 2.11: Potential landscape tomography. Here we record the absorption images of a time-sequentially loaded cloud of ^{88}Sr atoms for different detunings from the unperturbed $^1S_0 - {}^3P_1$ transition. The absorption images show the regions of space where the induced differential light shift compensates the probe detuning. At $\Delta = 0$, the atoms in the reservoir are resonant to the probe light. At the center of the reservoir the atoms are rendered transparent to the probe light by the transparency laser. At higher detunings ($\Delta > 0$) the reservoir atoms are no longer resonant to the probe light and only atoms in the transparency beam region can be observed. Due to the transparency beams' spatial profile first the atoms located at the edges of the beam are observed ($\Delta = 0.1 - 0.8$MHz), then atoms at the center of the beam where the light-shift is larger ($\Delta = 0.9 - 1.4$MHz), finally the probe beam is off-resonant with the whole cloud and no atoms are observed ($\Delta > 1.5$MHz).

FIGURE 2.12: Measurements of the transparency-induced light-shift on a cloud of ultracold ^{88}Sr atoms. (a) When using a single 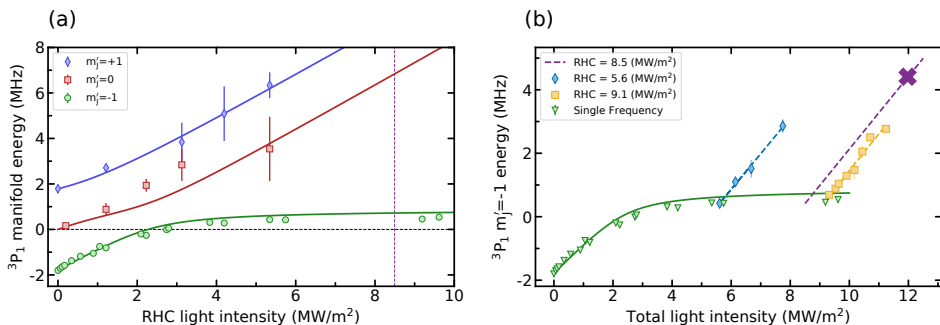frequency right-hand circular polarized configuration the light-shift induced on the $^{3}P_1$ $m_J = -1$ state saturates at high powers. The solid lines show the resulting light-shift according to the theory from subsection 2.2.1. The theory has no free parameters and shows a good qualitative agreement with the data. (b) Induced light-shift when addressing the atoms with two frequency components and orthogonal polarizations. The blue diamonds and the yellow squares show the measured shift for different initial right-hand circular component intensities, $5.6\,\mathrm{MW \cdot m^{-2}}$ and $9.1\,\mathrm{MW \cdot m^{-2}}$ respectively. Here the two-photon coupling is suppressed and the induced light-shift grows linearly with the laser intensity. The purple cross shows the estimated operation condition used in reference [37]. For reference the single frequency condition of the $m_J = -1$ state is also shown (green triangles).

2.3 Loading and cooling the reservoir

To produce a CW BEC in the dimple trap enough atoms at sufficiently cold temperatures need to be brought into the reservoir trap. Our initial expectations for the required atom number and temperature were based on thermal distributions. This approximation was inaccurate, giving us misleading theoretical results. Ultimately we found that, compared to thermal distributions, an increase of the overall atomic density of around one order of magnitude was required.

Indeed, to achieve a CW BEC several improvements of the reservoir loading performance compared to what is reported in references [35, 36, 44, 89, 99] were required. Here we detail the most relevant improvements. We start in subsection 2.3.1 by further detailing the loading and cooling of the reservoir and dimple traps supplementing the information given in section 2.1. We continue in subsection 2.3.2 by describing how the laser cooling condition of the reservoir was optimized. Finally, in subsection 2.3.3 we show how the overall flux of atoms reaching the reservoir was improved.

2.3.1   Overview

As described in subsection 2.1.3 atoms from the high-PSD beam are continuously loaded into the reservoir trap. The reservoir trap is radially cooled by three laser beams, two in the horizontal direction and one in the vertical direction. To compensate for the differential light shift induced by the 1070 nm trap, which peaks at 55 kHz in the trap center, these beams are slightly blue detuned (42 kHz) from the unperturbed transition. This detuning choice allows for efficient cooling at the trap center. However, at the edges of the trap the light is blue detuned, inducing heating of the atoms. Since high-temperature atoms are more likely to explore the edges of the trap, this radial cooling also acts as a form of induced evaporation.

Unfortunately, as atoms load the reservoir trap, they must travel through the blue detuned region, where radial cooling induces heavy losses. Indeed comparing the atomic flux arriving in the reservoir ($1.0(2) \times 10^6$ atoms/s), with the atomic flux from the guide ($9(1) \times 10^6$ atoms/s) shows that around 85% of the atoms from the beam are lost.

In the axial direction, atoms are cooled by a set of two counter-propagating beams addressing the $^1S_0 - {}^3P_1\ m_J = -1$ transition. The magnetic transition allows us to select a spatial region where atoms are cooled down and brought to near standstill. From this region atoms diffuse to the center of the trap. With this cooling scheme the final temperature in the radial direction is $T_{\text{radial}} = 0.85(7)\,\mu K$ and in the axial direction $T_{\text{axial}} = 3.0(5)\,\mu K$.

Atoms that reach the center of the reservoir trap can enter the dimple beam. The dimple is a tightly focused 1070 nm, 130 mW vertically propagating beam with a waist of 27 μm and a trap depth of 7 μK. The dimple region is rendered transparent to laser-cooling light by the transparency beam (see section 2.2.2) so the energy of the incoming atoms must be removed by elastic collisions between atoms in the reservoir and atoms in the dimple.

We are able to load $N = 6.9(4) \times 10^5$ atoms at a temperature of $T = 1.08\,\mu K$ into the dimple beam. Assuming thermal equilibrium, the expected number of atoms in the BEC $N_{\text{BEC,thermal}}$ follows [100]

$$T_c = 0.94 \cdot \hbar\omega_{\text{ho}} \cdot N^{\frac{1}{3}}, \qquad\qquad \frac{N_{\text{BEC,thermal}}}{N} = 1 - \left(\frac{T}{T_c}\right)^3.$$

Here $\omega_{\text{ho}} = (\omega_x \cdot \omega_y \cdot \omega_z)^{1/3} = 2\pi \cdot 425\,\text{Hz}$ is the geometric average of the trap frequencies.

Using these equations we obtain an expected number of BEC atoms of $N_{\text{BEC,thermal}} = 5.5 \times 10^5$ atoms. By contrast, the actual number of atoms in the BEC is much lower, only $N_{BEC} = 74(23) \times 10^2$ atoms. This contrast shows that the population in the dimple is not

Laser	Lifetime (s)	Laser	Lifetime(s)
Background	8(6)	Radial x	3.8(1)
X MOT	4.5(4)	Radial y	2.3(1)
Y MOT	2.16(5)	Slower	1.81(6)
Z MOT	6.5(5)	Slower (II)	3.3(2)

TABLE 2.1: Losses due to undesired scattering of the laser cooling beams: The table shows the lifetime of atoms in the reservoir when different laser cooling beams are turned on. To obtain this data, a cloud of ^{88}Sr atoms is loaded into the reservoir trap. Then the corresponding laser beam is switch on and after a given wait time the atom number is measured. Finally an exponential decay is fitted to the data. The table gives the $1/e$ lifetime of these atoms while the respective beam powers can be found in appendix reference[37]

in thermal equilibrium. Indeed, initial expectations based on thermal distributions can be misleading. Even though we placed considerable effort into ensuring that the cooling and thermalization of reservoir and dimple atoms was efficient, we found that an increase of the dimple atom number of around an order of magnitude compared to thermal predictions was required to achieve a BEC in steady state.

2.3.2 Reservoir losses

Atoms inside the dimple beam are protected from laser cooling light thanks to the transparency beam, while in the reservoir trap atoms are cooled down by laser cooling light. Scattering from different laser beams can lead to high losses of atoms in the reservoir. Key to achieving a CW BEC is to reduce undesired atom losses inside the reservoir trap while maintaining efficient cooling, allowing to achieve colder and denser samples closer to thermal equilibrium.

These losses arise mostly due to the undesired scattering of laser-cooling light. To characterize them we measured the lifetime of atoms in the reservoir trap in the presence of different laser cooling beams. Surprisingly, we found that the vertical MOT beam was the largest source of losses of atoms in the reservoir. Indeed, even though the beam does not spatially overlap with the reservoir trap (see figure 2.13), unwanted scattering and reflections inside the vacuum chamber severely limited the measured lifetime to less than $0.5(1)$ s. After a careful realignment of this beam to avoid these reflections the lifetime was improved. Other beams, like the Z-MOT beam, have significant overlap with the reservoir trap, so their frequency is tuned to avoid the spectral region where reservoir atoms are resonant, see figure 2.13.
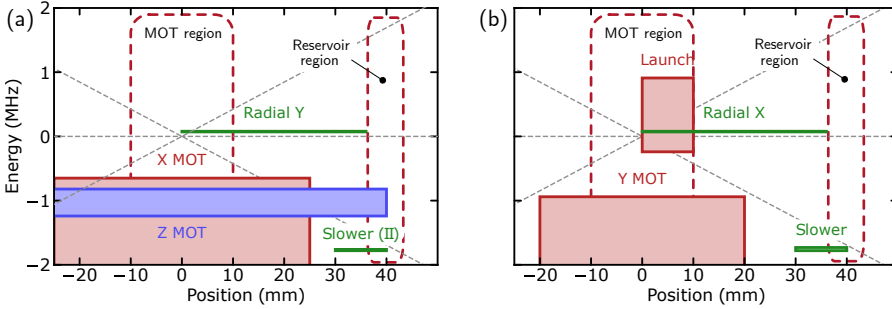
FIGURE 2.13: Spatial and spectral overlap of each of the laser cooling beams shown in section 2.1. The horizontal axis shows the position along the z-axis. The filled squares show the approximate resonance windows of different laser cooling beams. These windows are defined by the approximate spatial extent of the beam along the z direction (width of the rectangle) and the frequency span of the beam (height of the rectangle). The grey dashed lines show the spatially-dependent energy of the magnetic $^3P_1$ states. The red dashed lines show different spatial regions. (a) shows the X and Z MOT beams, the vertical radial cooling beam, and the counterpropagating slower beam (designated as Slower II). (b) shows the vertical MOT beam, the launch beam, the horizontal radial cooling beam (radial X) and the slower beam.

Finally, the radial cooling and the slower beams must address atoms within or close to the reservoir region so losses are harder to avoid. The losses generated by the axial beams (see subsection 2.1.3) can be minimized by tuning the reservoir trap polarization to maximize the trap's light-shift on the $^1S_0 - ^3P_1$ $m_J = -1$ magnetic transition. We recorded absorption spectra of reservoir atoms, similarly to how it is shown in subsection 2.2.3, and tuned the polarization of the light right-hand-circular to maximize the light-shift.

The radial cooling beams must address atoms inside the trap, so losses are much harder to avoid. The losses become stronger as the light addresses atoms closer to the bottom of the trap. The detuning choice is therefore a trade-off between efficient and fast cooling and inducing low losses. In table 2.1 we give the reservoir lifetime at the operation conditions of these beams. At higher blue detunings, when atoms are addressed close to the trap center, this lifetime can become much shorter.

In the future, the losses arising from the radial cooling beams could be further reduced by using a magic-wavelength reservoir trap. For such a trap the differential light-shift of the $^1S_0 - ^3P_1$ transition would be zero, and therefore the laser cooling beams could be tuned to the red of the transition.

Another more subtle source of losses arises when atoms are entering the dimple region. Inside the dimple the transparency beam light-shifts the $^1S_0 - ^3P_1$ transition far out of resonance and protects the BEC from scattering photons (see section 2.2). Unfortunately,
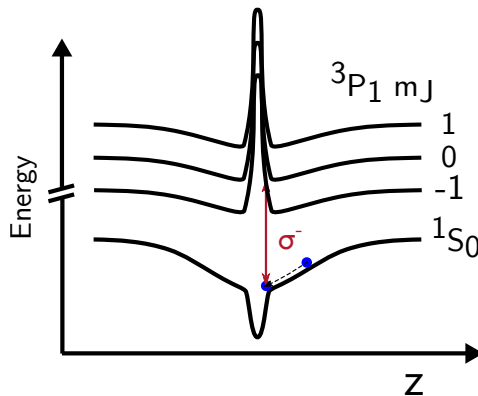
FIGURE 2.14: Undesired scattering of atoms entering the dimple region.
As atoms enter the dimple region, the transparency beam can bring the
$^1S_0 - \, ^3P_1 \; \sigma^-$ transition into resonance resulting in undesired losses.

at the edges of the dimple beam, the transparency beam is less intense and atoms can
be brought within resonance of the $^1S_0 - \, ^3P_1 \; \sigma^-$ transition. We minimize this effect by
carefully matching the polarization of the radial cooling beams as close as possible with the
local quantization axis given by the magnetic field to suppress excitation of this transition.
Additionally, the increase of the transparency beam laser intensity reported in section 2.2
reduces the size of the interaction region and helps to mitigate this effect.

2.3.3   Reservoir atomic flux

During the course of this thesis, we placed considerable effort into increasing the atomic flux
in the experiment. These efforts increased the overall flux into the lower chamber by more
than two orders of magnitude and were the final ingredient required to achieve steady-state
condensation. Note that, for each of the experimental stages preceding the reservoir, the
atomic collision rate is relatively small and one-body losses are dominant, see reference [36].
Therefore, the overall flux arriving in the reservoir and the PSD is proportional to the input
flux into the lower chamber.

To achieve higher atomic flux we first analyzed the power-vs-flux dependence of all
the laser-cooling beams in the upper chamber, see section 2.1. Our results showed that, for
all of the laser cooling beams in the upper chamber, except the Zeeman slower beam, an
increase in power did not yield a flux increase.

Initially, the Zeeman-slower light was produced by a single 100 mW blue diode from
Nichia (*NDB4216*). By focusing the laser light to a smaller spot size matching the oven's
aperture, we could increase the flux arriving in the lower chamber by a factor of ~ 40
compared to using a collimated beam, which had erroneously been used before. To ensure

that this measurement was done correctly, we inserted two removable lenses into the experiment and positioned them to slightly reduced the size of the beam at the oven aperture compared to its size at the 2D MOT location. Then we measure the flux into the steady-state MOT for different lens locations corresponding to different beam sizes at the oven location. Afterwards we removed the lenses and measured the MOT flux again. To rule out experimental degradation, we inserted back both lenses, set them for the optimal beam size, and measured the flux again. We repeated this protocol with different isotopes yielding similar results. We also upgraded our source by using 500 mW diodes recently available from Nichia (*NDB4916E*) [101]. In this way we were able to further increase the atomic flux by a factor of ~ 7.

Additionally we worked on a novel repumping scheme for strontium MOTs addressing the $^1S_0 - {}^1P_1$ transition. This work has been covered in detail in reference [99] and is only briefly mention here. In a nutshell, these MOTs feature losses as the cooling transition is not fully closed [87] and atoms can populate the $^3P_2$ excited state through the $^1P_1 - {}^1D_2 - {}^3P_2$ decay channel. This state is long-lived so these atoms are lost from the cooling transition. Typically different repumping transitions can be used to bring these atoms back to the ground state. For such schemes the repumping speed is limited by the decay time of the $^1D_2 - {}^3P_2$ transition of ~ 0.3 ms. Typically, for long lived MOTs, where lifetimes are much longer than 1 ms, this repumping speed does not limit the performance of the MOT. However, the lifetime of atoms in our 2D MOT (see 2.1.1) is much shorter, so the repumping speed is a stronger issue. To achieve a faster repumping speed, we address the 448 nm $^1D_2 - 5s8p^1P_1$ transition. This transition has a linewidth of 3 MHz so repumping is much faster. For our implementation this novel scheme resulted in a further increase of flux of a factor of ~ 1.4 for bosons and a factor of ~ 1.1 for fermions.

2.4 Publication: Continuous Bose-Einstein condensation.

Chun-Chia Chen [1] , Rodrigo González Escudero [1] , Jiří Minář [2,3], Shayne Bennetts [1] , Benjamin Pasquiou [1] and Florian Schreck [1]

[1] *Van der Waals-Zeeman Institute, Institute of Physics, University of Amsterdam, Science Park 904, 1098XH Amsterdam, The Netherlands*

[2] *Institute for Theoretical Physics, Institute of Physics, University of Amsterdam, Science Park 904, 1098XH Amsterdam, The Netherlands*

[3] *QuSoft, Science Park 123, 1098XG Amsterdam, The Netherlands*

Bose-Einstein condensates (BECs) are macroscopic coherent matter waves that have revolutionized quantum science and atomic physics. They are essential to quantum simulation [102] and sensing [45, 63], for example underlying atom interferometers in space [103] and ambitious tests of Einstein's equivalence principle [104, 105]. The key to dramatically increasing the bandwidth and precision of such matter-wave sensors lies in sustaining a coherent matter wave indefinitely. Here we demonstrate continuous Bose-Einstein condensation by creating a continuous-wave (CW) condensate of strontium atoms that lasts indefinitely. The coherent matter wave is sustained by amplification through Bose-stimulated gain of atoms from a thermal bath. By steadily replenishing this bath while achieving 1000x higher phase-space densities than previous works [34, 35], we maintain the conditions for condensation. This advance overcomes a fundamental limitation of all atomic quantum gas experiments to date: the need to execute several cooling stages time-sequentially. Continuous matter-wave amplification will make possible CW atom lasers, atomic counterparts of CW optical lasers that have become ubiquitous in technology and society. The coherence of such atom lasers will no longer be fundamentally limited by the atom number in a BEC and can ultimately reach the standard quantum limit [106–108]. Our development provides a new, hitherto missing piece of atom optics, enabling the construction of continuous coherent matter-wave devices. From infrasound gravitational wave detectors [6, 8] to optical clocks [20, 21], the dramatic improvement in coherence, bandwidth and precision now within reach will be decisive in the creation of a new class of quantum sensors.

Interferometers listen to gravitational waves, image the shadow of black holes, and are at the core of countless other high-precision measurements in science and technology. An interferometer achieves its outstanding sensitivity through the interference of waves. For example, the wave-like properties of matter are exploited in the world's most accurate sensors of acceleration and gravity [13]. Interferometers reach optimal sensitivity and bandwidth by using continuous, coherent, high-brightness sources, which is why many optical interferometers, such as LIGO, are based on CW lasers. However, no continuous matter-wave source with long-range coherence currently exists, which prevents atom interferometers from reaching their full potential. Creating such a CW source of matter will benefit applications ranging from geodesy [11, 109], to tests of Einstein's equivalence principle [104, 105], gravitational-wave detection [5, 6, 8, 110, 111], and dark-matter and dark-energy searches [112, 113].

The key to realizing a CW BEC of atoms is to continuously amplify the atomic matter wave while preserving its phase coherence [114]. An amplification process is essential to compensate naturally occurring atom losses, e.g. from molecule formation. It is also needed to replace the atoms that will be coupled out of the BEC for sustaining an atom laser or atom interferometer. Addressing this challenge requires two ingredients: a gain mechanism that amplifies the BEC and a continuous supply of ultracold atoms near quantum degeneracy.

The first steps towards a continuous gain mechanism were taken by [115], where merging of independent condensates periodically added atoms to an already existing BEC, but where coherence was not retained across merger events. A Bose-stimulated gain mechanism into a single dominant mode (the BEC) is required to provide gain without sacrificing phase coherence. Such gain mechanisms have been demonstrated using elastic collisions between thermal atoms [114, 116], stimulated photon emission [117], four wave mixing [118, 119] or superradiance [120]. However, in all these demonstrations the gain mechanism could not be sustained indefinitely.

To sustain gain the second ingredient is needed: a continuous supply of ultracold, dense gas with a phase-space density — the occupancy of the lowest motional quantum state — approaching $\rho = 1$. Great efforts were spent developing continuously cooled beams of atoms [31, 36] and continuously loaded traps [34, 35], which so far have reached phase-space densities of $\rho = 10^{-3}$. To achieve the required μK temperatures, these experiments have to use laser cooling, but near-resonant laser cooling light is highly destructive for BECs [26]. Several experiments have maintained a BEC in the presence of harmful light, either by spatially separating the laser cooling from the quantum gas [31, 35, 36, 115, 121] or by reducing the quantum gas' absorbance [27, 28, 114, 122].

Here we demonstrate the creation of a CW BEC that can last indefinitely. Our experiment comprises both ingredients, gain and continuous supply, as illustrated in Fig. 2.15. The
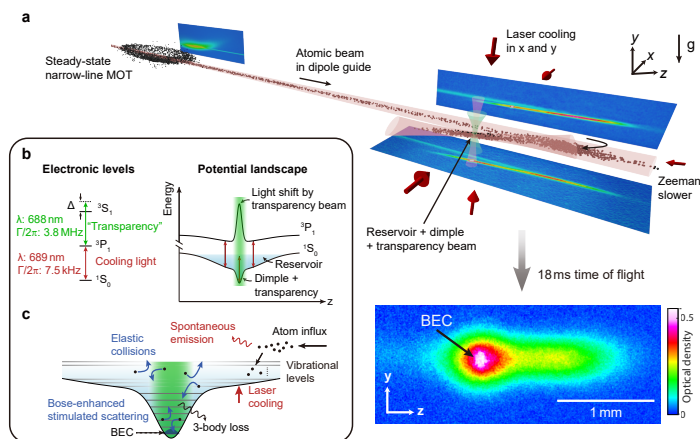
FIG. 2.15: | **Experimental setup and scheme. a,** ^{84}Sr atoms from a steady-state narrow-line magneto-optical trap (MOT) are continuously outcoupled into a guide and loaded into a crossed-beam dipole trap that forms a large reservoir with a small, deep dimple. Atoms accumulate in the laser cooled reservoir and densely populate the dimple, where a Bose-Einstein condensate (BEC) forms in steady state. After time-of-flight expansion, the BEC shows as an elliptical feature in the center of an absorption image. **b,** By off-resonantly addressing the $^3P_1 - {}^3S_1$ transition using a "transparency" laser beam, we produce a strong spatially varying light shift on the $^3P_1$ electronic state, rendering atoms locally transparent to laser cooling photons addressing the $^1S_0 - {}^3P_1$ transition. This enables condensation in the protected dimple region. **c,** Schematic of the potential landscape from both reservoir and dimple trap, and of the dominant mechanisms leading to BEC atom gain and loss.

centerpiece of the experiment consists of a large "reservoir" that is continuously loaded with Sr atoms and that contains a small and deep "dimple" trap in which the BEC is created. The gas in the reservoir is continuously laser-cooled, and exchanges atoms and heat with the dimple gas. A "transparency" beam renders atoms in the dimple transparent to harmful laser-cooling photons. The dimple increases the gas density while the temperature is kept low by thermal contact with the reservoir. This enhances the phase-space density, leading to the formation of a BEC. Bose-stimulated elastic collisions continuously scatter atoms into the BEC mode, providing the gain necessary to sustain it indefinitely.

Experiment

In order to continuously refill the reservoir, a stream of atoms from an 850 K-hot oven flows through a series of spatially-separated laser cooling stages. The initial stages load a steady-state magneto-optical trap (MOT) operated on the 7.5 kHz-narrow $^1S_0 - {}^3P_1$ transition [35], shown in Fig. 2.15a. An atomic beam of μK-cold atoms is then outcoupled and guided [36] 37 mm to the reservoir. This long-distance transfer prevents heating of the atoms in the reservoir by laser cooling light used in earlier cooling stages.

To slow the $\sim 10\text{-cm} \cdot \text{s}^{-1}$ atomic beam and load it into the reservoir while minimizing resonant light, we implement a Zeeman slower on the $^1S_0 - {}^3P_1 \, |m'_J = -1\rangle$ transition. This slower employs a single, counterpropagating laser beam together with the $0.23 \, \text{G} \cdot \text{cm}^{-1}$ MOT magnetic field gradient along the guide see 2.4. The 11.5 μK-deep reservoir is produced by a horizontal 1070-nm laser beam focused to an elliptical spot with waists $w_y = 14.5 \, \mu\text{m}$ vertically and $w_x = 110 \, \mu\text{m}$ horizontally. A 6° horizontal angle between the guide and reservoir allows the decelerated atoms to be nudged into the reservoir after reaching the intersection. The atomic beam and the reservoir are radially cooled by two pairs of beams addressing the magnetically insensitive $^1S_0|m_J = 0\rangle - {}^3P_1|m'_J = 0\rangle$ transition.

This arrangement of traps and cooling beams leads to the irreversible loading of the reservoir with a flux $\Phi_R = 1.4(2) \times 10^6 \, \text{atoms} \, \text{s}^{-1}$ see 2.4, a radial temperature of $T_{Rr} = 0.85(7) \, \mu\text{K}$, and an axial temperature of $T_{Rz} = 3.0(5) \, \mu\text{K}$. The corresponding phase-space flux is $\kappa = \left(\frac{\partial \rho_R}{\partial t} \right)_T = \Phi_R \left(\frac{\hbar^3 \omega_{Rx} \omega_{Ry} \omega_{Rz}}{k_B^3 T_{Rr}^2 T_{Rz}} \right) = 5.0(2) \times 10^{-2} \, \text{s}^{-1}$ [123], where $\hbar$ is the reduced Planck constant, k_B the Boltzmann constant, and $\omega_{Ri}/2\pi$ are the reservoir trap frequencies.

To reduce heating and loss we use a "transparency" laser beam [27] that renders atoms in the dimple trap transparent to near-resonant cooling light. This beam is overlapped with the dimple and its frequency is set 33 GHz blue detuned from the $^3P_1 - {}^3S_1$ transition, so as to locally apply a differential light shift on the $^1S_0 - {}^3P_1$ transition, see Fig. 2.15b and see 2.4. All transitions to the $^3P_1$ manifold are thereby shifted by more than 500 times the $^1S_0 - {}^3P_1$ linewidth, while atoms in the $^1S_0$ ground state experience a light shift of only
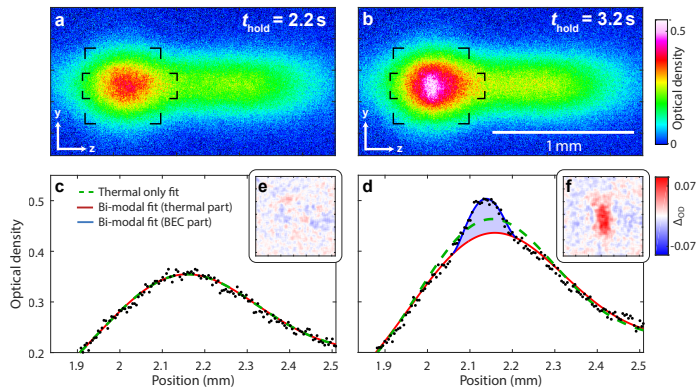
FIG. 2.16: | **Detection of the CW BEC. a**, **b**, Absorption images of the atomic cloud before and after condensation. The atoms are imaged after an 18 ms time-of-flight expansion. **c**, **d**, Optical density within the rectangles marked by corners in **a** and **b**, averaged along *y*. Fitted profiles using a thermal-only distribution (green dashed line) or a bi-modal distribution, consisting of a thermal (red line) and a Thomas-Fermi (blue line) component. The thermal-only fit fails to represent the condensed atoms in **d** (blue shaded area). **e**, **f**, Corner-marked square region of absorption images **a** and **b** minus thermal parts of the bi-modal fits, showing the continuous-wave BEC.

20 kHz. Without the transparency beam, the lifetime of a pure BEC in the dimple is shorter than 40 ms while with the transparency beam it exceeds 1.5 s see 2.4.

For a BEC to form in the dimple, the ultracold gas must exceed a critical phase-space density of order one. The dimple is produced by a vertically propagating 1070-nm beam with 27 μm waist focused at the center of the reservoir. In steady state the $6.9(4) \times 10^5$ atoms in the dimple are maintained at a low temperature ($T_D = 1.08(3)$ μK) by thermalization through collisions with the $7.3(1.8) \times 10^5$ laser-cooled atoms in the reservoir [27]. The dimple provides a local density boost, thanks to its increased depth (7 μK) and small volume compared to the reservoir [96, 124, 125]. This leads to a sufficient phase-space density for condensation.

In a typical instance of our experiment we suddenly switch all laser beams on and let atoms accumulate in the reservoir and dimple for a time t_{hold}. The phase-space density in the dimple increases and eventually a BEC forms. The BEC grows thanks to preferential Bose-stimulated scattering of non-condensed atoms into the macroscopically populated BEC mode. This produces continuous matter-wave amplification, the gain mechanism for the CW BEC [116]. The BEC grows until losses eventually balance gain and steady state is reached.

Analysis of the CW BEC

We now demonstrate the existence of a BEC and later show that it persists indefinitely. To tackle the first point we analyze atomic cloud density images for $t_{\text{hold}} = 2.2\,\text{s}$ and $3.2\,\text{s}$, immediately before and after the formation of a BEC, as shown in Fig. 2.16a, b. These x-integrated absorption images are taken after switching off all laser beams and letting the cloud expand for $18\,\text{ms}$. Both images show broad distributions of thermal atoms that are horizontally extended, reflecting the spatial distribution of the gas before expansion. Interestingly, the image for the longer t_{hold} shows a small additional elliptical feature at the location of highest optical density, which is consistent with the presence of a BEC. The appearance of a BEC is clearly revealed in Fig. 2.16c, d, showing y-integrated density distributions. For short t_{hold} only a broad, thermal distribution exists. However for long t_{hold} a bi-modal distribution appears, the hallmark of a BEC.

We further validate the BEC's existence by fitting theoretical distributions to the absorption images in Fig. 2.16a, b. As shown in Fig. 2.16c, d, excellent agreement is found by combining a thermal distribution with a Thomas-Fermi (TF) distribution describing the BEC. At short hold times, we find that a thermal fit alone is sufficient to describe the data, whereas at longer times the additional TF component is required, indicating the presence of a BEC. To clearly visualize the BEC, we remove the thermal fit component from the data, see Fig. 2.16e, f. The pronounced anisotropic shape of the BEC in Fig. 2.16f is consistent with the expansion of a BEC from the anisotropic dimple, whose trap frequency along the y axis is approximately double that along z see 2.4.

Once established, the BEC can be maintained in steady state indefinitely with gain balancing losses. As shown in Fig. 2.17, we study the formation transient and stability of the condensate by recording and analyzing images for different t_{hold}. Fig. 2.17a shows representative density profiles during the initial $5\,\text{s}$ formation transient (A-F) and then in the presence of a stable BEC (G-J). Likewise, Fig. 2.17b shows the evolution and then stability of the BEC atom number and the peak phase-space density in the dimple $\rho_D = N_D \left(\frac{\hbar^3 \omega_{Dx} \omega_{Dy} \omega_{Dz}}{k_B^3 T_D^3} \right)$, where N_D is the thermal atom number in the dimple and $\omega_{Di}/2\pi$ are the dimple trap frequencies. The steady-state BEC is observed over times much longer than both the lifetime of a pure BEC $(1.5 - 3\,\text{s})$ and the background-gas limited lifetime $(7\,\text{s})$ see 2.4.

Although we do not continuously monitor the continuous-wave BEC, its atom number fluctuations can be estimated from many independent observations. To study these fluctuations we collected ~ 200 measurements for $t_{\text{hold}} = 15\,\text{s}$, significantly longer than both the lifetimes in the system and the formation transient, see Fig. 2.17c. A BEC atom number of $\bar{N} = 7400(2300)$ is observed, with none of the points falling below our BEC detection threshold of 2000 atoms see 2.4.
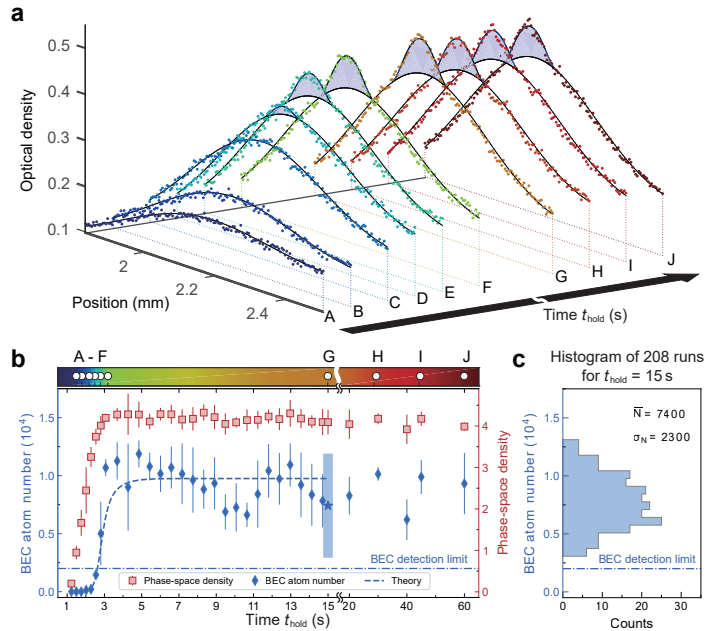
FIG. 2.17: | **Formation and stability of the CW BEC. a**, Profiles as in Fig. 2.16c,d for various hold times (marked in **b**) first during the formation of the BEC (A: 1.5 s, B: 1.8 s, C: 2.2 s, D: 2.5 s, E: 2.8 s, F: 3.2 s), then during the steady state of the continuous-wave BEC (G: 15 s, H: 30 s, I: 45 s, J: 60 s). **b**, Evolution of the BEC atom number and the dimple atom phase-space density ρ_D in dependence of hold time t_{hold} after suddenly switching all laser beams on. The dashed blue line shows the result of the BEC evolution fitted to the data before 15 s using the rate-equation model see 2.4. The error bars show the standard deviation from binning ~ 4 measurements for each time. **c**, Histogram of the BEC atom number from 208 images for $t_{\text{hold}} = 15$ s, long after the establishment of steady state (blue star in **b**). No points fall below our BEC detection limit of 2000 atoms. The 95 % confidence interval ($4\sigma_{\text{N}}$) calculated from this data set is given in **b** at 15 s (blue rectangle).

Modelling the formation, growth and stabilization of the BEC provides valuable insights into this new driven-dissipative system. It also provides the gain and loss from the BEC, which are important for practical applications such as producing a continuous-wave atom laser [117] and improving matter-wave coherence. We explain the BEC dynamics by fitting a phenomenological rate-equation model to measured temperature and atom numbers. Our analysis covers the condensate formation and perturbations such as disrupting the reservoir loading see 2.4. From this model we estimate a steady-state gain of $2.4(5) \times 10^5$ atoms s^{-1} into the BEC, with representative fits shown in Fig. 2.17b and Fig. 2.24. A substantial fraction of this gain could conceivably be translated into an outcoupled flux forming a CW atom laser. We also find that losses in the BEC at steady state are dominated by three-body recombinations with thermal atoms, due to the gas density exceeding 5×10^{14} atoms cm^{-3}. The presence of high, steady in-flux and loss makes our BEC a driven-dissipative system. We confirm this by showing that it is impossible to model the atoms in the trap as a closed system in thermal equilibrium see 2.4. Open driven-dissipative systems like this one are thought to exhibit rich nonequilibrium many-body physics waiting to be explored, such as purity oscillations [126], behaviors described by new critical exponents [127], and unusual quantum phases, especially in lower dimensions [128].

Discussion and conclusion

In summary, we have demonstrated continuous Bose-Einstein condensation. The resulting CW BEC can be sustained indefinitely using constant gain provided by a combination of Bose-stimulated scattering and atom refilling with high phase-space flux. Our work paves the way for continuous matter-wave devices, where matter-wave coherence is no longer limited by the atom number and lifetime of a single condensate [107]. In the near future, BEC purity and matter-wave coherence can be improved by enhancing the phase-space flux loading the dimple. A straight-forward option to achieve this is to render the reservoir laser cooling uniform by using a magic-wavelength reservoir trap. Further options include lowering the reservoir temperature by Raman cooling [28] or by adding a continuously operating evaporation stage [31]. Real-time non-destructive detection and feedback [129] can be used to stabilize the CW BEC atom number to a stability approaching the shot-noise level [130] and even beyond, leading to squeezed states [131] for measurements beyond the standard quantum limit [107].

Our CW BEC is the matter-wave equivalent of a CW optical laser with fully reflective cavity mirrors. A tantalizing prospect is to add an output coupler to extract a propagating matter-wave. This could be implemented by coherently transferring atoms to an untrapped state and would bring the long-sought CW atom laser finally within reach [22, 123]. This prospect is especially compelling because our CW BEC is made of strontium, the element used in some of today's best clocks [132] and the element of choice for future cutting-edge

atom interferometers [5, 6, 8, 110, 111, 133]. Our work will inspire a new class of such quantum sensors.

Author contribution C.-C.C. and S.B. built the apparatus. C.-C.C., R.G.E., and S.B. performed the investigation and data collection. C.-C.C., B.P. and S.B. analysed the data. J.M. developed the theoretical model. B.P., S.B., and F.S. supervised the project. F.S. acquired funding. All authors contributed to the manuscript.

Correspondence and requests for materials should be addressed to F.S. Raw data and analysis materials used in this research can be found at: https://doi.org/10.21942/uva.16610143.v1

Materials and methods

Creating an ultracold ^{84}Sr beam

We use the experimental scheme developed in our previous work [35, 36] to create an ultracold ^{84}Sr beam propagating within a dipole trap guide. The scheme begins with strontium atoms emitted by an 850 K-hot oven. They then travel through a succession of laser cooling stages arranged along multiple connected vacuum chambers using first the $^1S_0 - {}^1P_1$ and then the $^1S_0 - {}^3P_1$ transitions. Using the 30 MHz-wide $^1S_0 - {}^1P_1$ transition is necessary to efficiently slow and cool the fast atoms from the oven. However, this strong transition can't be used in the last chamber where the BEC is located, due to the likely heating of the BEC from scattered near-resonant photons. Cooling using the narrow $^1S_0 - {}^3P_1$ transition is however made possible in this last chamber thanks to the addition of a transparency beam (see below).

To form a guided beam, atoms arriving in the final vacuum chamber are first captured and cooled in a narrow-line magneto-optical trap (MOT). They are then outcoupled into a long, horizontal dipole guide with a 92 µm waist. The ^{84}Sr atoms propagate along the guide with a velocity $v_G = 8.8(8)$ cm $\cdot$ s^{-1}, a Gaussian velocity spread $\Delta v_G = 5.3(2)$ cm $\cdot$ s^{-1}, and a flux $\Phi_G = 8.6(1.0) \times 10^6$ atoms s^{-1}.

Making the reservoir and dimple traps

The 11.5 µK-deep reservoir is produced by a right circularly polarized 1070 nm laser beam propagating in the z direction. It uses 540 mW of power focused to an elliptical spot with waists of $w_y = 14.5$ µm vertically and $w_x = 110$ µm horizontally. The guided atomic beam and the reservoir intersect with a horizontal angle of 6°, about 1 mm from the reservoir center and 37 mm from the MOT quadrupole center. The reservoir beam crosses approximately 45(10) µm below the guide beam and descends with a vertical tilt of around 1.2(1)° as it separates from the guide beam. A secondary 250-mW beam of 175(25) µm waist runs parallel to the guide and points at the reservoir region. The fine adjustment of these beams is used to optimize the flow of atoms from the guide to the reservoir.

The dimple region has a 7 µK deeper potential located at the center of the reservoir. This is mainly produced by a vertically propagating 1070-nm "dimple beam", although 1 µK is due to the vertically propagating transparency beam. The dimple beam uses 130 mW of power linearly polarized along the z axis with a 27 µm waist in the plane of the reservoir. The dimple trap frequencies are $\left(\omega_{Dx}, \omega_{Dy}, \omega_{Dz}\right) = 2\pi \times (330, 740, 315)$ Hz, whereas the reservoir beam alone produces a trap with frequencies $\left(\omega_{Rx}, \omega_{Ry}, \omega_{Rz}\right) = 2\pi \times (95, 740, 15)$ Hz.

TABLE 2.2: | Properties of laser beams addressing the narrow-linewidth $^1S_0 - ^3P_1$ transition. Under "Detuning" $\Delta_1 : \delta : \Delta_2$ refers to a comb of lines from detuning Δ_1 to Δ_2 with a spacing of δ, obtained by triangular frequency modulation.

Beam name	Detuning (MHz)	Total power (µW)	$1/e^2$ radius (mm)	Comments
MOT X	$-0.66 : 0.015 : -2.2$	1.2×10^3	23.5	two counter-propagating beams
MOT Y	$-0.96 : 0.02 : -3.6$	11.3×10^3	34	single beam, upward propagating
MOT Z	$-0.825 : 0.017 : -1.25$	7	4	two counter-propagating beams
Launch	$+0.9 : 0.017 : -0.25$	20×10^{-3}	0.25	single beam
Zeeman slower	$-1.74 : 0.017 : -1.79$	4.5×10^{-3}	0.2	single beam
Counter Zeeman slower	$-1.77 : 0.017 : -1.79$	10.5×10^{-3}	0.15	single beam
Molasses X	$+0.042$	1.5	14.4	two counter-propagating beams
Molasses Y(up)	$+0.042$	3.5	18	single beam, upward propagating
Molasses Y(down)	$+0.042$	160×10^{-3}	19	single beam, downward propagating

Zeeman slower on the $^1S_0 - ^3P_1$ transition

To load the guided atomic beam into the reservoir it must first be slowed and pushed into the reservoir. To perform this task, we implement a Zeeman slower using the $^1S_0 - ^3P_1$ transition starting ~ 3 mm before the guide-reservoir intersection. The slower makes use of the quadrupole magnetic field of the narrow-line MOT to provide a magnetic gradient along the guide's axis. The MOT's quadrupole field has gradients of -0.55, 0.32 and $0.23 \, \text{G} \cdot \text{cm}^{-1}$ in the x, y, and z directions respectively. The slower is displaced by 37 mm along the z axis with respect to the quadrupole center, resulting in a magnetic field offset of 0.85 G. The slower uses a counter-propagating 200 µm-waist laser beam that crosses the guide at a shallow horizontal angle of $4°$. We modulate the laser frequency to broaden its effective linewidth to 50 kHz. This makes the slowing robust to potential fluctuations in the effective detuning (see Table 2.2). The light intensity corresponds to $2.2 \, I_{\text{sat}}$ when not frequency-broadened, where $I_{\text{sat}} \approx 3 \, \mu\text{W} \cdot \text{cm}^{-2}$ is the transition's saturation intensity. We choose the laser detuning to match the Zeeman shift of the $^3P_1 \, |J' = 1, m'_J = -1\rangle$ state at the intersection between the guide and reservoir. This way atoms reach zero axial velocity at the intersection before being pushed back and into the reservoir.

Loading the reservoir

Since the reservoir is a conservative trap, efficiently loading atoms from the guide requires a dissipative mechanism. This is provided in two ways by laser cooling on the $^1S_0 - ^3P_1$ transition. The first is a "counter Zeeman slower" beam propagating approximately along the z axis opposing the Zeeman slower beam. This beam addresses the $^3P_1 \, |J' = 1, m'_J = -1\rangle$ state with a peak intensity of $\sim 8 \, I_{\text{sat}}$ and has a waist of 150 µm. Making use of this magnetic transition, we choose the light detuning such as to address the atoms near the

guide-reservoir intersection and thus compensate the backward acceleration of the Zeeman slower beam. This allows atoms to gradually diffuse toward the reservoir center, where collisions and the second laser cooling mechanism will further lower their temperature.

The second cooling mechanism consists of a molasses on the radial axes (x, y) addressing the magnetically insensitive π transition. Using a magnetically insensitive transition avoids impacting cooling by the spatial inhomogeneities in the effective detuning due to magnetic field variation across the extent of the laser-cooled cloud. Another cause of spatial inhomogeneities, that does affect the molasses cooling efficiency, is the differential light shift induced by the reservoir trap. This shift is around $+55\,\mathrm{kHz}$, many times larger than the transition's linewidth. The optimal molasses cooling frequency is found to be $42\,\mathrm{kHz}$ higher than the unperturbed transition. This partially accommodates for the differential light shifts and preferentially cools atoms located near the bottom of the reservoir. To reach the lowest temperature and enable condensation in the dimple, we also apply a very low total light intensity of $0.4\,I_{\mathrm{sat}}$. With this choice of detuning and intensity, some of the incoming atoms reach the reservoir center where they are radially cooled to $T_{Rr} = 0.85(7)\,\mathrm{\mu K}$. Other atoms might be heated out of the $9\,\mathrm{\mu K}$-evaporation-threshold trap by the blue detuned light in the outer trap region.

Minimizing heating and loss in the reservoir

The atoms in the reservoir have a lifetime of $7\,\mathrm{s}$ limited by collisions with the background gas of the vacuum chamber. However, these losses can be overwhelmed by optical effects such as photo-association or heating by photon scattering. It is therefore critical to minimize the exposure of the reservoir to unnecessary light, and we address this point by implementing four techniques.

Firstly, the $37\,\mathrm{mm}$ offset between the MOT and reservoir centers allows us to avoid any direct illumination from the x, y MOT beams on the reservoir, see Fig. 2.18. On the z axis, the influence of the MOT beams is greatly reduced by using a "dark cylinder", as described in [36].

Secondly, we optimize the cooling spectrum and intensity of each laser cooling beam entering the last vacuum chamber. By separately measuring their influence on the reservoir atom number, we optimize on a compromise between the lifetime of atoms and the loading flux. The results are illustrated in Fig. 2.18 and Table 2.2.

Thirdly, we maximize the π polarization component of the molasses beams that illuminate both the guided beam and the reservoir, thus minimizing the effects of unwanted transitions. Unavoidably, beams along the y axis possess admixtures of σ^- and σ^+ due to the orientation of the local magnetic field.

Finally, we purify the spectrum of the light used to address the $^1\mathrm{S}_0 - {}^3\mathrm{P}_1$ cooling transition. Our cooling light is produced by multiple injection-locked diode lasers beginning

from a single external-cavity diode laser (ECDL). We reduce the linewidth of this ECDL to 2 kHz by locking it onto a cavity with a finesse of ~ 15000, whose spectrum has a full-width half maximum of ~ 100 kHz. By using the light transmitted through this cavity to injection lock a second diode laser, we can filter out the ECDL's amplified spontaneous emission and servo bumps. This filtering is critical to increase the atoms' lifetime inside the dimple by reducing resonant-photon scattering.

Without the dimple and transparency beams, individual laser cooling beams reduce the lifetime of atoms in the reservoir to no shorter than ~ 1.5 s. With the dimple, transparency and all laser cooling beams on, atoms in the reservoir have a $1/e$ lifetime of $420(100)$ ms, as determined from the fits shown in Fig. 2.19.

Transparency beam

To minimize the destructive effects of resonant light on the BEC and atoms within the dimple, we render this region locally transparent to light on the $^1S_0 - {}^3P_1$ cooling transition. By coupling light to the $^3P_1 - {}^3S_1$ transition, we induce a light shift on the $^3P_1$ state as illustrated in Fig. 2.20a,b. Due to the extreme sensitivity of the BEC to photon scattering, all sub-levels of the $^3P_1$ state must be shifted significantly. This requires using at least two of the three transition types $(\sigma^\pm, \pi)$ in this $J = 1 - J' = 1$ structure. However, when polarizations at the same frequency are combined, quantum interference between sub-levels always produces a dark state in the dressed $^3P_1$ manifold. In this case the energy of this dark state can only be shifted between $\pm\Delta_{\text{Zeeman}}$, where Δ_{Zeeman} is the Zeeman shift of the $^3P_1$ $m'_J = 1$ state. This corresponds to $\Delta_{\text{Zeeman}} = 1.78$ MHz at the dimple location, giving a light shift that is insufficient to protect the BEC. Thus it is necessary to use different frequencies for the different polarization components of the transparency beam, as illustrated in Fig. 2.20c.

The transparency beam is implemented by a single beam propagating vertically and focused on the dimple location with a 23 μm waist. This geometry aims to minimize the overlap of the transparency beam with the reservoir volume. In this way, we protect atoms at the dimple location without affecting the laser cooling taking place in the surrounding reservoir. This is necessary to maintain the reservoir's high phase-space flux. The transparency laser light is blue detuned by 33 GHz from the 3.8 MHz-wide $^3P_1 - {}^3S_1$ transition at 688 nm. It contains two frequency components, 7 mW of right-hand circularly polarized light and 3 mW of left-hand circularly polarized light separated by 1.4 GHz. The magnetic field at the dimple location lays in the (y, z) plane and has an angle of 60° with respect to the vertical y axis along which the transparency beam propagates. This leads to a distribution of the light intensity onto the transitions $\{\sigma^+, \sigma^-, \pi\}$ of $\{1, 9, 6\}$ for the left-hand and $\{9, 1, 6\}$ for the right-hand circular polarization.

The light is produced from a single external-cavity diode laser, frequency shifted by acousto-optic modulators and amplified by several injection-locked laser diodes and a
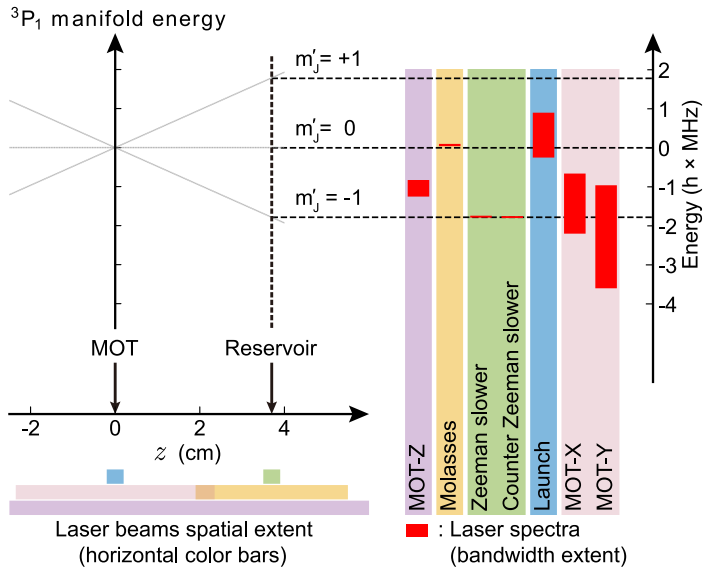
FIG. 2.18: | **Spectra of narrow-linewidth cooling lasers, and their spatial
extent.** The right side represents the spectra of cooling lasers addressing the
$^1S_0 - {}^3P_1$ transition (vertical red bars) with respect to the (relative) energy
of the states in the $^3P_1$ manifold, shown on the left side. The energies of
these m'_J states are given depending on the location along the z axis, and
the horizontal black dashed lines represent their respective Zeeman shifts
when atoms are located inside the reservoir. The horizontal color bars at the
bottom left show the location and spatial extent of each laser beam, see also
Table 2.2 for detailed beam parameters.
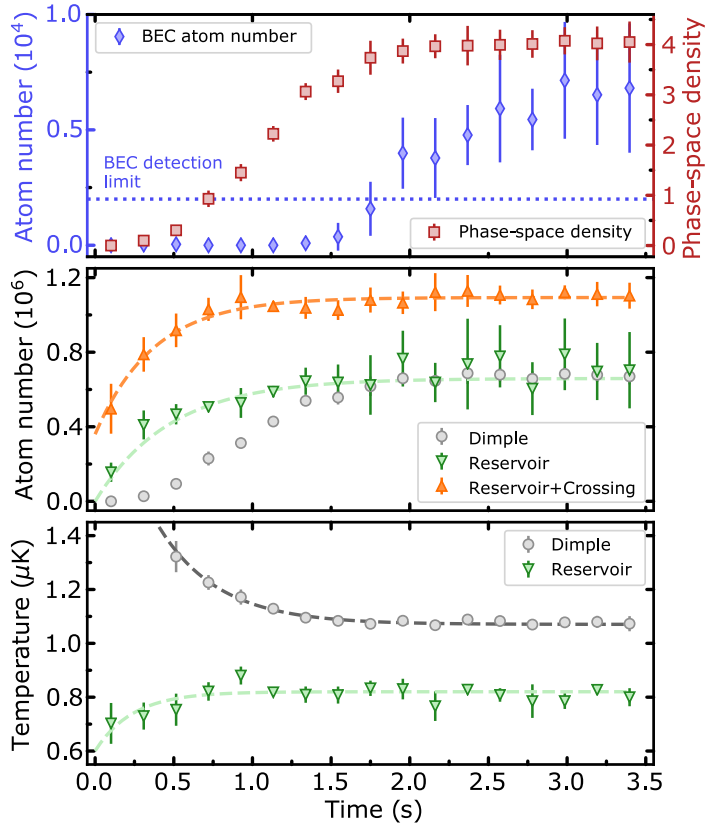
FIG. 2.19: |**Loading of the reservoir and dimple at constant flux.** We achieve a constant flux Φ_G in the guide by switching the experiment on for 10 s without the Zeeman slower beam, until reaching a steady flow. We then switch this beam on at time $t = 0$. We show (top) the BEC atom number and the phase-space density ρ_D in the dimple. The blue dotted line indicates our BEC detection limit in terms of condensed atom number. We show (middle) the dimple, reservoir, and "reservoir+crossing" atom number, and we show (bottom) the temperature T_D in the dimple and the temperature T_{Ry} in the reservoir along the vertical axis. The dashed lines are the results from fits with exponential growth or decay, giving access to the (constant) fluxes, one-body loss rate parameters, and thermalization times (see text). Error bars represent one standard deviation σ from binning on average 6 data points.
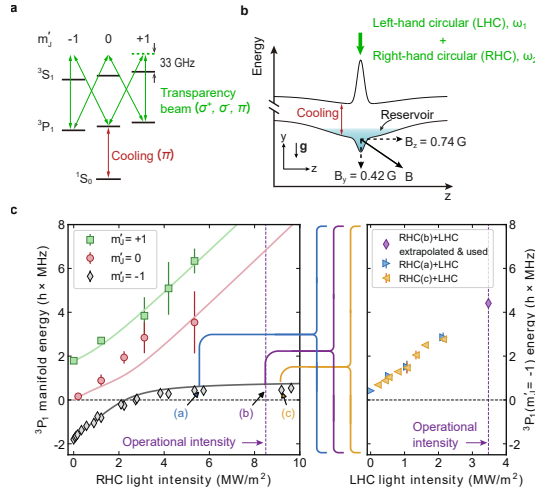
FIG. 2.20: | **Light shift from the transparency beam. a**, Level scheme showing laser cooling and transparency transitions. **b**, Schematic of the potential energy landscape of reservoir and dimple for the $^1S_0$ and $^3P_1$ states. Atoms are rendered insensitive to the laser cooling light by a single vertical "transparency" laser beam (green arrow), containing two frequency components, one for each circular polarization. **c**, Transition energies to the three $m'_J = 0, \pm 1$ Zeeman sub-levels of the $^3P_1$ manifold, referenced to the transition at zero electric and magnetic field (black dashed line). The energy shifts are shown for a single right-hand circular (RHC) polarization (left) and with the addition of the left-hand circular (LHC) component (right). We show the solutions (solid lines) of the Schrödinger equation for the $^3P_1$ manifold coupled by a light field with single frequency component and RHC polarization. In this case, at high laser intensities, the energy of the state originating from $m'_J = -1$ saturates, corresponding to the presence of a dark state. The purple vertical dashed lines show the operational intensities of the LHC and RHC light fields used in the CW BEC experiment, and the purple diamond is extrapolated from the data.

tapered amplifier. Since the $^1S_0 - {}^3P_1$ and $^3P_1 - {}^3S_1$ lines are less than 1.5 nm apart, it is crucial to filter the light to prevent amplified spontaneous emission from introducing resonant scattering on the $^1S_0 - {}^3P_1$ transition. This filtering is performed by a succession of three dispersive prisms (Thorlabs PS853 N-SF11 equilateral prisms), followed by a 2.5 m (right-hand circular) or 3.9 m (left-hand circular) propagation distance before aperturing and injection into the final optical fiber.

Characterizing the transparency beam protection

The transparency beam induced light shifts on the $^1S_0 - {}^3P_1$ transition were measured spectroscopically by probing the absorption of ^{88}Sr samples loaded into the dimple. ^{88}Sr is used instead of ^{84}Sr since the higher natural abundance improves signal without affecting the induced light shifts. Spectra are recorded for various transparency beam laser intensities at the magnetic field used for the CW BEC experiments. The results are shown in Fig. 2.20c for one then two polarization components.

The observed light shifts are consistent with the calculated dressed states for the six coupled sub-levels of the $^3P_1$ and $^3S_1$ states. This is evaluated by solving the Schrödinger equation in the rotating frame of the light field for a transparency beam consisting of a single frequency, right-hand circular laser beam in the presence of the measured external magnetic field. The theoretical results are given in Fig. 2.20c (solid lines, left side) with no adjustable parameters. We find a reasonable agreement with the observed shifts and reproduce the expected saturation of the light shift due to the presence of a dark state. An optimized fit can be obtained with a slightly higher intensity corresponding to a waist of 21 µm instead of 23 µm, and a slightly modified polarization distribution. In this fitted polarization distribution, the contribution of the weakest component, σ^-, is enhanced by a factor of roughly 2.5. Both differences can be explained by effects from the vacuum chamber viewports and dielectric mirrors.

When the left-hand circular polarization component of the transparency beam is added, we observe in Fig. 2.20c (right side) that the "dark" state shifts linearly away. In this manner all sub-levels of $^3P_1$ can be shifted by more than 4 MHz, more than 500 times the linewidth of the laser cooling transition. For comparison, the light shift on the $^1S_0$ ground state from the transparency beam is 20 kHz, and at most 380 kHz by all trapping beams, about one order of magnitude smaller than the shift on $^3P_1$ states from the transparency beam.

We demonstrate the protection achieved by the transparency beam in two ways. Firstly, we measure the lifetime of a pure BEC inside the dimple in the presence of all light and magnetic fields used in the CW BEC experiments. This pure BEC is produced beforehand using time-sequential cooling stages. Once the pure BEC is produced, we apply the same conditions as used for the CW BEC, except that the light addressing the $^1S_0 - {}^1P_1$ transition is off, to prevent new atoms from arriving. Without the transparency beam the $1/e$ lifetime

of a pure BEC in the dimple can't even reach 40 ms while with the transparency beam it exceeds 1.5 s.

Secondly, we show the influence of the transparency beam on the existence of a CW BEC. Beginning with the same configuration as the CW BEC but without the transparency beam, steady state is established after a few seconds, with no BEC formed. We then suddenly switch the transparency beam on and observe the sample's evolution as shown in Fig. 2.21. While the reservoir sample seems unaffected, the dimple atom number increases by a factor of 6.4(1.8), indicating fewer losses. At the same time the sample (partially) thermalizes and a BEC appears after about 1 s. This demonstrates the critical importance of the transparency beam.

Characterizing the BEC and thermal cloud

To characterize the CW BEC and surrounding thermal cloud, we switch all traps and beams off, and perform absorption imaging. Fitting the expanding clouds' distributions allows us to estimate atom numbers and temperatures throughout the system, as well as the number of condensed atoms, all from a single image.

We begin with absorption images typically recorded after an 18 ms time-of-flight expansion. The observed 2D density distribution can be fitted by an ensemble of four thermal components plus an additional Thomas-Fermi distribution when a BEC is present. Three independent 2D Gaussian functions represent atoms originating from the dimple, the reservoir, and the crossing between the guide and reservoir. Atoms originating from the guide are represented along the guide's axis by a sigmoid that tapers off due to the effect of the Zeeman slower, and in the radial direction by a Gaussian profile. Examples are shown in Fig. 2.22.

We found this fit function with 18 free parameters to be the simplest and most meaningful one capable of representing the data. By combining knowledge of their distinct locations and/or momentum spreads, we can determine individually the populations and their characteristics. We find that the uncertainty in the fitted parameters is mostly insignificant compared to shot-to-shot variations in the data. An exception is distinguishing the population in the reservoir from the one in the guide-reservoir crossing region, where there is some ambiguity resulting in higher uncertainties. Both in the main text and these Materials and methods, the error bars indicate the standard deviation σ calculated from multiple images. While it is possible to estimate the temperatures in the y axis from a single fitted image, the initial cloud sizes in the z direction are large compared to the ballistic expansion. Thus we use a set of measurements with varying times of flight to estimate z axis temperatures.

When a BEC is present, it is necessary to add a Thomas-Fermi profile to the previously discussed fit function. The only additional free parameter used in the fit is the number
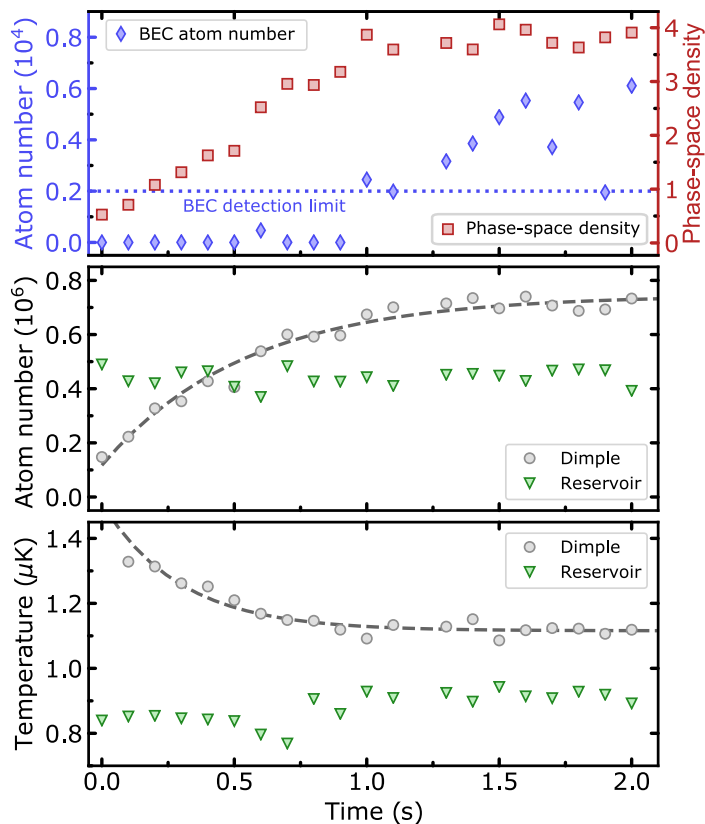
FIG. 2.21: | **Influence of the transparency beam.** We let the experiment reach a steady state with the transparency beam off. At $t = 0$ we switch the beam on and observe the system's evolution. We show (top) the BEC atom number and the phase-space density ρ_D in the dimple. The blue dotted line indicates our BEC detection limit in terms of condensed atom number. We show (middle) the dimple and reservoir atom number, and (bottom) the temperature T_D in the dimple and the temperature T_{Ry} in the reservoir along the vertical axis. Both atom number and temperature in the reservoir remain constant, while the dimple loads additional atoms, indicating lower losses thanks to the protecting effect of the transparency beam.
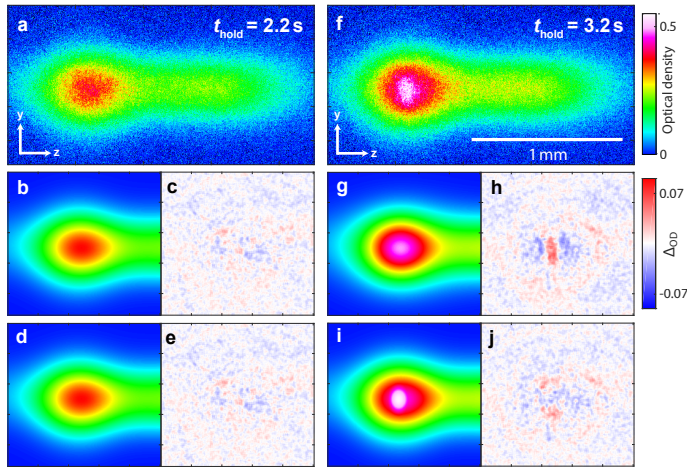
FIG. 2.22: | **Fitting a CW BEC.** We show absorption pictures and their respective fits for two hold times, before (left, $t_{hold} = 2.2\,$s) and after (right, $t_{hold} = 3.2\,$s) the formation of the BEC. In the top row, we show absorption pictures **a, f** taken after 18 ms time-of-flight expansion. In the middle row, we show results of fits **b, g** to these pictures, and the fit residuals **c, h**. The fits use a 2D density distribution fit function accounting only for a thermal cloud. By contrast, the bottom row shows both fits **d, i** and residuals **e, j** with a 2D density distribution fit function including a Thomas-Fermi distribution describing a BEC, in addition to the thermal distribution. In presence of a BEC, the residual of the thermal-only fit **h** clearly shows a discrepancy at the BEC location, while the residual **j** demonstrates that the fit accounts for the BEC.

of atoms in the BEC. We assume that the BEC position is the same as the one of the non-condensed atoms in the dimple and we calculate the BEC's radii from the BEC atom number, the *s*-wave scattering length, the trap frequencies in the dimple, and the expansion time [134]. These frequencies are calculated from the knowledge of the waists of each relevant beam and of the powers used. The waists are either directly measured or extracted from observations of dipole oscillation frequencies of a pure BEC in the trap for several beam powers.

Adding an additional fitting parameter can lead to overfitting. To rigorously determine whether including this Thomas-Fermi distribution provides a significantly better fit of the data, we employ a statistical *F*-test. This allows us to determine a BEC atom number threshold above which the fit is statistically better than the one without the Thomas-Fermi distribution. For this *F*-test we isolate a region of interest (ROI) in the image containing both thermal and BEC atoms. We then calculate the value $F = \frac{(RRS_1 - RSS_2)}{p_2 - p_1} / \frac{RSS_2}{n - p_2}$, where RRS_i is the residual sum of squares over the ROI for model i with p_i parameters, and n is the number of pixels of the ROI. The fit including the Thomas-Fermi distribution is significantly better than the one without, only if F is higher than the critical value of an *F*-distribution with $(p_2 - p_1, n - p_2)$ degrees of freedom, with a desired confidence probability. By applying this test to the data of Fig. 2.17, we find that the BEC model fits better, with a confidence greater than 99.5 %, when the BEC atom number exceeds 2000. This sets our detection limit, above which we are confident a BEC exists. Importantly, this limit is lower than the BEC atom number corresponding to a $-2\sigma_N$ shot-to-shot fluctuation. This indicates that, at all times after steady state is reached, a BEC exists.

Characterizing the reservoir loading
To estimate the flux Φ_R of atoms loaded into the reservoir we begin with all laser cooling and trapping beams on, except for the Zeeman slower beam. After some time, a steady state is reached, in which the guide is filled but not the reservoir. We then switch on the Zeeman slower beam, and observe the loading of the reservoir, see Fig. 2.19. Using our fitting procedure for the absorption images (see section "Characterizing the BEC and thermal cloud"), we estimate the growth in the number of atoms in various regions of the cloud. With the rough assumptions of a constant flux Φ_R and a one-body loss rate parameter Γ_{loss} originating for example from transfer of atoms to the dimple, the loading of the reservoir can be fitted by the exponential growth function $N_R(t) = (1 - e^{-\Gamma_{loss}t}) \Phi_R / \Gamma_{loss}$. This function fits best for a flux $\Phi_R = 1.4(2) \times 10^6$ atoms s^{-1}, see Fig. 2.19. We also show the combined number of atoms loaded in the reservoir and "crossing" (guide-reservoir intersection) regions. We fit this data with a similar exponential growth function, and obtain a flux of $2.9(3) \times 10^6$ atoms s^{-1}. The relative uncertainty of the combined atom numbers

is smaller than for the data set describing only the reservoir atom number. This is due to ambiguity between the "reservoir" and "crossing" regions in our fitting procedure.

Loading dynamics

The data of Fig. 2.19 show several timescales at play in the system's evolution. First we see atoms populating the reservoir. About 500 ms later the dimple region begins to fill. Finally about 1 s after the start of the dimple loading we see a BEC begin to form.

These dynamics can be understood from the thermalization timescale and from the need to exceed the critical phase-space density to begin forming a BEC. We estimate the peak phase-space density evolution by $\rho_D = N_D \left(\frac{\hbar^3 \omega_{Dx} \omega_{Dy} \omega_{Dz}}{k_B^3 T_D^3} \right)$, where N_D is the thermal atom number in the dimple. However, this estimation is inaccurate because of the non-thermalized distribution function describing the atoms in the dimple (see section "Modeling of the BEC's open dynamics" below). We give it here as an indication of the phase-space density, which with this definition and for a thermalized sample should be greater than 1.2 in order to produce a BEC.

Once the critical phase-space density is exceeded BEC formation begins at a slow rate and then accelerates as more atoms condense. Indeed, the growth of a BEC or matter-wave is governed by Bose-stimulated scattering, which scales with the number of atoms occupying the ground state of the trap [116, 119, 135, 136].

After about 3 s steady state is established. We probe the system for various hold times up to 5 min and find no indication that the BEC departs from steady state. This is exemplified in Fig. 2.19 and Fig. 2.17b.

BEC anisotropy after time-of-flight

A Bose-Einstein condensate and a thermal gas expand very differently when released from a trap. A thermal gas expands isotropically, beginning with a shape reminiscent of the initial trap geometry, and asymptotically approaching an isotropic shape for long times of flight (TOF). By contrast, the expansion of a BEC released from an anisotropic trap remains anisotropic for long TOF, inverting its aspect ratio mid flight. This originates from the anisotropic release of mean-field energy, which reflects the trap anisotropy [134].

The transpose-anisotropy provides an elegant method by which to efficiently detect the presence of a CW BEC. The transpose-anisotropy of the density distribution n_{OD} is $n_{\mathrm{OD}}^s (y, z) - n_{\mathrm{OD}}^s (z, y)$, where the origin of the coordinate system is at the density maximum. n_{OD}^s is obtained from n_{OD} by adding the same n_{OD} distribution rotated by 180°. Transpose-anisotropies for short (0.1 ms) and long (18 ms) TOFs are shown in Fig. 2.23. For 0.1 ms TOF, the density distribution shows a marked anisotropy as indicated by a strong cloverleaf pattern. This initial anisotropy is solely due to the action of the trap geometry on the density distribution of the thermal gas, as the size of a potential BEC is below our imaging resolution.
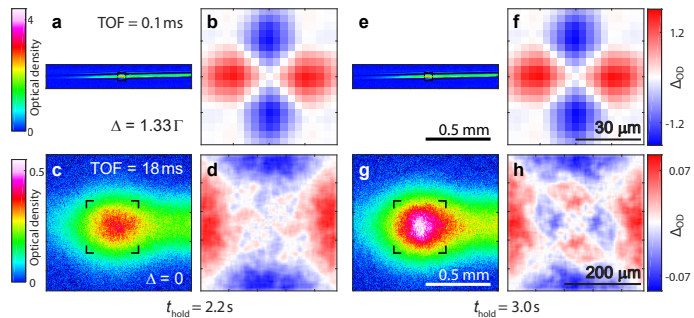
FIG. 2.23: | **BEC anisotropy after time-of-flight. a, e,** Absorption images after short (0.1 ms) and **c, g,** after long (18 ms) free-expansion time-of-flight (TOF), for short ($t_{\text{hold}} = 2.2$ s, **a, c**) and long ($t_{\text{hold}} = 3.0$ s, **e, g**) trap loading times. Pictures **a** and **e** were imaged with a detuning of $1.33\,\Gamma$ to avoid saturation. The regions of interest (corner-marked squares) centered around the density maximums are analyzed in panels **b, d, f, h,** which show the transpose-anisotropy of the density distribution. This representation produces a cloverleaf pattern when the atomic cloud is anisotropic (see text). For short t_{hold} (left), the cloverleaf pattern, which appears because of how the trap geometry initially shapes the thermal cloud, keeps a constant sign and diminishes during the expansion of a thermalized gas sample. For long t_{hold} (right), we observe at long expansion time **h** an additional smaller cloverleaf pattern of opposite sign, which is indicative of the presence of a BEC.

However, for 18 ms TOF we see a difference between pictures for short (2.2 s) and long (3.0 s) hold time t_{hold}. For short t_{hold} the anisotropy is broad and simply a remnant of the initial cloud anisotropy. However for long t_{hold}, at which steady state is established, we see an additional, smaller cloverleaf pattern with opposite anisotropy around the center of the picture. Both the existence and the sign of this pattern are consistent with the expansion of a BEC from a dimple with our trap frequencies.

Modeling of the BEC's open dynamics

In order to describe the formation and properties of the continuous-wave Bose-Einstein condensate, we develop a model capable of fitting our experimental data, as shown for example by the dashed blue line in Fig. 2.17b. In the following we describe the model and its results.

Firstly, we lay out the model, which builds on the standard Boltzmann kinetic theory of Bose gases with additional dissipation to account for the open dynamics. As a main result of our derivation we arrive at the rate equation Eq. (2.11). We provide details of the derivation of each gain and loss term in the equation and the assumptions that led to them.

Secondly, we discuss the fit of this model to our data, from which we extract useful physical quantities, like the 1- and 3-body loss rate parameters, and the flux into the CW

BEC after reaching steady state.

In particular, we find that we are not able to describe our data if we assume that our system is in thermal equilibrium. This reflects the intrinsic driven-dissipative nature of the system.

The model — We model the dynamics of the BEC using the rate equation

$$
\begin{aligned}
\dot{n}_{\mathrm{BEC}}(\mathbf{r}) &= s_{\mathrm{in}}(\mathbf{r}) - s_{\mathrm{out}}(\mathbf{r}) - \gamma_{\mathrm{1b}} n_{\mathrm{BEC}}(\mathbf{r}) \\
&\quad - \gamma_{\mathrm{3b}} \Big[n_{\mathrm{BEC}}(\mathbf{r})^3 + 6 n_{\mathrm{BEC}}(\mathbf{r})^2 n_{\mathrm{th}}(\mathbf{r}) \\
&\qquad + 6 n_{\mathrm{BEC}}(\mathbf{r}) n_{\mathrm{th}}(\mathbf{r})^2 \Big],
\end{aligned}
\tag{2.2}
$$

where $\gamma_{\mathrm{1b}}, \gamma_{\mathrm{3b}}$ are the phenomenological one- and three-body loss rate parameters, see [125], $n_{\mathrm{BEC}}, n_{\mathrm{th}}$ are the local densities of the BEC and thermal atoms in the dimple, and we do not write explicitly the time dependence of the variables. In the framework of kinetic Boltzmann equations, $s_{\mathrm{in}}, s_{\mathrm{out}}$ are the collisional integrals (source terms) describing the exchange between the thermal atoms and the BEC. To this end we follow closely the treatment in [137] and write (setting $\mathbf{v}_{\mathrm{BEC}} = 0$ in [137])

$$
s_{\mathrm{in}} = \frac{n_{\mathrm{BEC}} \sigma}{\pi h^3} \int \mathrm{d}\mathbf{p}_3 f_3 \frac{1}{v_3} \int \mathrm{d}\tilde{\mathbf{v}} f_4
\tag{2.3a}
$$

$$
s_{\mathrm{out}} = \frac{n_{\mathrm{BEC}} \sigma}{h^3} \int \mathrm{d}\mathbf{p}_2 f_2 \Delta v \int \frac{\mathrm{d}\Omega}{4\pi} (1 + f_3 + f_4),
\tag{2.3b}
$$

where $\sigma = 8\pi a_{\mathrm{sc}}^2$ is the s-wave scattering cross-section, $\Delta v = \sqrt{v_2^2 - 4v_0^2}$, $v_0 = \sqrt{g n_{\mathrm{BEC}}/m}$, $g = 4\pi\hbar^2 a_{\mathrm{sc}}/m$ and $\mathbf{p}_j = m\mathbf{v}_j$. Eq. (2.3a) describes the scattering of two thermal atoms with velocities $\mathbf{v}_3$ and $\mathbf{v}_4$ resulting in a BEC atom and a thermal atom with velocity $\mathbf{v}_2$; Eq. (2.3b) corresponds to the opposite process. In Eq. (2.3a) $\mathbf{v}_4 = \tilde{\mathbf{v}} + \frac{g n_{\mathrm{BEC}}}{m v_3^2} \mathbf{v}_3$ with $\tilde{\mathbf{v}} \perp \mathbf{v}_3$ such that the second integration is performed over the plane perpendicular to $\mathbf{v}_3$. In Eq. (2.3b) $\mathrm{d}\Omega$ denotes the solid angle subtended by $\mathbf{v}_3$ and $\mathbf{v}_4$. We use ^{84}Sr atomic mass m and its s-wave scattering length $a_{\mathrm{sc}} = 122.8\,a_0$, with a_0 the Bohr radius. $f_j = f(\mathbf{r}, \mathbf{p}_j)$ are the *unknown* distribution functions of the thermal atoms with the property $N_{\mathrm{th}} = \int \mathrm{d}\mathbf{r}\,\mathrm{d}\mathbf{p}/h^3 f(\mathbf{r}, \mathbf{p})$.

In principle, one could obtain f_j from complete N-body simulations [137] of the open system, accounting for the coupled dynamics between the reservoir, the dimple and the

BEC. While strongly desirable, such a study goes beyond the scope of the present analysis[7]. Instead, let us first assume a thermal equilibrium such that f is given by the Bose-Einstein distribution. In this case the total number of non-interacting atoms in a harmonic trap is given by $N_{\text{th}} = (\beta_D \hbar \omega_D)^{-3} \text{Li}_3 \left(e^{-\beta_D \mu} \right)$. Here μ is the chemical potential of the distribution, $\omega_D = (\omega_{Dx}\omega_{Dy}\omega_{Dz})^{1/3}$, $\beta_D = 1/k_B T_D$, and $\text{Li}_s(z)$ is a polylogarithm of order s. With the experimentally measured dimple trap frequencies and gas temperature, we find that even for the maximum allowed $\mu = 0$, the atom number only reaches $N_{\text{th}} \approx 1.8 \times 10^5$. This estimation is well below the measured value of $6.9(4) \times 10^5$ atoms in the dimple. To try to resolve this discrepancy, we perform a more refined calculation following [27], where the harmonic trapping potential is replaced by the combined potential of the reservoir and dimple traps, and where we account for the interactions between atoms. This calculation gives $N_{\text{th}} \approx 3.6 \times 10^5$ atoms in reservoir and dimple combined, which is less than those measured in the dimple, let alone in the reservoir and dimple combined ($1.4(2) \times 10^6$). Unsurprisingly, in this calculation most atoms are contained well within the dimple, as $k_B T_D$ is much smaller than the dimple depth. The refined approach is thus also incapable of reproducing the measured atom number. This is in direct contradiction with our previous analysis in [27]. There, the refined calculation was capable of accounting for all atoms in a trap with a similar geometry, but where the continuous refilling of the reservoir was absent. This difference leads us to conclude that the current system does not fulfill the thermal equilibrium assumption due to its open character, and that the population dynamics are governed by out-of-equilibrium distribution functions f.

To proceed, we assume that the distribution function can be written as a product

$$f(\mathbf{r}, \mathbf{p}) = n_{\text{th}}(\mathbf{r}) f'(\mathbf{p}). \tag{2.4}$$

We take $f'(\mathbf{p}) = \frac{1}{\mathcal{N}} e^{-\beta_D \frac{p^2}{2m}}$, $\mathcal{N} = \frac{4\pi}{(2\pi\hbar)^3} \sqrt{\frac{\pi}{2}} \left(\frac{m}{\beta_D} \right)^{\frac{3}{2}}$ to be the Boltzmann distribution, which fulfills the normalization property $\int \frac{d^3 p}{(2\pi\hbar)^3} f'(\mathbf{p}) = 1$. We next specify the densities $n_{\text{BEC}}(\mathbf{r})$ of the BEC and $n_{\text{th}}(\mathbf{r})$ of the thermal atoms appearing in Eq. (2.2). For the BEC we consider the Thomas-Fermi profile given by

$$n_{\text{BEC}}(\mathbf{r}) = n_0 \left(1 - \left(\frac{x}{R_x} \right)^2 - \left(\frac{y}{R_y} \right)^2 - \left(\frac{z}{R_z} \right)^2 \right),$$

$$\tag{2.5}$$

---

[7]In this context, a possibility is to consider instead a simpler ergodic description of the Bose-Einstein condensation [138–140]. However, our preliminary analysis indicates breaking of the ergodicity assumptions, thus requiring the complete N-body simulations.

where $R_\alpha = \sqrt{2\mu_D/m}/\omega_{D\alpha}$, $\mu_D = \frac{\hbar\omega_D}{2}\left(15N_{\text{BEC}}\frac{a_{\text{sc}}}{a_{\text{ho}}}\right)^{\frac{2}{5}}$, $a_{\text{ho}} = \sqrt{\frac{\hbar}{m\omega_D}}$, N_{BEC} is the total BEC atom number and $n_0 = \mu_D/g$. In the BEC region, the condensate atoms will repel the thermal ones resulting, to a good accuracy, in the characteristic parabolic profile

$$n_{\text{th}}(\mathbf{r}) \approx$$
$$n_{\text{th},0}\left[1 + \gamma_x\left(\frac{x}{R_x}\right)^2 + \gamma_y\left(\frac{y}{R_y}\right)^2 + \gamma_z\left(\frac{z}{R_z}\right)^2\right],$$

$$(2.6)$$

where $\gamma_\alpha = (n_{c,\alpha} - n_{\text{th},0})/n_{\text{th},0}$. Next, motivated by the approach in [27, 137], we determine the thermal densities in the center, $n_{\text{th},0} = n_{\text{th}}(0)$, and at the edge of the BEC cloud, $n_{c,\alpha} = n_{\text{th}}(R_\alpha)$ in the direction $\alpha = x, y, z$, self-consistently as

$$n_{\text{th}}(\mathbf{r}) = -\frac{1}{\lambda_{\text{dB}}^3}\text{Li}_{\frac{3}{2}}\left[-e^{-\beta_D(V(\mathbf{r})+2gn_{\text{BEC}}(\mathbf{r})+2gn_{\text{th}}(\mathbf{r})-\eta)}\right],$$

$$(2.7)$$

with $\lambda_{\text{dB}} = h/\sqrt{2\pi mk_B T_D}$ the thermal de-Broglie wavelength. Here, we need to stress that unlike in [27], the function in Eq. (2.7) is not the density corresponding to the thermal equilibrium of a Bose gas as that one fails to reproduce the observed number of thermal atoms N_{th}, see the discussion above Eq. (2.4). The function in Eq. (2.7) in fact corresponds to a Fermi-Dirac distribution, which however here does not have a particular physical significance. It should be seen as a convenient ansatz from which we extract $n_{\text{th},0}$ and $n_{c,\alpha}$, which has the advantage that it allows to match the observed number N_{th} for positive values of the parameter η [141].

The assumed prescription for $n_{\text{th}}(\mathbf{r})$ Eq. (2.7) is clearly an idealization. Despite this fact, the model yields a value for the three-body loss rate parameter γ_{3b} that is compatible with the values reported in the literature (see section *The results* below). We interpret this compatibility as indicating that the values of $n_{\text{th},0}$ and $n_{c,\alpha}$ extracted from Eq. (2.7) lie within a factor $O(1)$ from the actual experimental values.

Next, we turn to the evaluation of the collisional integrals Eqs. (2.3) using the distribution function Eq. (2.4) with the result

$$s_{\text{in}} = n_{\text{BEC}}n_{\text{th}}^2\sigma I_{\text{in}} \tag{2.8a}$$

$$s_{\text{out}} = n_{\text{BEC}}n_{\text{th}}\sigma I_{\text{out}}^{(1)} + n_{\text{BEC}}n_{\text{th}}^2\sigma I_{\text{out}}^{(2)}. \tag{2.8b}$$

Here, we have introduced the functions

$$I_{\text{in}} = \kappa v_0^2 K_1(\beta_D m v_0^2) \tag{2.9a}$$

$$I_{\text{out}}^{(1)} = \kappa \mathcal{N} e^{-\beta_D m v_0^2} v_0^2 K_1(\beta_D m v_0^2) \tag{2.9b}$$

$$I_{\text{out}}^{(2)} = 2\kappa j, \tag{2.9c}$$

where $\kappa = \frac{1}{h^3} \frac{1}{\mathcal{N}^2} \frac{8\pi m^3}{m\beta_D}$, K_1 is the modified Bessel function of the second kind, and

$$j(\mathbf{r}) = \int_{2v_0}^{\infty} dv_2\, v_2 e^{-\frac{\beta_D m}{2} v_2^2} \left[e^{-\frac{\beta_D m}{8}(v_2 - \Delta v(v_2))^2} - e^{-\frac{\beta_D m}{8}(v_2 + \Delta v(v_2))^2} \right], \tag{2.10}$$

which has to be evaluated numerically.

Ultimately, we are interested in the dynamics of the total number of the condensate atoms, which can be obtained by integrating Eq. (2.2) over the volume. To be able to carry out the final integration, we take the functions $I_{\text{in}}, I_{\text{out}}^{(1,2)}$ to be independent of the position[8]. Using the profiles (2.5),(2.6) we arrive at the final rate equation

$$\dot{N}_{\text{BEC}} = S_{\text{in}} - S_{\text{out}} - L_{1b} - L_{3b}^{(3)} - L_{3b}^{(2)} - L_{3b}^{(1)}, \tag{2.11}$$

where

$$S_{\text{in}} = n_0 n_{\text{th},0}^2 \sigma V^{(1,2)} I_{\text{in}} \tag{2.12a}$$

$$S_{\text{out}} = n_0 n_{\text{th},0} \sigma V^{(1,1)} I_{\text{out}}^{(1)} + n_0 n_{\text{th},0}^2 \sigma V^{(1,2)} I_{\text{out}}^{(2)} \tag{2.12b}$$

$$L_{1b} = \gamma_{1b} N_{\text{BEC}} \tag{2.12c}$$

$$L_{3b}^{(3)} = \gamma_{3b} n_0^3 V^{(3,0)} \tag{2.12d}$$

$$L_{3b}^{(2)} = 6\gamma_{3b} n_0^2 n_{\text{th},0} V^{(2,1)} \tag{2.12e}$$

$$L_{3b}^{(1)} = 6\gamma_{3b} n_0 n_{\text{th},0}^2 V^{(1,2)} \tag{2.12f}$$

In the above equations, we have introduced the volume integrals

$$V^{(p,q)} = 1/(n_0^p n_{\text{th},0}^q) \int d\mathbf{r} n_{\text{BEC}}(\mathbf{r})^p n_{\text{th}}(\mathbf{r})^q, \tag{2.13}$$

---

[8]In principle, they still depend on spatial coordinates through $v_0(n_{\text{BEC}}(\mathbf{r}))$. For the span of experimental values of $n_{\text{BEC}}(\mathbf{r})$, this leads to a maximum variation by a factor 0.7.

which evaluate to

$$V^{(1,1)} = 4\pi R_x R_y R_z \frac{2}{105}(7 + 3\bar{\gamma}) \tag{2.14a}$$

$$V^{(1,2)} = 4\pi R_x R_y R_z \frac{2}{315}(21 + 5G + 18\bar{\gamma}) \tag{2.14b}$$

$$V^{(2,1)} = 4\pi R_x R_y R_z \frac{8}{315}(3 + \bar{\gamma}) \tag{2.14c}$$

$$V^{(3,0)} = 4\pi R_x R_y R_z \frac{16}{315}, \tag{2.14d}$$

where

$$\bar{\gamma} = \frac{1}{3}(\gamma_x + \gamma_y + \gamma_z) \tag{2.15a}$$

$$G = \frac{1}{5}(\gamma_x^2 + \gamma_y^2 + \gamma_z^2) + \frac{2}{15}(\gamma_x\gamma_y + \gamma_x\gamma_z + \gamma_y\gamma_z). \tag{2.15b}$$

To fit the data, we take γ_{1b}, γ_{3b} in Eqs. (2.12c)-(2.12f) as free parameters and further parametrize Eq. (2.12a) and Eq. (2.12b) as

$$S_{\text{in}} = \alpha_{\text{in}} n_0 n_{\text{th},0}^2 \sigma V^{(1,2)} I_{\text{in}} \tag{2.16a}$$

$$S_{\text{out}} = \alpha_{\text{out}} \alpha_{\text{in}} (n_0 n_{\text{th},0} \sigma V^{(1,1)} I_{\text{out}}^{(1)} + n_0 n_{\text{th},0}^2 \sigma V^{(1,2)} I_{\text{out}}^{(2)}) \tag{2.16b}$$

with $\alpha_{\text{in}}, \alpha_{\text{out}}$ the fit parameters.

The results — We have simultaneously fitted 6 data sets of the onset of the BEC analogous to Fig. 2.17b, with slight variations in the experimental starting conditions. For each of these sets, we use as a known time-varying input our measurements of the time evolution of dimple atom number and temperature (see for example the exponential fits to the dimple data of Fig. 2.24). We use the rate Eq. (2.11) and require the fit parameters γ_{1b}, γ_{3b}, and α_{out} to be the same for all the data sets. Conversely, we allow independent variation for each data set of α_{in} and the initial BEC atom number $N_{\text{BEC}}(0)$, which provides the seed to Eq. (2.11).

From this single fit, we obtain the loss rate parameters $\gamma_{1b} = 6(2)\,\text{s}^{-1}$ and $\gamma_{3b} = 1.9(2) \times 10^{-29}\,\text{cm}^6/\text{s}$. The value obtained for γ_{3b} is compatible with the rough experimental values reported in the literature, namely $\approx 0.7 \times 10^{-29}\,\text{cm}^6/\text{s}$ in [142] and $1.4(3) \times 10^{-29}\,\text{cm}^6/\text{s}$. The latter value can be extracted from the data used in [143], where the standard deviation is derived from statistical uncertainty, without accounting for systematic effects. We also obtain the average flux into the CW BEC at steady state $\bar{S}_{\text{in}} - \bar{S}_{\text{out}} = 2.4(5) \times 10^5\,\text{atoms s}^{-1}$. In steady state, most of this incoming flux is compensated by the three-body losses involving
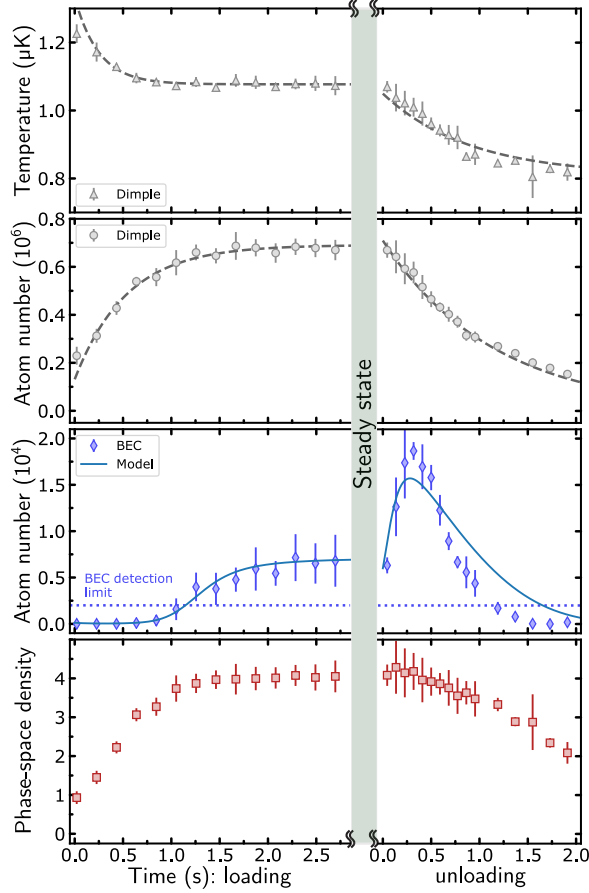
FIG. 2.24: | **Modeling the onset and disappearance of the BEC.** Evolution
of the gas in the dimple. (left) BEC onset when loading reservoir and dimple
at constant flux Φ_G in the guide, started by Zeeman slower switch-on at
$t = -0.7\,$s (same data as in Fig. 2.19, but choosing a different origin for the
time axis). (right) BEC disappearance after setting Φ_G to zero by switching
the Zeeman slower off. The first two rows show the temperature and atom
number of the thermal atoms in the dimple. The last two rows show the
BEC atom number and the estimated phase-space density ρ_D in the dimple.
The solid blue line is the result of the fit of the BEC atom number with the
model of Eq. (2.11). The dashed grey lines are results of fits with exponential
growth/decay functions, which are used as input for Eq. (2.11). Error bars
represent one standard deviation σ from binning ~ 4 data points. For the
BEC atom number, due to the small number of data points, the error bars can
be underestimated compared to the, more reliable, characterization at steady
state of $\sigma_N = 2300$ provided in the main text. The phase-space density ρ_D is
estimated from measurements of the atom number and temperature in the
dimple (see text).

thermal atoms described by Eqs. (2.12e) and (2.12f), while the loss mechanisms Eqs. (2.12c) and (2.12d) are only reaching a few 10^4 atoms s^{-1}. Finally, we extract from the fit additional information about the CW BEC, namely the Thomas-Fermi radii $\{R_{\text{TFx}}, R_{\text{TFy}}, R_{\text{TFz}}\} = \{2.8(1), 1.2(1), 2.9(1)\}\,\mu\text{m}$, the peak BEC density $n_0 = 3.6(2) \times 10^{20}$ atoms m^{-3} and the density of the thermal gas at the BEC center $n_{\text{th},0} = 3.6(1) \times 10^{20}$ atoms m^{-3}.

Fig. 2.24 shows example fits together with their corresponding experimental data sets. The left ("loading" stage) of Fig. 2.24 shows the onset and stabilization of the BEC following the switch on of the Zeeman slower beam. The right ("unloading" stage) of Fig. 2.24 shows the subsequent data after suddenly switching off the same beam. This corresponds to stopping the atomic flux into the reservoir and leads to the disappearance of the BEC. It is apparent that the rate equation Eq. (2.11) captures well the initial dynamics of the BEC atom number as well as the initial dynamics of the unloading stage. The discrepancy for longer times during the unloading stage can likely be attributed to the change of the momentum distribution functions $f(\mathbf{r}, \mathbf{p})$. This arises from the simultaneous thermalization and depletion of the dimple atoms, which is not captured by the parametrization of Eqs. (2.16).

In summary, the rate equation (2.11) provides a satisfactory fit to the data, from which we obtain the loss rate parameters γ_{1b}, γ_{3b} and the steady-state BEC flux rate $\bar{S}_{\text{in}} - \bar{S}_{\text{out}}$. A more comprehensive quantitative understanding may be provided through further analysis starting from first principles. Such an analysis requires more complex modeling of the coupled dynamics between the reservoir, the dimple, and the BEC, such as the use of the ZNG theory [144, 145] and the related N-body simulations [137].

Chapter 3

A steady-state magneto-optical trap of fermionic strontium on a narrow-line transition

During this thesis we developed a steady-state magneto-optical trap (MOT) of fermionic strontium operating on the 7.5 kHz $^1S_0 - {}^3P_1$ transition. To produce a such MOT we extended the experimental methods demonstrated for bosonic isotopes [35], to deal with the more complicated internal structure of the fermionic isotope. A noteworthy application of this research relates to steady-state superradiant lasers using fermionic strontium's $^1S_0 - {}^3P_0$ "clock" transition. The fermionic isotope is particularly interesting for these devices, because its clock transition is naturally open due to the presence of the nuclear spin (I = 9/2). In the bosonic isotopes, because of the absence of hyperfine interaction (I = 0), this transition is orders of magnitude weaker and probing it requires mixing of the 3_0^P state with 3_1^P or 1_1^P states, for example by applying a high external magnetic [146]. Therefore the technical requirements of a continuous-wave superradiant laser would be greatly simplified by using the fermionic isotope. Here we show how to create a continuous narrow-line MOT of fermionic strontium, which could be used to resupply a steady-state superradiant laser.

In this chapter, we describe the relevant experimental details on how to produce such a MOT and we outline its scientific importance. The main part of this chapter is based on reference [90] which we reproduce here. We have also included two addenda (B and A), which are not included in reference [90], and give supplementary information that might be useful to the reader:

For the convenience of the reader I would like to recall the structure of reference [90] included in this chapter:

- In section 3.1 we introduce this work, outlining its importance, and putting it into context.

- In section 3.2 we include a brief description of the experimental stages required to produce the MOT. Compared with the bosonic architecture, the ^{87}Sr MOT needs two additional components to deal with its more complex internal structure. These components are described in sections 3.3 and 3.4.

- Section 3.3 describes a 2D molasses that uses the sawtooth-wave adiabatic passage (SWAP) technique [147] to deal with the internal structure of ^{87}Sr. The SWAP molasses allows atoms to pass between two chambers and achieve efficient loading into the MOT.

- In Section 3.4 we describe a narrow-line slower that decelerates incoming atoms before they reach the MOT. To ensure efficient deceleration, optical pumping into addressed states of the $^1S_0$ F = 9/2 hyperfine manifold is required. This optical pumping is achieved by operating the slower in a dual-frequency manner, addressing two hyperfine transitions.

- In Section 3.5 we characterize the MOT. We measure its temperature, lifetime, size, density and atom number and give the relevant laser parameters required to produce it.

- Finally in section 3.6 we discuss the possible applications of this MOT, focusing on the application of this work to superradiant lasers.

  Finally, in addendum A we expand our discussion of the 2D SWAP molasses described in subsection 3.3. In particular, we show how cross-axis photon exchange can reduce the efficiency of SWAP cooling. We first recall the SWAP cooling principle, then give an intuitive explanation of how cross-axis photon exchange reduces SWAP's efficiency, and finally, we measure how this photon exchange is influenced by adding a time delay between the start time of the ramp time of each SWAP cooling arm. In addendum B we include the results of a Monte Carlo simulation of the system. We first benchmark our simulation comparing it to experimental data. Then we use this simulation to support some conclusions given in reference [90] and estimate different experimentally inaccessible quantities. In particular, we estimate the internal state distribution of atoms in the MOT, the temperature on the *x*-axis, [1] and the velocity-dependant capture probability of the slower stage.

---

[1]Because of experimental constrains we are not able to measure the MOT's temperature along this axis.

Steady-state magneto-optical trap of fermionic strontium on a narrow-line transition

Rodrigo González Escudero [1], Chun-Chia Chen [1], Shayne Bennetts [1], Benjamin Pasquiou [1] and Florian Schreck [1,2]

[1] *Van der Waals-Zeeman Institute, Institute of Physics, University of Amsterdam, Science Park 904, 1098XH Amsterdam, The Netherlands*
[2]*QuSoft, Science Park 123, 1098XG Amsterdam, The Netherlands*

A steady-state magneto-optical trap (MOT) of fermionic strontium atoms operating on the 7.5 kHz-wide $^1S_0 - ^3P_1$ transition is demonstrated. This MOT contains 8.4×10^7 atoms, a loading rate of 1.3×10^7 atoms/s, and an average temperature of $12\,\mu K$. These parameters make it well suited to serve as a source of atoms for continuous-wave superradiant lasers operating on strontium's mHz-wide clock transition. Such lasers have only been demonstrated using pulsed Sr sources, limiting their range of applications. Our MOT makes an important step toward continuous operation of these devices, paving the way for continuous active optical clocks.

3.1 Introduction

Optical atomic clocks [17] are proving to be powerful tools to answer fundamental questions in physics. They enable searches for dark matter [3, 4, 73], the study of gravitational waves [148], tests of general relativity [149, 150] or variations in nature's fundamental constants [74–76]. In the applied domain they are playing an increasingly important role in geology and geodesy [9–12].

Typically, state-of-the-art optical clocks operate in a time-sequential manner, with distinct phases for sample preparation and measurement. This time-sequential mode of operation introduces noise, known as the Dick effect [18], which limits their performance [19]. The Dick effect results from the down-conversion or aliasing of high-frequency noise, present in the laser used to interrogate the atoms, down to frequencies lower than the clock's interrogation frequency. To address it, several approaches have been followed: employing high-precision non-destructive detection techniques [64], developing novel experimental architectures to achieve high duty cycles [151] or interleaving the clock interrogations between two different atomic samples [53, 152, 153].

A new class of optical clocks based on the principle of superradiant lasing have been proposed as next-generation devices [20, 21]. Their working principle is inherently suited to continuous operation, thus circumventing the Dick effect. Furthermore, their potential goes beyond addressing this challenge: in the future they could outperform conventional clocks in terms of stability, detection bandwidth, and, by relaxing the requirements on external high-finesse cavities, portability and robustness [21, 154].

Pulsed superradiant lasing has already been demonstrated [155], in particular using strontium's $^1S_0 - {}^3P_0$ clock transition [81, 156]. There are ongoing efforts to incorporate steady-state atomic sources with this new type of clock [83, 84, 155, 157]. While there exist several strontium sources achieving the required flux and temperature [35, 36], all of these operate using bosonic isotopes, due to their simpler atomic structure. However, superradiant lasing using the clock line of bosonic strontium has, so far, not been demonstrated.

For bosonic strontium, the clock linewidth is orders of magnitude smaller than for its fermionic counterpart, and requires high external magnetic fields for the linewidth to be broadened enough for clock interrogation [146, 158]. Moreover, such fields must feature an exceptional degree of homogeneity and stability across the atomic sample for all atoms to participate in superradiant lasing [159]. Conversely, the laser cooling stages that are necessary to achieve the desired temperature and density operate best at low magnetic fields and gradients. These two adverse requirements complicate the integration of a steady-state source of bosonic strontium into an active optical clock. By contrast, a fermionic source seems better suited. Indeed, due to the non-zero nuclear magnetic moment of fermionic

strontium, the clock transition is naturally much stronger than for bosonic strontium [17, 160], making it accessible without the need for the high external magnetic fields that are typically required with bosons.

Here we demonstrate a continuously loaded magneto-optical trap (MOT) of ultra-cold fermionic ^{87}Sr atoms, operated on the 7.5 kHz-wide $^1S_0 - {}^3P_1$ inter-combination line. This narrow-line MOT contains $8.41(4) \times 10^7$ atoms at an average temperature of 12.0(1) μK, is loaded with a rate of $1.31(2) \times 10^7$ atoms/s and reaches a peak density of $2.12(4) \times 10^9$ ^{87}Sr/cm^3. This steady-state source could be used to provide the high flux of ultracold atoms necessary to refill the gain medium of a steady-state superradiant active clock [81, 154, 155].

This article is structured as follows. Section 3.2 briefly describes the experimental setup necessary to produce a continuous MOT of strontium using the $^1S_0 - {}^3P_1$ transition, while Sec. 3.3, 3.4, and 3.5 focus on the specificities pertaining to the fermionic isotope ^{87}Sr. Section 3.3 describes a 2D molasses, making use of the sawtooth-wave adiabatic passage (SWAP) technique to collimate an atomic beam passing from one chamber to the next. Section 3.4 describes a narrow-line Zeeman slower adapted to fermionic strontium, thanks to optical pumping into suitable states of the hyperfine manifold of ground-state strontium. Section 3.5 characterizes the MOT performance and directly compares the ^{88}Sr and ^{87}Sr cases. Lastly, Sec. 3.6 discusses the application of this atomic source to superradiant active optical clocks and concludes.

3.2 Apparatus overview

In this section we first outline the main components of our apparatus, by describing every laser cooling stage necessary to produce a continuous narrow-line MOT. We then highlight the main differences between steady-state narrow-line MOTs of ^{88}Sr (bosonic strontium) and ^{87}Sr (fermionic strontium).

Similarly to our previous work on bosonic strontium [35], we stream a beam of atoms through a sequence of spatially separated laser cooling stages, until reaching the μK regime. Initially, atoms coming from an oven at $\sim 550\,^\circ$C are slowed down by a Zeeman slower operated on the 30 MHz-wide $^1S_0 - {}^1P_1$ transition. For this work, we have upgraded the power of the Zeeman slower beam to improve our atomic flux by more than an order of magnitude, using 500 mW diodes now available from Nichia (Part NDB4916) [101]. The high cycling rate of the $^1S_0 - {}^1P_1$ transition is necessary to decelerate and cool a significant part of the velocity distribution of the beam exiting the oven. However, parasitic light resonant with this transition, coming, for example, from uncontrolled reflections or fluorescence from the laser-cooled atoms, will be extremely damaging to superradiantly

lasing ensembles and quantum degenerate gases [27, 37, 81]. It will also be harmful to the lifetime and temperature of our narrow-line MOT. To address these issues, we opted for a two-chamber design, consisting of an upper and a lower chamber, separated by ~ 40 cm, see Fig. 3.1. We use light addressing $^1S_0 - {}^1P_1$ in the upper chamber but not in the lower one. Indeed, by inducing a light shift on the $^3P_1$ excited state, the 7.48(5) kHz-wide [71, 161] $^1S_0 - {}^3P_1$ transition can be locally shifted out of resonance. In such a way, long-lived quantum degenerate gases can exist in the presence of laser cooling light addressing $^1S_0 - {}^3P_1$ transition [27, 37].

In the upper chamber, Zeeman slowed atoms are gathered in a 2D MOT using the $^1S_0 - {}^1P_1$ transition, see Fig. 3.1. This 2D MOT produces a vertical, downward propagating atomic beam with a radial velocity $\lesssim 0.5$ m $\cdot$ s^{-1}. In order to efficiently transfer atoms to the lower chamber through a 20 mm long, 8 mm-diameter baffle, this atomic beam requires collimation. In typical double-chamber experiments, this collimation can be achieved by accelerating the atoms exiting the 2D MOT to high velocities. However due to the low scattering rate of the $^1S_0 - {}^3P_1$ transition, we would not be able to stay below the capture velocity in the lower chamber. Thus, in order to achieve a high-transfer efficiency we need to provide additional radial cooling for the beam. We achieve this goal by employing a 2D molasses operating on the $^1S_0 - {}^3P_1$ transition and located directly below the 2D MOT.

Due to gravity, atoms accelerate and reach the center of the lower chamber, located ~ 40 cm below the 2D MOT, with a downward velocity distribution peaked at ~ 4 m $\cdot$ s^{-1}. A counter-propagating laser beam slows the atoms over a ~ 5 cm distance using the $^1S_0 - {}^3P_1$ transition. Finally, a narrow-line 5-beam 3D MOT using the same transition captures the atoms. The vertical, upward propagating beam serves a dual purpose, both slowing the atoms coming from the upper chamber and acting as a MOT beam. Once in the MOT, atoms are slow enough that gravity is sufficient to provide the downward restoring force.

The above description applies to our previous work on ^{88}Sr [35] and to our new work on ^{87}Sr described here. However, in order to deal with the internal structure of ^{87}Sr, our new architecture implements two key changes. Firstly, the collimating 2D molasses needs to be upgraded using the SWAP technique [162], to account for the magnetic sensitivity of all ^{87}Sr $^3P_1$ Zeeman sub-levels, see Sec. 3.3. Secondly, optical pumping into suitable states of the Sr $^1S_0$ hyperfine manifold is necessary to ensure efficient slowing of falling atoms in the lower chamber. We use additional laser light addressing the $^1S_0$ F = $9/2 - {}^3P_1$ F' = $9/2$ transition [163] to perform optical pumping thus enhancing the atomic flux into the MOT, see Sec. 3.4 and 3.5.
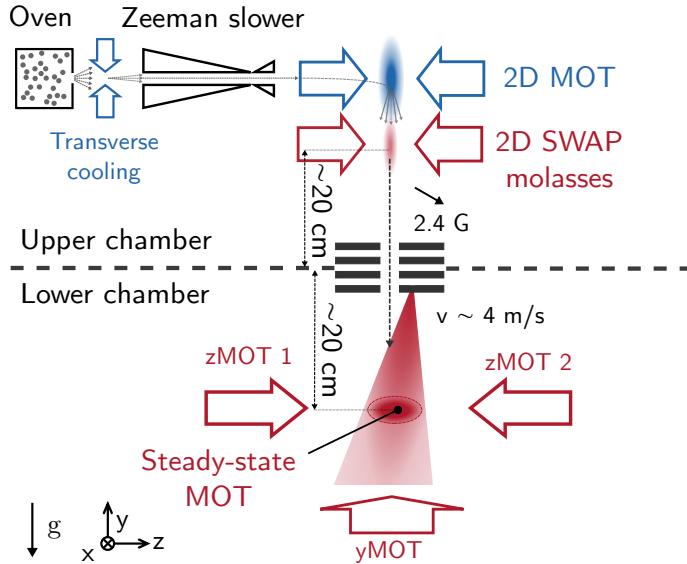
FIG. 3.1: Schematic of the apparatus producing a steady-state narrow-line MOT of fermionic ^{87}Sr. The top chamber features a 2D MOT using the 30 MHz-wide $^1S_0 - {}^1P_1$ transition, followed by 2D molasses using the 7.5 kHz-wide $^1S_0 - {}^3P_1$ transition. To account for both Doppler broadening and Zeeman shifts in the ^{87}Sr $^3P_1$ manifold, we use a variation of the SWAP molasses technique, see Sec. 3.3. In the lower chamber where the steady-state narrow-line MOT is produced, we use a dual-frequency scheme to both decelerate and capture the incoming atoms, see Sec. 3.4.

3.3 2D SWAP molasses

In this section, we describe how the 2D molasses using the narrow $^1S_0 - {}^3P_1$ transition collimates the atomic beam in order for the atoms to pass from the upper chamber to the lower chamber. We first detail how we previously achieved this collimation for bosonic ^{88}Sr, then highlight the additional challenges pertaining to fermionic ^{87}Sr. We resolve these challenges using SWAP cooling, a technique which uses sawtooth-shaped detuning ramps of the laser cooling light. We recall two criteria for this technique to work. We then explore its limits in our implementation and show that our 2D molasses performs better using SWAP laser detuning ramps rather than inverted SWAP or symmetric ramps. Finally, we measure and model the cooling efficiency of the 2D molasses in dependence of the laser powers and ramp durations.

3.3.1   SWAP molasses needed for fermionic Sr

The collimation molasses is located just below the broad-line 2D MOT that uses the $^1S_0 - {}^1P_1$ transition. It exploits the much lower Doppler temperature limit of the narrow-line $^1S_0 - {}^3P_1$ transition to further reduce the radial velocity spread of the downward propagating atomic beam, see Fig. 3.1. As atoms fall with a velocity of $\sim 3\,\mathrm{m \cdot s^{-1}}$, radial cooling with this 2D molasses reaches steady state in at most 10 ms. To achieve a sufficiently long interaction time the molasses beams are elliptical, with a $1/e^2$ diameter of 45.6 mm along the vertical axis and 18.2 mm along the horizontal axis.

   The molasses needs to address the atoms efficiently, despite a Doppler broadening about 100 times larger than the transition's natural width $\gamma = 2\pi \times 7.5\,\mathrm{kHz}$. For bosonic strontium we therefore broaden the molasses beams' frequency spectrum, forming a frequency comb spanning from 30 to 750 kHz to the red of the transition with a 25 kHz spacing [35]. An additional challenge arises from the presence of a residual 2D quadrupole magnetic field with a gradient of $2\,\mathrm{G \cdot cm^{-1}}$ at the location of the molasses. This field originates from the 2D quadrupole field of the nearby 2D MOT and it cannot be completely removed. This residual field leads to Zeeman broadening of the magnetic $^1S_0 - {}^3P_1$ transitions and position dependent light scattering forces. This challenge is overcome by addressing only the $|J = 0, m_J = 0\rangle - |J' = 1, m_{J'} = 0\rangle$, π, non-magnetic transition of ^{88}Sr. To this end, we add a vertical bias field of 1.2 G to Zeeman shift the other two, $\sigma^{\pm}$, transitions away from resonance, as the solution previously used in Ref. [35]. At the location of the atomic beam, the average field amplitude is 2.4 G, creating a Zeeman shift of about 5 MHz, a significant part of the field being along the z axis, see Fig. 3.1. The field orientation is not fully vertical because the atomic beam is displaced sideways with respect to the zero of the 2D quadrupole field, resulting in an additional component along the z axis.

   Due to the hyperfine structure of ^{87}Sr, non-magnetic transitions from $^1S_0$ to $^3P_1$ do not exist, see Fig. 3.2(a). Therefore, the method just described no longer provides efficient transfer of atoms to the lower chamber. To overcome this difficulty we use SWAP cooling [147, 162, 164–167], a technique that uses two rapid adiabatic passages to transfer atoms to a long-lived excited state and back to the ground state. In this work these states are $^3P_1$ and $^1S_0$ respectively. SWAP cooling exploits the time ordering of the adiabatic passages, transferring photons between two counter-propagating laser beams, and ensuring that the recoil momenta associated with photon absorption and stimulated emission are both oriented against the atoms' direction of travel, see Fig. 3.3. SWAP cooling has the advantage of robustly addressing a wide range of effective detunings, while increasing deceleration. Therefore it can be used on atomic samples whose Doppler broadening is much wider than the $^1S_0 - {}^3P_1$ transition's width, and it can address several transitions with distinct
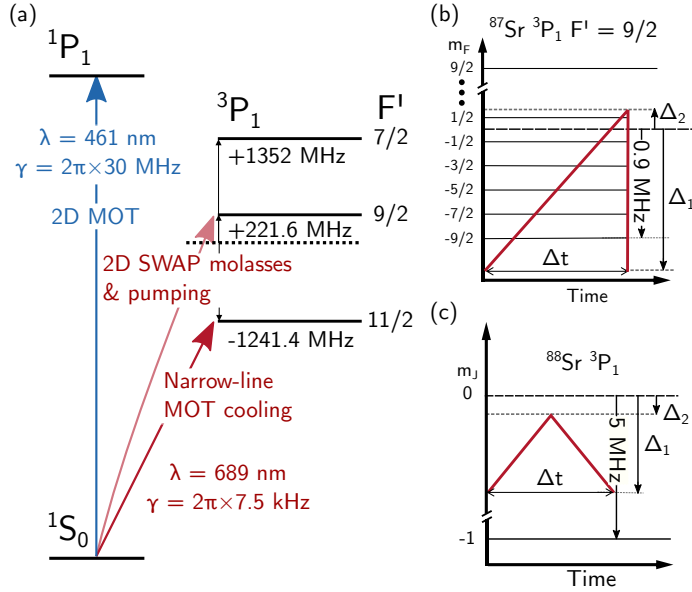
FIG. 3.2: (a) ^{87}Sr energy levels relevant for our experiment. The arrows indicate all transitions necessary to obtain our steady-state narrow-line MOT. The hyperfine shifts of the $^3P_1$ manifold are referenced to the single $^3P_1$ state of ^{88}Sr. (b) Magnetic sub-levels of the $^3P_1$ F' = 9/2 state for an atom at rest in presence of a field of 2.4 G. Also shown is a schematic of the detuning sweep (red lines) used by the 2D SWAP molasses to collimate the atoms propagating toward the lower chamber. (c) Schematic of the symmetric sweep used to collimate bosonic atoms [35]. The ramp parameters shown are the sweep duration Δt, the laser start detuning Δ_1 and stop detuning Δ_2.

differential Zeeman shifts in a single sweep.

3.3.2 SWAP cooling criteria

For SWAP cooling to be effective two main criteria must be fulfilled [147, 162]. The first is the adiabaticity of the rapid adiabatic passage from one internal state to the other, which is required for both absorption and stimulated emission. To be adiabatic, the square of the Rabi frequency of the laser light Ω^2 needs to be high compared to the laser detuning sweep rate α, i.e. $\kappa = \Omega^2/\alpha \gg 1$. Here $\alpha = \Delta\omega/\Delta t$, $\Delta\omega$ is the full detuning range spanned, and Δt is the duration of a single sweep. Indeed, for a Landau-Zener type crossing the probability of transfer is given by $P_{LZ} = 1 - \exp(-\pi\kappa/2)$ [147, 168].

The second criterion concerns the time an atom must spend in the excited state in order to perform a complete cycle of absorption and stimulated emission. This time must be smaller than the natural decay time by spontaneous emission $1/\gamma$. If this criterion is not met, spontaneous emission will occur before the stimulated emission, reducing the cooling
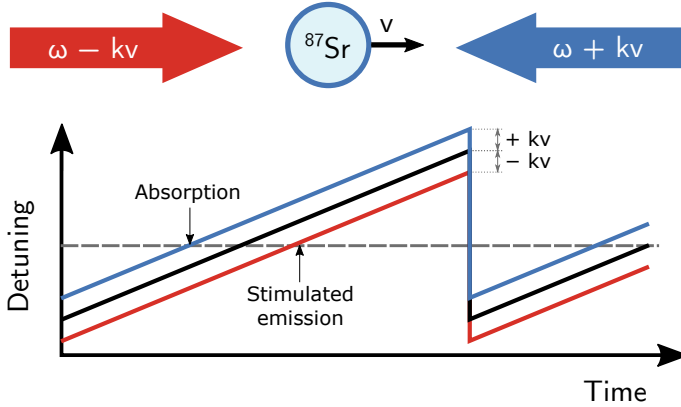
FIG. 3.3: SWAP working principle. The plain black trace describes the laser frequency sweep in the laboratory frame. In the reference frame of the atom, the detuning of each of the two counter-propagating beams (blue and red traces) is Doppler shifted by $\vec{k} \cdot \vec{v}$. This shift introduces an effective time ordering, ensuring that the momenta transferred to the atom are oriented against its direction of travel.

efficiency. Moreover, if the atom absorbs a second photon by adiabatic passage from the co-propagating beam, momentum will be imparted in the wrong direction. This second criterion is expressed by $\tau_e = |2(kv - 2\omega_r)/\alpha| \ll 1/\gamma$. Here v is the velocity of the atom, and k and $\omega_r = \hbar k^2/2m$ are the wavevector and the recoil frequency associated with the $^1S_0 - {}^3P_1$ transition, where $\hbar$ is the reduced Planck constant and m is the atom's mass. For high-velocity atoms, where $kv \gg 2\omega_r$, the second criterion requires the sweep rate α to be fast, while maintaining the first, adiabaticity criterion $\kappa \gg 1$.

Due to the presence of a magnetic field, the detuning range $\Delta\omega$ must be large enough to address all ^{87}Sr Zeeman sub-levels. However, the available laser power does not allow us to fulfill the adiabaticity criterion κ for a large range $\Delta\omega$. To mitigate this issue we use the $^1S_0$ F $= 9/2 - {}^3P_1$ F$' = 9/2$ transition, because it has the lowest differential magnetic moment of all the possible hyperfine transitions. Additionally, we further reduce the necessary $\Delta\omega$ by offsetting the center detuning of the sweep to the red of the unperturbed transition, see Fig. 3.2(b). Therefore, instead of using a symmetric detuning range, as shown in Fig. 3.3, we address more strongly the high-field seeking Zeeman sub-levels, see Fig. 3.2 (b). In this way we compromise between executing a well performing SWAP molasses for the most populated m_F states and addressing as many states as possible.

3.3.3   SWAP and inverted SWAP working regimes

For SWAP cooling, the sign of the sawtooth ramp slope determines whether the time ordering associated with absorption and stimulated emission results in net momentum
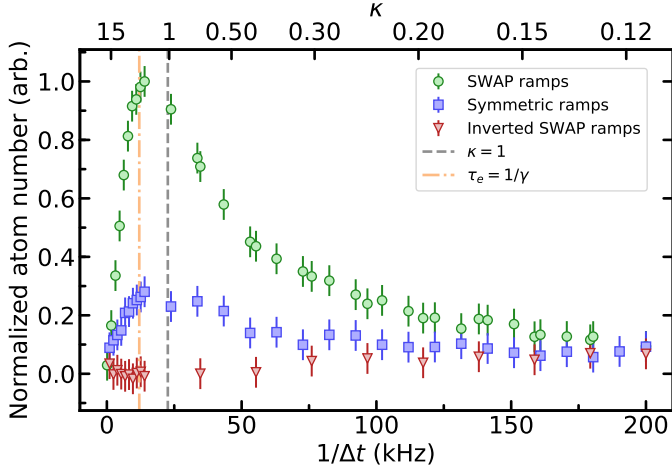
FIG. 3.4: Relative number of atoms captured in the narrow-line 3D MOT for three different ramp types with varying sweep frequency $1/\Delta t$ and fixed MOT loading time of 8.5 s. The green disks, blue squares, and red triangles show respectively SWAP, symmetric, and inverted SWAP ramps. The uncertainty on the data is estimated by performing 16 measurements at a value of $1/\Delta t = 14$ kHz using SWAP ramps, and we give the resulting standard deviation as error bars for all points. The gray dashed line and the orange dashed-dotted line show the conditions $\kappa = 1$ and $\tau_e = 1/\gamma$ ($v = 0.2\,\mathrm{m \cdot s^{-1}}$), respectively. We use the maximum available power for the 2D red molasses beams, which is 14.2 mW for one beam pair and 15.2 mW for the other. This corresponds to a Rabi frequency averaged across all transitions of about $2\pi \times 90$ kHz. The molasses light detuning is modulated as shown in Fig. 3.2, between $\Delta_1 = -2\pi \times 2\,\mathrm{MHz}$ and $\Delta_2 = +2\pi \times 0.2\,\mathrm{MHz}$ for SWAP and symmetric ramps and between $\Delta_1 = -2\pi \times 0.2\,\mathrm{MHz}$ and $\Delta_2 = -2\pi \times 2\,\mathrm{MHz}$ for inverted SWAP ramps. Note that the MOT atom number is not strictly proportional to the flux arriving in the lower chamber, due to possible optical pumping processes and other saturation effects (see Sec. 3.4).

gain or loss. A positive slope (SWAP ramps), such as the one shown in Fig. 3.3, results in deceleration and cooling, while a negative slope (inverted SWAP ramps) results in acceleration and heating [147, 166]. In Fig. 3.4 we compare the atom number loaded into the MOT (see Sec. 3.5) for molasses following SWAP, inverted SWAP, and symmetric ramps, with varying sweep frequency $1/\Delta t$. For all explored Δt, the flux of loaded atoms is the highest using SWAP ramps, while inverted SWAP ramps perform the worst. This difference is the most pronounced at $1/\Delta t_{\mathrm{opt}} \sim 15$ kHz, corresponding to an adiabaticity criterion of $\kappa \sim 1.5$, while in the limits of short or long sweep durations the fluxes become similar. This comparison of the three types of ramp shows that the time ordering of the molasses beams' action matters and that the adiabaticity of the emission and absorption of the rapid adiabatic passages plays a significant role here.

The results of Fig. 3.4 can be explained by considering the two SWAP criteria previously
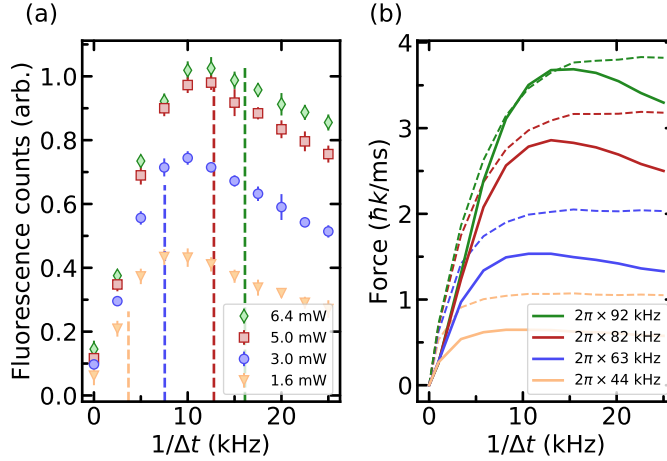
FIG. 3.5: Molasses performance characterization. (a) Experimentally mea-
sured transfer efficiency into the bottom chamber for several beam powers
with varying sweep frequency $1/\Delta t$. The powers stated in the legend refer
to the average laser power for each beam. Each data point represents the
average of ten independent measurements and the error bars show the stan-
dard deviation of these measurements. The vertical dashed lines highlight
the location of $\kappa = \Omega^2/\alpha = 1.5$. (b) Numerical estimations of the molasses'
average restoring force exerted on an atom exiting the 2D MOT, with the
same parameters as in (a). The curves represent thermal averages over a 1D
Maxwell Boltzmann distribution at 1 mK for two regimes, one integrated
only over the low-velocity class $|v| < 0.25\,\mathrm{m \cdot s^{-1}}$ (solid line) and the other
integrated over the high-velocity class $|v| > 0.25\,\mathrm{m \cdot s^{-1}}$ (dashed lines). The
given Rabi frequencies result from spatial averages of the intensity across a
$1/e^2$ beam waist.

given. Indeed, for short durations the adiabaticity parameter decreases to $\kappa \ll 1$ and
the probability of stimulated emission or absorption becomes negligible. This reduces
the cooling efficiency and effectively breaks the time ordering. In this limit the cooling
efficiencies of SWAP and inverted SWAP ramps converge and result in similar fluxes.
For $\kappa \gg 1$, corresponding to long durations, the adiabaticity criterion is fulfilled, but
the second criterion is broken, as $\tau_e \propto 1/|\alpha| \propto \Delta t$. For $\tau_e \gg 1/\gamma$ the cooling reduces to
two independent stimulated absorption events each followed by spontaneous emission,
one from the counter-propagating beam and one from the co-propagating beam. In this
situation the average slowing force approaches zero for all three ramp types.

3.3.4 Modeling SWAP molasses

To explore the power dependence of the 2D SWAP molasses, we measure the relative transfer efficiency to the lower chamber for different laser beam powers and sweep durations. These results are shown in Fig. 3.5(a).

We obtain this data by collecting fluorescence from the falling atoms in the lower chamber. For this purpose, we illuminate the passing atoms with light addressing the fast cycling $^1S_0 - {}^1P_1$ transition, with no other beam present in the lower chamber. This detection method provides a more direct measure of the atomic flux arriving into the lower chamber that what is given by the MOT atom number.

For each chosen power we observe the existence of an optimal sweep frequency close to $1/\Delta t_{opt} \sim 10\,\text{kHz}$, that shows only a small dependence with the laser beam power. The location of this optimum does not quite correspond to the value of the adiabaticity criterion κ, indicated in Fig. 3.5(a) by vertical dashed lines. This mismatch might arise from the laser beams' finite interaction time with the atoms. Indeed, in order to pass through the 8 mm-diameter baffle between the two vacuum chambers, the radial velocity must be reduced below $v < v_{\min} \approx 0.07\,\text{m} \cdot \text{s}^{-1}$. However, atoms exiting the 2D MOT have a radial velocity up to $0.5\,\text{m} \cdot \text{s}^{-1}$. Successful passage to the lower chamber therefore requires that the 2D molasses removes about 50 recoil momenta per beam pair. Assuming a momentum transfer of one photon recoil per sweep, achieving this deceleration within the finite interaction time with the laser beams would require a minimum sweep frequency of $1/\Delta t \sim 3\,\text{kHz}$. The measured optimum sweep frequency is three times slower, indicating that on average only 0.3 photons might be transferred per sweep, corresponding to a restoring force of $\sim 3\,\hbar k/\text{ms}$.

To deepen our insight into SWAP molasses cooling, we theoretically estimate the average restoring force exerted on the atoms exiting the 2D MOT, see Fig. 3.5(b). We limit our discussion to the average force exerted by the molasses, as reproducing the data shown in Fig 3.5(a) would require introducing free parameters into our model that we do not have access to. Such parameters include the atomic distribution exiting the 2D MOT, the transit time and the maximum transfer velocity of the atoms. Moreover, including them in the model would not provide deeper insight into the molasses cooling process itself.

The results of Fig. 3.5(b) are obtained by expanding on the theory developed by Bartolotta et al. [147] to take into account the internal structure of ^{87}Sr. In particular, we numerically integrate the optical Bloch equations for the sweep durations and Rabi frequencies shown in Fig. 3.5(b) using the finite set of states,

$$|m_\text{F}, p + n\hbar k\rangle, |m_{\text{F}'}, p + n\hbar k\rangle,$$

where $n \in \{2, 1, 0, -1, -2\}$, p defines the starting momentum used in the calculation, and we have used short-hand notation for a particle with momentum $p + n\hbar k$ in the $^1S_0$ F = 9/2 m_F and $^3P_1$ F' = 9/2 $m_{F'}$ states respectively.

We solve these equations stepping through several starting momenta, $p/\hbar k \in \{70, 69.5, 69, \ldots, 0\}$ and one sweep cycle of duration Δt to obtain a momentum dependent force $F(p) = (\text{tr}(\rho_{i,p}\hat{p}) - \text{tr}(\rho_{f,p}\hat{p}))/\Delta t$. Here $\hat{p}$ is the atomic momentum operator, $\rho_{i,p} = \sum_{m_F} P_{i,m_F,p} |m_F, p\rangle \langle m_F, p|$ is the initial state used in the calculation and $\rho_{f,p}$ is the final state after the single sweep.

To take into account optical pumping, the initial distribution over internal states m_F described by $P_{i,m_F,p}$ in ρ_i is obtained by an iterative process. Starting from a fully depolarized state with momentum $70\hbar k$, i.e. $P_{i,m_F,70\hbar k} = 1/10$, the final occupation of the internal states of each momentum step is used as an input occupation for the following step, i.e. $P_{i,m_F,p'} = \sum_n \langle m_F, p + n\hbar k | \rho_{f,p} | m_F, p + n\hbar k \rangle$, with $p - p' = 0.5\hbar k$ corresponding to our choice of discretization. We checked that the result of the calculation depends weakly on this somewhat arbitrary choice and that the shape of the curves shown in Fig. 3.5 (b) remains similar when using a grid with $p - p' = \{0.5, 1, 2\}\hbar k$.

The curves shown in Fig. 3.5(b) average the force obtained over a 1D Maxwell-Boltzmann distribution split into two velocity classes, $|v| < v_c$ and $|v| > v_c$. Atoms in the low-velocity class are rapidly deexcited via stimulated emission, whereas atoms in the high-velocity class remain unaddressed long enough to spontaneously emit a photon. Here we choose to distinguish these two classes for $1/\Delta t = 15$ kHz, which gives $v_c = 0.25$ m · s^{-1} using the second SWAP cooling criterion, see Sec. 3.3.2.

Our theoretical results confirm that for the high-velocity atoms, $v > v_c$, the cooling mostly reduces to a single absorption by adiabatic passage from the counter-propagating beam, followed by spontaneous emission. Low velocity atoms $v < v_c$ have an effective detuning dominated by the Zeeman shifts. Since our sweep range is red detuned from the unperturbed transition, it leaves the magnetic sub-levels with $m_F > \frac{3}{2}$ unaddressed. However, our simulations show that optical pumping is optimal for a sweep duration corresponding to ~ 10 kHz. This optical pumping enhances the population of the states that are efficiently addressed by the molasses beams, particularly those with low $|m_F|$ values. Failing to take the effect of optical pumping into account shifts the optima shown in Fig. 3.5(b) to significantly lower sweep duration.

From these simulations we obtain the maximum average restoring force $F_{\text{max}} = 3.8\,\hbar k/\text{ms}$ provided by the SWAP molasses. This relatively small force is enough to collimate most atoms such that they pass through the 8 mm-diameter hole between chambers, and is consistent with the rough estimation $\sim 3\,\hbar k/\text{ms}$ we gave previously.

To finalize this section, we summarize the SWAP molasses cooling parameters used in the remainder of this work. The optical powers are 14.2 mW for one pair of beams and 15.2 mW for the other. Their polarization is linear and perpendicular to the y axis. The sweep duration is $\Delta t = 71\,\mu s$, while the molasses detuning is modulated between $\Delta_1 = -2\pi \times 2\,\text{MHz}$ and $\Delta_2 = +2\pi \times 0.2\,\text{MHz}$. Based on our experimental explorations, we find this set of parameters to provide optimal flux to our narrow-line 3D MOT.

3.4 Laser slowing stage

Atoms flowing through the 2D SWAP molasses region can be captured in the lower chamber by a narrow-line MOT operating on the $^1\text{S}_0 - {}^3\text{P}_1$ transition, see Fig. 3.1. Because of the limited deceleration achievable with the $^1\text{S}_0 - {}^3\text{P}_1$ transition, we slow the atoms before they reach the MOT. In the following, we first describe the operation of this slowing stage for bosonic isotopes. Then we highlight the additional challenges for the fermionic isotope. We finish this section by describing the frequency ramps used to efficiently slow the atoms.

Accelerated by gravity, atoms reach the entrance of the lower chamber with a downward velocity distribution peaked at $\sim 4\,\text{m}\cdot\text{s}^{-1}$, which exceeds the MOT's capture velocity. Therefore we employ a counter-propagating laser beam addressing the $^1\text{S}_0 - {}^3\text{P}_1$ transition to begin slowing the atoms before they reach the MOT, which is located $\sim 40\,\text{cm}$ below the 2D SWAP molasses. This beam is circularly polarized to address the σ^+ transition and its frequency is red detuned from the unshifted resonance. For the laser slowing stage, the magnetic field is dominated by the quadrupole field used to generate the narrow-line MOT.

For bosonic strontium, the slowing stage operates as a Zeeman slower and its working principle is sketched in Fig. 3.6(a). As atoms decelerate, the change in Doppler shift δ_{Doppler} is partially compensated, thanks to the vertical magnetic field gradient produced by the MOT, $dB/dy = 0.32\,\text{G}\cdot\text{cm}^{-1}$. This gradient is mostly linear up to 10 cm away from the MOT quadrupole center, beyond which the magnetic field amplitude decreases. Due to the high initial atom velocity the Zeeman shift alone is insufficient to fully address the atoms, so we also modulate the laser detuning with a span of $\Delta\omega_{\text{ZS}} = 2\pi \times 4.05\,\text{MHz}$, thus forming a "white light" slower [169].

The choice of laser detuning Δ_2, together with the maximum magnetic field experienced by the falling atoms B_{max}, defines a capture velocity for the slowing stage, $v_{\text{capture}} = (\delta_Z(B_{\text{max}}) - \Delta_2)/k$, see Fig. 3.6. For bosonic strontium $v_{\text{capture}} = 5.3\,\text{m}\cdot\text{s}^{-1}$, faster than the velocity at which the atoms fall of $\sim 4\,\text{m}\cdot\text{s}^{-1}$. For fermionic strontium, the hyperfine structure complicates the slowing stage, see Fig. 3.6(b). From all the hyperfine transitions (see Fig. 3.2) only the $^1\text{S}_0\ F = 9/2 - {}^3\text{P}_1\ F' = 11/2$ "cooling" transition can have high enough capture velocity to slow the atoms while being compatible with the MOT configuration
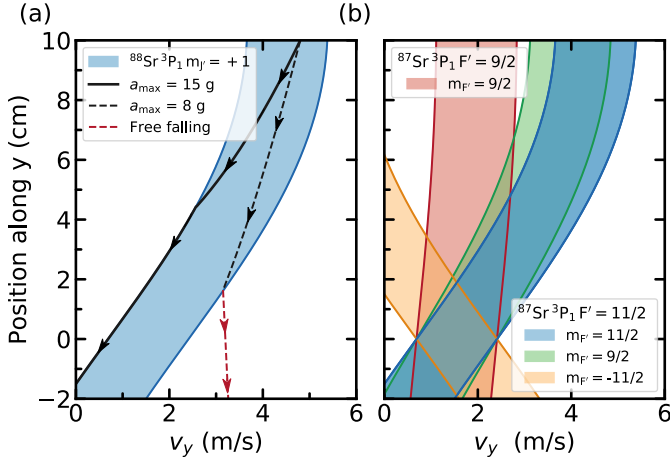
FIG. 3.6: Phase-space plots of falling atoms under the influence of the slower beam. The highlighted regions show the resonance windows of the various $^1S_0 - {}^3P_1$ transitions, defined by $\Delta_2 < \delta_Z(B(y)) - \delta_D(v_y) < \Delta_1$. Here $\delta_D(v_y)$ is the Doppler shift, $\delta_Z(B(y))$ the position-dependent Zeeman shift resulting from the quadrupole field of the MOT, and Δ_1 and Δ_2 are the slower laser start and stop frequency detunings given in Table 3.1 (YMOT). The lines show falling trajectories for two different decelerations. Atoms not efficiently slowed (dashed lines) can fall out of the resonance window and be lost. (a) For bosonic isotopes, such as ^{88}Sr, as the falling atoms slow down (black solid line), the change of Doppler shift is partially compensated thanks to the magnetic field gradient from the quadrupole, whose center is at $y = 0$. (b) For fermionic ^{87}Sr, due to its internal structure, the capture velocity depends on the hyperfine transition being addressed. In particular, the cooling transition has the highest possible capture velocity, while the pumping transition has a much smaller capture velocity due to the smaller Landé factor. For clarity, not all of the possible transitions are shown.

described in Sec. 3.5. Therefore we use this transition in order to slow atoms entering the lower chamber. Note that the condition $v_{\text{capture}} > 4\,\text{m} \cdot \text{s}^{-1}$ can only be fulfilled for atoms in the $m_F > \frac{3}{2}$ states, were $\vec{y}$ defines the quantization axis. Without optical pumping, fast atoms entering the lower chamber in other states will be lost. This loss mechanism can be particularly relevant as our simulations show that the collimating 2D molasses in the upper chamber results in a mixture of several m_F states, predominantly with low $|m_F|$ values.

To optically pump ground-state atoms to the $m_F > 3/2$ Zeeman sub-levels, we use dual-frequency laser light for the vertical slower beam, addressing two different hyperfine manifolds. Firstly, we use the cooling transition, because of its high capture velocity. Secondly, we use the $^1S_0\ F = 9/2 - {}^3P_1\ F' = 9/2$ "pumping" transition to optically pump atoms that would otherwise remain unaddressed. For atoms entering the lower chamber, the slower light is typically off-resonant by a few MHz. However, atoms are illuminated by the vertical beam for $\sim 10\,\text{cm}$ traveling distance before reaching the region where the

slowing starts. For velocities of $2 - 4\,\text{m}\cdot\text{s}^{-1}$, the resulting interaction times of $50 - 25\,\text{ms}$ allow for off-resonant scattering of about $1 - 100$ photons, thus optically pumping atoms to addressed states, see Table 3.1 and Fig. 3.1.

As atoms continue to slow down, the σ^+ polarized slower beam keeps the atoms in the $m_{\text{F}} = 9/2$ magnetic sub-level. However, atoms traveling toward the MOT location can experience spin flips relative to the quantization axis $\vec{y}$ if they are able to adiabatically follow the local magnetic field. For these atoms the deceleration provided by the cooling transition will be severely reduced.

Indeed, such a spin flip is possible. Close to the quadrupole center slowed atoms have a velocity $v_y \gtrsim 0.5\,\text{m}\cdot\text{s}^{-1}$. These falling atoms will experience a time-dependent magnetic field that rapidly changes direction. If the rate of magnetic field change is slower than the Larmor frequency of the $^1\text{S}_0\,\text{F} = 9/2$ state then the probability of a spin flip is high. This criterion can be expressed as $\chi = \frac{1}{B}\frac{dB}{dt}/\gamma_I B \ll 1$, where $\gamma_I = 2\pi \times 183(7)\,\text{Hz}\cdot\text{G}^{-1}$ is the gyromagnetic ratio of the $^1\text{S}_0\,\text{F} = 9/2$ state.

The criterion $\chi = 1$ delimits a horizontal disk with radius $r \approx \sqrt{v_y/(\gamma_I\,dB/dy)} \approx 4\,\text{mm}$. This radius is comparable to the atomic beam radius, apertured by the $8\,\text{mm}$-diameter baffle between chambers. Therefore some atoms will fall outside the disk and their spin will adiabatically follow the local magnetic field. Relative to the quantization axis these atoms will experience a spin flip and the deceleration imparted by the cooling transition will be reduced. For example atoms transferring to the $m_{\text{F}} = -9/2$ Zeeman sub-level will experience a maximum deceleration of only $3\,\text{m}\cdot\text{s}^{-2}$, because of the reduced Clebsch-Gordan coefficients. Without optical pumping these atoms will be lost. Luckily, the σ^+ pumping transition is an order of magnitude stronger, ensuring fast optical pumping of these atoms to the efficiently-slowed $m_{\text{F}} = 9/2$ state.

As described above, optical pumping is important for the operation of the slower. We enhance it by using the dual frequency configuration for the slower beam, thereby improving the loading efficiency by a factor $2.2(3)$ compared to when addressing only the cooling transition. Note that only using the pumping transition does not enable us to load any atoms in the MOT.

As atoms fall in the lower chamber they can fall out of resonance and be lost if they are not efficiently slowed, see Fig. 3.6(a) black dashed line. To increase the available force, we ramp the detuning of both transitions addressed by the slower beam using an asymmetric sawtooth, as in Fig. 3.3. Operating the slower beam in this manner can yield a force up to twice the typical radiation pressure force [165]. Here, because atoms are always counter-propagating toward a single beam, ramps with positive or negative slope yield the same flux. Using an asymmetric sawtooth frequency sweep instead of a symmetric one serves only to suppress stimulated emission into the slower beam. Using the asymmetric

TABLE 3.1: Properties of the MOT beams shown in Fig. 3.1. For each beam, we give the power of the cooling || pumping beam, $1/e^2$ beam diameter D, and laser detuning sweep parameters: start detuning Δ_1, stop detuning Δ_2, and repetition rate $1/\Delta t$. Cooling and pumping beams have the same polarization, the same frequency modulation, and are combined within the same optical fibers before being sent to the atoms. The vertical MOT beam is focused ~ 22 cm above the quadrupole center and we give the diameter of the beam ~ 22 cm below it. The high-power for the vertical beam is required to achieve high-flux in the experiment, while the remaining parameters offer more flexibility and have been tuned to maximize the flux in the experiment.

Beam	Power (mW)	D (mm)	$\Delta_1/2\pi; \Delta_2/2\pi$ (MHz)	$1/\Delta t$ (kHz)
YMOT	9.2 || 6.6	68	$-0.94; -3.49$	40
XMOT1	0.66 || 0.3	47	$-0.65; -2.19$	15
XMOT2	0.66 || 0.3	47	$-0.65; -2.19$	15
ZMOT1	0.1 || 0	8	$-0.82; -1.24$	17
ZMOT2	0.1 || 0	8	$-0.82; -1.24$	17

frequency sweep we enhanced our loading efficiency by a factor of ~ 1.5 compare to using only the symmetric sweeps. Here the sweep time has been independently optimized for each sweep configuration and we have used the laser detunings and powers shown in Table 3.1 (YMOT beam).

3.5   Steady-state narrow-line MOT

Atoms that are successfully slowed accumulate in a narrow-line 3D MOT operating on the $^1S_0 - {}^3P_1$ transition. In this section we describe how this MOT is set up and characterize its performance. In particular, we will focus on the comparison of the flux and lifetime between MOTs of ^{88}Sr (bosonic strontium) and ^{87}Sr (fermionic strontium).

The MOT confinement is provided by five beams, four in the horizontal plane and one propagating upward. The downward restoring force is provided by gravity. The upward propagating beam is also used as a slower beam, see Sec. 3.4. The properties of these beams are given in Table 3.1, while the field gradients used for the MOT are $\{-0.55, 0.32, 0.23\}\, \text{G} \cdot \text{cm}^{-1}$ along the $\{x, y, z\}$ axes. The magnetic field gradient is produced by three different coil pairs in anti-Helmholtz configuration. The choice of using three different coil pairs to generate the magnetic gradient is taken for experimental convenience. Indeed, a single coil pair oriented along the x, y or z axes could also be used.

In order to characterize the performance of this MOT, we measure the flux, temperature, steady-state atom number, and lifetime. We then compare the MOT for fermionic strontium

with one for bosons produced with the same apparatus. The results are summarized in Table 3.2. In order to characterize the MOT we take absorption images using the $^1S_0 - {}^1P_1$ transition, see inset of Fig. 3.7.

To record the loading of the MOT, we repeat such measurements for different loading times after switching the laser beams on, see Fig. 3.7(a). As the flux of atoms entering the lower chamber is constant, we fit these data with the function $N(t) = N_\infty(1 - e^{-t/\tau_{\text{load}}})$, where N_∞ is the steady-state atom number, and τ_{load} is the $1/e$ loading time. We obtain from the fit $\tau_{\text{load}} = 6.4(1)\,\text{s}$ and $N_\infty = 8.41(4) \times 10^7$ atoms. We extract the flux of atoms Φ being loaded into the MOT as $\Phi = N_\infty/\tau_{\text{load}} = 1.31(2) \times 10^7$ atoms/s. We also measure the $1/e$ lifetime by reaching steady state then turning off the 2D MOT in the upper chamber, see Fig. 3.7 (b).

To quantify the long-term robustness of our experiment each of the data-points shown in Fig. 3.7 (b) (blue disks) is measured four times at ~ 45 minute intervals. For the data point at 0.1 s, we measure a relative atom number fluctuation of 2.1% across the three hour time span. The measured long-term stability is mostly limited by laser power and frequency fluctuations, specifically of the lasers addressing the 30 MHz wide $^1S_0 - {}^1P_1$ transition. These limitations could straightforwardly be overcome by better laser locking schemes and active power stabilization of these lasers.

We measure the temperature of the steady-state MOT by time of flight and obtain $7.5(2)\,\mu\text{K}$ along the y axis and $14.2(2)\,\mu\text{K}$ along the z axis. As we use a single-axis imaging system, we are unable to measure the sample's size and temperature in the x axis, and we assume it to be the same as in the other horizontal (z axis) in order to calculate the average MOT temperature and peak density. However it must be noted that, because we tune the laser powers and frequencies independently for each axis, this approximation is rough.

We compare these data to an equivalent ^{88}Sr bosonic MOT, using similar sweep parameters and magnetic fields. For ^{88}Sr the collimating 2D molasses in the upper chamber uses the same detuning ramps and similar powers as the ones reported in our previous work [35]. We follow the procedure described above to characterize this MOT and summarize the results in Table 3.2. For bosons, the flux is $2.29(6) \times 10^8$ atoms/s, about 17 times higher than for fermions. This difference can partly be explained by the 12 times higher natural abundance of ^{88}Sr compared to ^{87}Sr [170]. The remaining difference can be explained by the previously mentioned imperfections of the 2D molasses and Zeeman slower, owing to the more complex internal structure of ^{87}Sr.

The similar lifetimes of ^{88}Sr and ^{87}Sr MOTs indicates that the two MOTs have similar losses. A well-known peculiarity of ^{87}Sr narrow-line MOTs is that they have a loss mechanism not present in narrow-line bosonic MOTs, if no countermeasures are taken. This loss mechanism arises due to the difference in Landé factors between the $^1S_0$ F = 9/2

TABLE 3.2: Characteristics of the steady-state MOT, for both ^{87}Sr and ^{88}Sr isotopes (see also description in the main text). The steady-state MOT extents $\sigma_{y,z}$ are Gaussian widths extracted by fitting a 2D Gaussian function to the images of the MOT. All uncertainties are given as the standard deviation from the fitted data.

	^{87}Sr MOT	^{88}Sr MOT
Flux Φ (atoms/s)	$1.31(2) \times 10^7$	$2.29(6) \times 10^8$
T_z (µK)	14.2(2)	12.6(1)
T_y (µK)	7.5(2)	9(1)
$T_{average}$ (µK)	12.0(1)	11.4(4)
Width σ_y (mm)	0.689(8)	0.632(8)
Width σ_z (mm)	1.91(2)	2.82(2)
Atom number N_∞	$8.41(4) \times 10^7$	$100.8(9) \times 10^7$
Peak density (atoms/cm^3)	$2.12(4) \times 10^9$	$1.28(2) \times 10^{10}$
$1/e$ loading time τ_{load} (s)	6.4(1)	4.4(1)
$1/e$ lifetime τ_{life} (s)	4.84(3)	4.6(1)

ground state and the ^{3}P$_1$ F$' = 11/2$ excited state. Indeed, atoms within such MOTs can be optically pumped into states that are not trapped if they travel to the opposite side of the quadrupole magnetic field center. Typically these losses are avoided by adding a second set of laser beams addressing the pumping transition. This transition generates "stirring", a fast randomization of the population over all the m_F states [171]. We apply this solution by using the pumping light described in Sec. 3.4 with the parameters reported in Table 3.1. Fig. 3.7(b) compares the MOT's decay with and without pumping beams. Surprisingly, we found that the presence of the pumping light does not affect the ^{87}Sr MOT lifetime. While the flux increases by a factor of 2.2(3) the lifetime remains the same.

This behavior can be explained by the small gradients of the MOT quadrupole field and large detuning of the MOT beams, combined with the sample's low temperature. Atoms slowed by the vertical beam and captured in the MOT are addressed at a distance $y_0 = \hbar\Delta_1/(g_{F'}m_{F'}\mu_B\,dB/dy)$ from the MOT quadrupole magnetic field center, where μ_B is the Bohr magneton. For $m_F = +9/2$, $|y_0| \approx 14$ mm below the center, which is much bigger than the vertical Gaussian width σ_y of the MOT sample. This large distance relative to the MOT size implies that atoms always lie well below the quadrupole field center. Here they are constantly addressed by the vertical beam and optically pumped mainly into the $m_F = +9/2$ state. Therefore the losses observed in other ^{87}Sr MOTs that are operated with less detuning and without stirring beam, are not present here. The convenient polarization mechanism at play here, resulting from weak optical forces, gravity and the large detuning of the MOT beams, has already been observed in MOTs of other elements
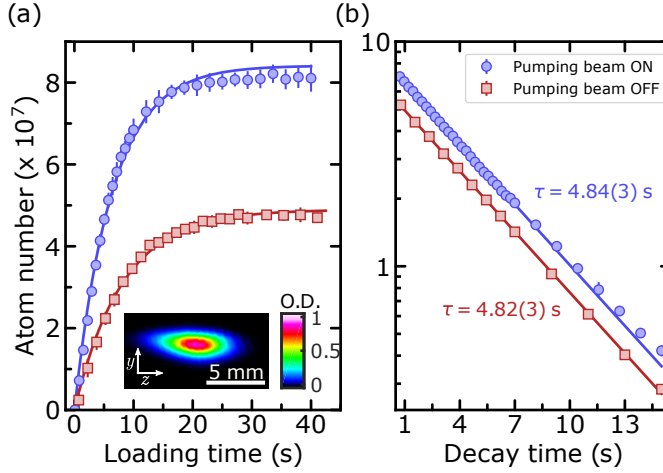
FIG. 3.7: ^{87}Sr MOT loading (a) and decay (b) with the pumping beams on and off. The solid lines are fits to the data using the functions (a) $N(t) = N_\infty(1 - e^{-t/\tau_{load}})$ and (b) $N(t) = N_0 e^{-t/\tau_{life}}$. When switching the pumping beams on, the flux into the MOT is enhanced by 2.2(3) while the lifetime remains the same. In (a) at $t = 0$ we switch the laser beams on. In (b), we load the MOT for 15 s, then switch off the 2D MOT in the top chamber at $t = 0$. Error bars give the standard deviation from averaging $2 - 5$ data points. The inset in (a) shows a typical absorption image of the steady-state MOT, for 40 s loading time in presence of the pumping beam.

such as dysprosium and erbium [38, 172, 173]. We note that, even if present, the pumping light is unlikely to have a strong effect on the MOT because it is strongly detuned at its location, see Fig. 3.6. The role of the pumping light is to increase the atom flux Φ from the slower stage.

3.6 Discussion and conclusion

Let us now compare the performance of our ^{87}Sr MOT with the requirements for a superradiant active optical clock operating on the mHz-wide clock transition [81, 154, 155]. Such a clock is a bad-cavity laser, which uses as a gain medium a cloud of ultracold atoms within the mode of a high-finesse optical cavity. After being optically pumped to an excited state, these atoms can emit into the cavity mode, with a rate of emission enhanced via collective, superradiant emission. To sustain the emission of this laser, the excited population must be renewed. Atoms could be renewed by pumping them back into the excited state, which leads to unfavorable heating, or by bringing new excited state atoms into the superradiantly lasing ensemble. This translates into requirements for a stream of new incoming atoms needed for allowing the laser's continuous-wave operation. For a laser operating on the

$^1S_0 - {}^3P_0$ transition of strontium, we estimate that, without optical pumping, the flux of new atoms must be superior to 10^6 ^{87}Sr atoms/s. Moreover, MOT atoms must be transported into the cavity mode, located somewhere outside of the MOT region, where they cannot be addressed by laser cooling light. Such transport could be achieved by a moving optical lattice [85]. For MOT atoms to be efficiently loaded into a lattice of reasonable depth, their temperature should be lower than $\sim 10\,\mu$K. Our steady-state fermionic MOT satisfies these requirements and is an excellent candidate for feeding atoms into a superradiant laser system. A lower temperature or higher density can be achieved by using less light intensity within MOT beams, to the detriment of the atomic flux. A higher flux can be straightforwardly achieved by operating at a higher oven temperature and/or by using "repumper" beams to plug losses on the $^1S_0 - {}^1P_1$ cooling cycle [87].

To conclude, we have demonstrated a steady-state magneto-optical trap operating on the narrow intercombination line of strontium that works with the fermionic isotope ^{87}Sr, despite the additional challenges arising from its hyperfine structure. Two key ingredients were necessary: (1) the use of 2D SWAP molasses to collimate the atomic beam before atoms pass from the upper vacuum chamber to the next; (2) a dual-frequency narrow-line Zeeman slower and MOT capable of slowing and capturing the incoming atoms. This MOT is well suited to provide atoms for the gain medium of a continuous-wave superradiant laser operating on strontium's mHz-wide clock transition.

Acknowledgments

Addenda

In the following sections we present additional information not included in reference [90].

A   Two-dimensional SWAP molasses

In section 3.3 we described a new type of laser cooling technique known as sawtooth wave adiabatic passage (SWAP) cooling [162]. We use this technique to transfer the atoms between two chambers and achieve high atomic flux into the MOT (see subsection 3.2). Although our molasses operates in two dimensions, we described it in a single dimension, as a such description can give a good understanding of the cooling dynamics. However, when cooling atoms in two or three dimensions, SWAP cooling is known to reduce its efficiency. This reduction results from photon exchange between each of the laser cooling axes [165].

Here we attempt to suppress this photon exchange by dephasing the SWAP ramps of each of the orthogonal beam pairs. We start with a brief description of SWAP cooling in one dimension. Then we use an intuitive explanation to illustrate how cross-axis photon exchange can reduce the cooling efficiency and how introducing a dephasing might affect the cooling. Finally we experimentally investigate the effect of such dephasing in our 2D SWAP molasses cooling efficiency.
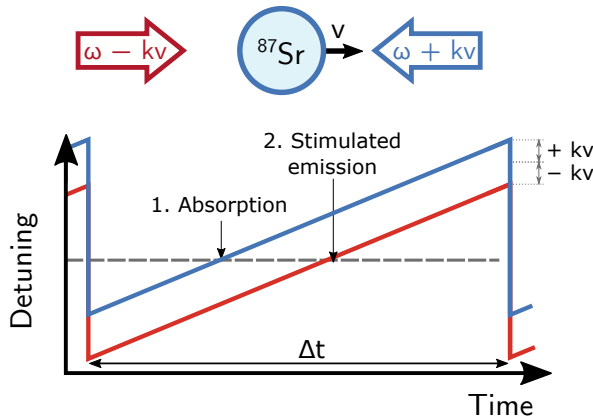

FIG. 3.8: SWAP molasses cooling in one dimension. The atom is addressed by two counter-propagating beams with the same polarization. The detuning of these lasers is periodically ramped in a sawtooth-shaped manner with a sweep time of Δt. Due to the Doppler effect and the ramp choice, the atom is addressed first by the counterpropagating laser and then by the co-propagating laser reducing its velocity.
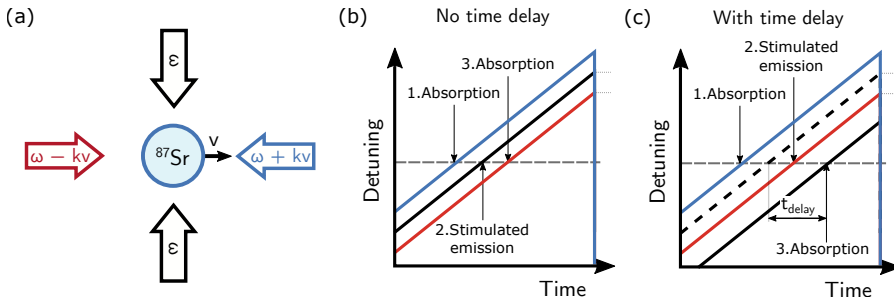
FIG. 3.9: SWAP molasses cooling in two dimensions. (a) The figure illustrates the case when the atom travels perpendicular to a beam pair. (b) In this case the atom is addressed first by the counter-propagating laser beam, and then by one of the perpendicular laser beams, reducing the cooling efficiency and leading to heating. (c) By introducing a time delay (t_{delay}) between booth cooling arms the resonance time of the perpendicular beams can be shifted, suppressing the undesired stimulated emission into the perpendicular beams.

The SWAP cooling principle in one dimension is shown in figure 3.8. To briefly recapitulate, SWAP cooling relies on two counter-propagating beams with the same polarization to adiabatically transfer the atoms between two different states, thus reducing its velocity. First an atom is transferred to an excited state, absorbing a photon from the counter-propagating beam. Then the atom is adiabatically transferred back to the ground state, this time by the co-propagating beam emitting a photon. In this a way the momentum of the atom is reduced by two-photon recoils. SWAP cooling relies on the Doppler effect and on sawtooth-shaped detuning ramps of the laser cooling light to ensure that the time ordering between the absorption and stimulated emission events results in the slowing of the atom. SWAP cooling has the advantage of robustly addressing atoms with different detunings while simultaneously increasing the cooling force.

Unfortunately, the working principle of SWAP cooling can be unfavorably altered when executed in two dimensions. Figure 3.9 shows the situation when the atom propagates along one beam axis and perpendicular to the other. In this particular case the atom will be adiabatically transferred to the excited state by the counterpropagating laser beam, reducing its momentum by one-photon recoil. Then the atom will be adiabatically transferred to the ground state by one of the perpendicular beams, emitting one photon into it and increasing its velocity on the perpendicular axis. Finally, the atom will absorb a photon from the copropagating beam increasing its velocity. These three events will lead to heating. To suppress this effect a dephasing between the swap ramps of each beam pair can be introduced. In our experiment this dephasing is done by introducing a time delay (t_{delay}) between the programmed start time of each SWAP ramp. This dephasing shifts the
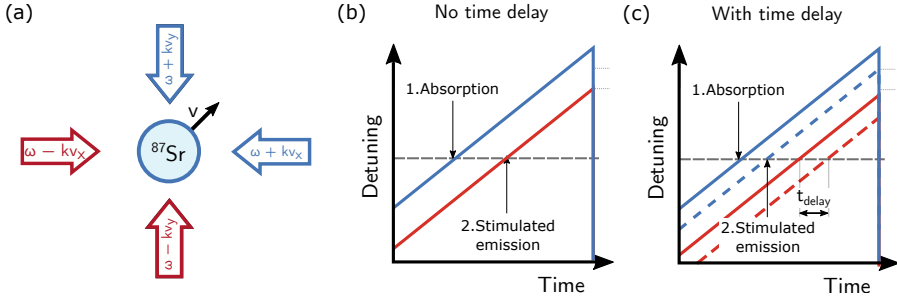
FIG. 3.10: SWAP molasses cooling in two dimensions. (a) The figure illustrates the case when the atom travels at a 45° angle. Each pair of counterpropagating and copropagating lasers have the same Doppler shift. (b) In this case the time ordering between the stimulated absorption and emission events is favorable. (c) Introducing a time delay can lead to heating if it is smaller than the lifetime of the transition.

resonance time for one of the orthogonal laser pairs (see figure 3.9 (c)), and can suppress cross-axis photon exchange.

Unfortunately, such a time delay can also lead to heating. Figure 3.10 describes the situation when an atom is traveling at a 45° angle to the laser cooling beams. In this case each of the counterpropagating and copropagating beams have the same Doppler shift, $+\vec{k}\vec{v}$ and $-\vec{k}\vec{v}$ respectively. If the introduced time delay is smaller than the lifetime of the excited state, the atom will absorb and emit a photon into the counterpropagating beams first and then into the copropagating beams, reducing the cooling efficiency.

To explore the effect that introducing a time delay might have on the 2D SWAP molasses cooling efficiency, we measure the atoms captured in the narrow-line MOT (see subsection 3.5) with varying delay times for different sweep frequencies $1/\Delta t$. The data is shown in figure 3.11. At a sweep frequency of 10 kHz (figure 3.11 (a)), two distinct peaks can be observed. Initially at short delay times, such that $t_{\text{delay}} < 1/\Gamma$ (vertical dashed line), the SWAP cooling efficiency reduces. Here photons are transferred first between the two counter-propagating beams, and finally between the two copropagating beams, as shown in figure 3.10, reducing the cooling efficiency. At longer time delays this effect is suppressed and the original cooling efficiency is recovered. At higher sweep frequencies (figure 3.11 (b)) the second peak is no longer observed. Indeed, here the condition $t_{\text{delay}} > 1/\Gamma$ (blue vertical dashed line) cannot be fulfilled within one SWAP period.

To explore the dependence of the zero-time-delay peak's shape, we measure its width for different modulation frequencies, see figure 3.12. For sweep frequencies higher than 10 kHz the width of the peak stays constant within experimental uncertainty. For the data point at 10 kHz, we have removed the points corresponding to the second peak (see figure 3.11), which introduces a systematic error on the fit. This result further confirms the previous
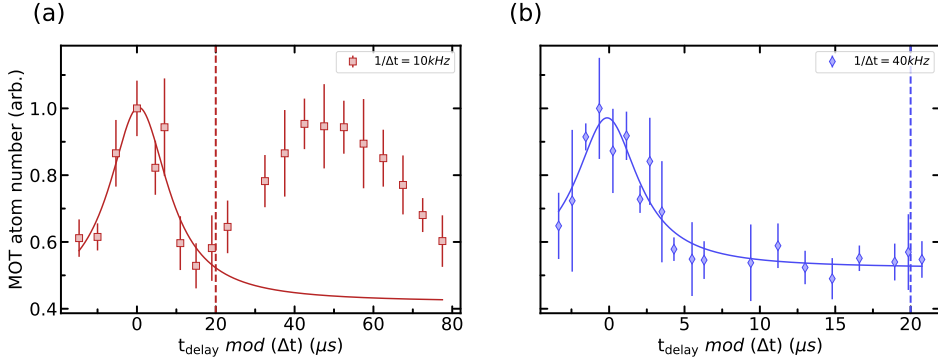
(a)

(b)

FIG. 3.11: Mot loading efficiency for different SWAP time delays t_{delay}. (a) For a sweep time of $\Delta t = 100\,\mu s$ and (b) for a sweep time of $\Delta t = 25\,\mu s$. Here the data is plotted modulo the sweep time ($t_{\text{delay}}\text{mod}\Delta t$). Each plot shows an average across two (a) and four (b) periods. Each data-point is averaged 2-8 times and error-bars show the corresponding standard deviation. The vertical dashed lines highlight the condition $t_{\text{delay}} = 1/\Gamma = 21\,\mu s$, where Γ is the natural linewidth of the $^1S_0 - {}^3P_1$ transition.

condition ($t_{\text{delay}} < 1/\Gamma$), which did not depend on the modulation frequency.

Unfortunately, the height of all observed peaks in figure 3.11 (a) remains similar, indicating that the cooling is not improved by introducing such time delay. We might not observe further enhancement because our molasses operates in a high-velocity regime where the additional heating induced by cross-axis photon exchange might be negligible.[2] In experiments that operate in a lower velocity regime than we do, introducing such time delay might result in increased cooling efficiency and lower temperatures.

B   Steady-state MOT simulation

To independently confirm some of the results presented in reference [90] we develop a Monte-Carlo simulation of the MOT. Our simulation has no free parameters. It uses the laser parameters described in reference [90] and a linear approximation for the magnetic field corresponding to the quadrupole gradient of the MOT. In this section, we describe the main results of this simulation. For the interested reader a simplified description of it can be found at the end of this section. Additionally we have also made the code publicly available [174].

We begin by benchmarking our simulation comparing its results to the available experimental data. In table 3.3 we give the predicted MOT's temperature and width from

---

[2]The mean average radial velocity of the incoming atoms to the molasses region is $\lesssim 0.5\,\text{m}\cdot\text{s}^{-1}$ and the required transfer velocity is $0.1\,\text{m}\cdot\text{s}^{-1}$. Both velocities are much larger than the recoil velocity of the transition of $0.07\,\text{m}\cdot\text{s}^{-1}$
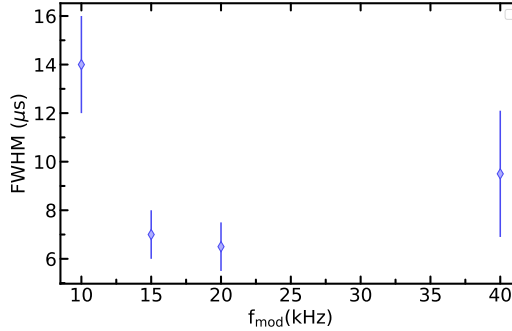
FIG. 3.12: Full-width-half-maximum of the zero-phase-peak (see figure 3.11) at different sweep frequencies ($1/\Delta t$). Each data point corresponds to a Lorentzian fit with a background to the data shown in figure 3.11.

our simulation and compare them with the experimental values given in subsection 3.5. While both the predicted temperature and cloud size are similar to the experimental values, the difference is larger than the uncertainties. Our simulation assumes that the horizontal laser beams are well aligned with the MOT cloud. Unfortunately, the predictions are quite sensitive to the location of the MOT cloud with respect to the lasers. For example, by introducing an offset on the z-MOT beam of 4 mm (half the beam waist) in the vertical direction, the predicted size and temperature on this axis increase to 6.6 mm and 41 μK respectively. So the difference between our prediction and the experimental data likely arises from the large uncertainty in the location of the beams. Here we chose to not introduce any free parameters in our simulation and use the previous assumption that the MOT cloud is well centered with the laser-cooling beams.

Our simulation predicts a surprisingly high temperature on the *x*-axis. Unfortunately, in our experiment we use a single axis imaging system, so we were unable to optimize the cloud's density and temperature on this axis. Our simulation shows that this value could easily be improved by increasing the power of the laser beam on this axis. For example, a power increase by a factor of two for the x MOT beam reduces the predicted temperature to 30 μK. Therefore we attribute this high temperature to a lack of laser power along this axis. During the experimental optimization, we always set the beam powers as low as possible. However, for the x-MOT beam this choice is suboptimal. Indeed we verified experimentally that this power can be increased without compromising the MOT's performance along the other axes.

As explained in section 3.4, ^{87}Sr MOTs addressing only the $^1S_0$ F $= 9/2 - {}^3P_1$ F$' = 11/2$ transition exhibit losses that are not present in our MOT. We attributed this behavior to optical pumping to the $^1S_0$ F $= 9/2$ $m_F = -9/2$ state that is not present in other ^{87}Sr

	Experiment	Simulation
T_x (µK)	Unknown	59 (8)
T_y (µK)	7.5(2)	12 (2)
T_z (µK)	14.2(2)	10 (1)
Width σ_x (mm)	Unknown	2.6 (2)
Width σ_y (mm)	0.689(8)	0.9 (1)
Width σ_z (mm)	1.91(2)	1.3 (2)

TABLE 3.3: Comparison between the simulated temperature and cloud size and the corresponding experimental values. The table shows the mean of 200 simulated ten-second trajectories. The uncertainties reflect the standard deviation of the data. For each trajectory the temperature is calculated as $T = 2E/k_B$ and the width follows the standard deviation of the particle's time-dependent position. Here E is the time-averaged kinetic energy of the particle and k_B is the Boltzmann constant.

MOTs. Here we use this simulation to calculate the average occupation probability of the $^1S_0$ F = 9/2 Zeeman sub-levels and verify this interpretation (see figure 3.13 (a)). Our simulation predicts that 85(6) % of the atoms occupy the F = 9/2 $m_F = -9/2$ state. By contrast, the occupation probability of the F = 9/2 $m_F = -5/2$ is much lower, 0.6(2) %, and the occupation of untrapped states is close to zero, confirming our previous interpretation.

So far we have focused our attention on the dynamics of atoms that have reached the MOT. However, before they reach the MOT they need to be slowed. In subsection 3.4, we explained how this slowing takes place. In a nutshell, atoms reach the lower chamber, where the MOT is located, with a velocity distribution peaked at $\sim 4\,\text{m} \cdot \text{s}^{-1}$. Due to the low scattering rate of the $^1S_0 - {}^3P_1$ transition, these atoms need to be slowed before they reach the MOT. The vertical MOT beam slows them in a distance of $\sim 10\,\text{cm}$, about 20 times the vertical size of the MOT. To do so the frequency of this beam is modulated with a large span, to compensate for the large Doppler shift of the incoming atoms. This laser will be resonant when the difference between the Doppler shift and the Zeeman shift lies within the laser detuning span of the laser. Mathematically this condition can be defined as

$$\Delta_2 < \delta_Z(B(y)) - \delta_D(v_y) < \Delta_1 \tag{3.1}$$

Here $\delta_D(v_y)$ is the Doppler shift, $\delta_Z(B(y))$ the position-dependent differential-Zeeman shift resulting from the quadrupole field of the MOT, and Δ_1 and Δ_2 are the vertical MOT beam start and stop frequency detunings given in subsection 3.5 Table 3.1 (YMOT). For ^{87}Sr the differential Zeeman shift will depend on the state the atoms are in. Therefore the slowing dynamics will depend on the state the atoms occupy when they reach the lower
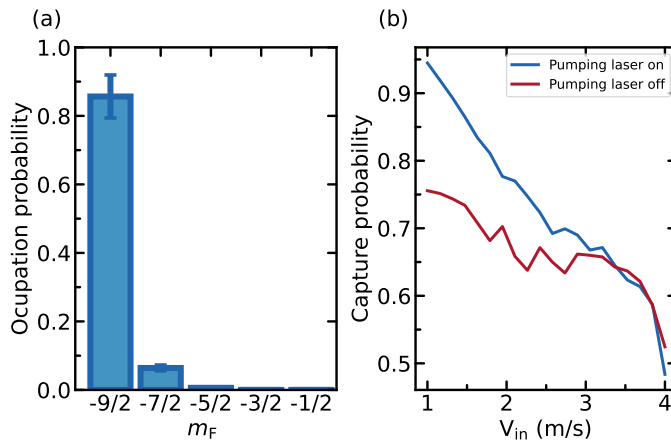
FIG. 3.13: (a) Simulated ground state distribution of the MOT atoms. The data shows the average occupation of 200 ten-second trajectories and the error bars show the corresponding standard deviation. For this simulation the initial position is set to 13 mm below the quadrupole center (roughly at the location of the MOT cloud) and the initial velocity follows a Gaussian distribution. (b) Capture probability of atoms with varying incoming velocity to the lower chamber V_{in} with the pumping light on and off. To obtain this data, we simulate 50 different trajectories for each possible initial state of the $^1S_0$ F = 9/2 manifold. The given data is an average across all of the simulated 500 trajectories and the initial position is set to 2.5 cm above the quadrupole center.
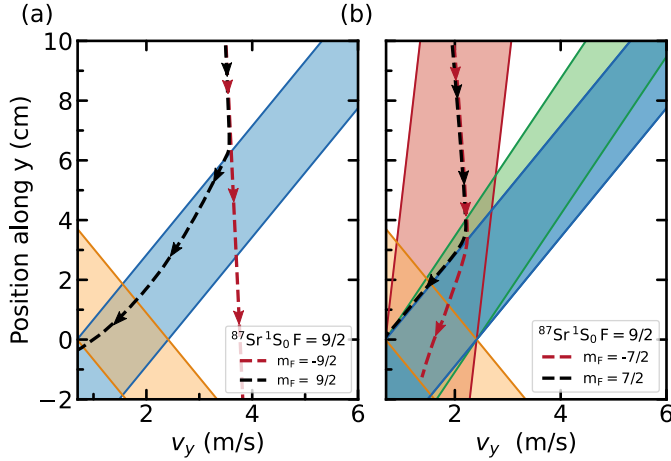
FIG. 3.14: Phase-space plot of falling ^{87}Sr atoms under the influences of the slowing beam, under different conditions. In (a) the atom reaches the lower chamber in the F = 9/2 m_F = 9/2 (black dashed line) and F = 9/2 m_F = −9/2 (red dashed line) states. In (b) the atom reaches the lower chamber in the $^1S_0$ F = −7/2 m_F = −7/2 state with the pumping beam on (black dashed line) and off (red dashed line). The dashed lines show the average of 50 different simulated trajectories. The highlighted regions show the resonance condition of different $^1S_0 - {}^3P_1$ transitions given by equation 3.1. To calculate these regions we have used the linear approximation for the magnetic field used in the simulation. The yellow, blue, and green regions show the resonance conditions of the $m_F = -9/2 - m_{F'} = -11/2$, $m_F = 9/2 - m_{F'} = 11/2$ and $m_F = 9/2 - m_{F'} = 7/2$ cooling transitions respectively. The red region gives the resonance condition of the $m_F = 9/2 - m_{F'} = 9/2$ pumping transition. For simplicity not all of the possible transitions are shown. We have also omitted the error of the trajectories.

chamber.

In figure 3.14 (a) we show two simulated trajectories for different starting conditions. If the atom reaches the lower chamber in the $^1S_0$ F = 9/2 m_F = 9/2 (black line) the Zeeman shift is favorable and the atom is efficiently slowed. By contrast, if the atom reaches the lower chamber in the m_F = −9/2 state, the Zeeman shift is unfavorable and the atom is only weakly addressed (red line). Fortunately the σ^+ polarized slower tends to rapidly pump atoms to favorable states, thus enhancing the slowing.

This optical pumping can be further enhanced by using a dual-frequency configuration for the slower beam, addressing both the $^1S_0$ F = 9/2 − $^3P_1$ F′ = 11/2 "cooling" transition and the $^1S_0$ F = 9/2 − $^3P_1$ F′ = 9/2 "pumping" transition. In figure 3.14 (b) we show two different simulated trajectories with the pumping light on and off, the black and red dashed lines respectively. In both cases the atom reaches the slowing region at $\sim 2\,\text{m}\cdot\text{s}^{-1}$ and in the $^1S_0$ F = −7/2 m_F = −7/2 state. In this case the pumping transition is resonant, so

if the pumping beam is turned on, the atom is rapidly brought to the efficiently-slowed $^1S_0$ F $= 9/2$ $m_F = 9/2$ state resulting in enhanced trapping (black line). By contrast, if the pumping light is not turned on, the average slowing force is greatly reduced (red line).

To further illustrate the pumping effect we calculate the capture probability when the atoms arrive in the lower chamber at different velocities when the pumping light is on or off. The resulting data is shown in figure 3.13 (b). At low velocities the slowing is enhanced thanks to the influence of the pumping light. At higher velocities the pumping light is no longer resonant due to the high Doppler shift, and the estimated capture probability does not change. Across all the calculated velocities and within the calculated uncertainty, the pumping light either improves the capture provability or it does not influence it.

Simulation description

Here we briefly describe the simulation used in chapter 3. For the interested reader who wishes to understand this simulation in detail the code has been made available on GitHub, see [174].

In this simulation the initial conditions of the atoms are defined by their start velocity, position, and internal state. The simulation uses realistic laser parameters and approximates the magnetic field as an ideal, axially symmetric quadrupole field, using the same centre position and vertical field gradient as the real MOT magnetic field. The simulation runs in discrete time steps of duration $\Delta_t = 1\,\mu s$. This time step is much shorter than the shortest relevant physical timescale (the lifetime of the $^3P_1$ state), but long enough to be computationally feasible. The simulation runs for $n = t_{\text{sim}}/\Delta_t$ steps, where t_{sim} is the simulation time. In each step the atoms' velocity v, and position r are updated according to the relations

$$\vec{v}_{n+1} = \vec{v}_n + \vec{g} \cdot \Delta_t + \Delta\vec{V}_{\text{lasers}}, \tag{3.2}$$

$$\vec{r}_{n+1} = \vec{r}_n + \vec{v}_n \cdot \Delta_t. \tag{3.3}$$

Here $\vec{g}$ is the acceleration of gravity and $\Delta\vec{V}_{\text{lasers}}$ is the velocity change due to the influence of the laser light. To calculate $\Delta\vec{V}_{\text{lasers}}$ we follow these steps:

If the atom is in an excited state

A decay probability to the ground state is estimated as $P_{\text{decay}} = \Gamma \cdot \Delta_t$. A pseudo-random number n_{random} [3] is used to decide if the atom decays to the ground state.

---

[3]Here all the random numbers are assumed to be evenly distributed between zero and one

If $n_{\text{random}} < P_{\text{decay}}$ then the atom decays to the $^1S_0$ F $= 9/2$ ground state. The Zeeman sub-level that the atom decays into is selected according to the transition strength, given by the Clebsh-Gordan coefficients and another random number. Finally $\Delta\vec{V}_{\text{lasers}} = (\hbar k/m) \cdot \vec{u}$, where m is the mass of the atoms, k is the wave-vector of the light, $\hbar$ is the reduced Planck constant and $\vec{u}$ is a unit vector oriented in a random direction.

If $n_{\text{random}} > P_{\text{decay}}$ the internal state of the atom is left unchanged and $\Delta\vec{V}_{\text{lasers}} = 0$.

If the atom is in the ground state

First, for each laser we estimate the probability of scattering a photon on each, σ^+, σ^-, and π transition as:

$$P_{\sigma^+,\sigma^-,\pi} = \Delta_t \cdot \Gamma \cdot \sum_{n=1}^{N_{\text{comb}}} \frac{s/2}{1+s+4\left(\frac{\Delta_n - \delta_{\text{Doppler}} - \delta_{\text{Zeeman}}}{\Gamma}\right)^2}. \tag{3.4}$$

$$s = \frac{I}{I_{\text{sat}}N_{\text{comb}}} \cdot (C\{\sigma^+,\sigma^-,\pi\} \cdot p\{\sigma^+,\sigma^-,\pi\})^2. \tag{3.5}$$

Because the frequency of the lasers is modulated, resulting in a frequency comb (see section 3.5), the summation extends to all the comb-lines of the laser. This approximation holds when only one line is close to resonance. Here, C is the Clebsch-Gordan coefficient of the addressed, σ^+, σ^- or π transition, $p\{\sigma^+,\sigma^-,\pi\}$ is the respective polarization decomposition of the laser, I is the laser intensity at the location of the particle, I_{sat} is the saturation intensity of the transition, δ_{Doppler}, is the Doppler shift with respect to the beam, δ_{Zeeman} is the Zeeman shift of the transition and Δ_n is the detuning of the nth comb-line from the unperturbed transition. Here we use realistic laser parameters and we estimate the Zeeman shift using the quadrupole gradient of the MOT.

Using equation 3.4, for each laser we obtain three numbers that give the scattering probability on each σ^+, σ^-, π transition. Similarly to above, a laser and a transition is selected randomly with a probability weighted by the scattering probability of the laser and the transition.

Finally $\Delta\vec{V}_{\text{lasers}}$ is calculated based on a random number n_{random} and on the scattering probability of the selected laser:

If $n_{\text{random}} > P_{\text{scattering}}$ the internal state of the atom is left unchanged and $\Delta\vec{V}_{\text{lasers}} = 0$.

If $n_{\text{random}} < P_{\text{scattering}}$ the internal state of the atom is updated according to the addressed transition and $\Delta\vec{V}_{\text{lasers}} = \left(\hbar\vec{k}/m\right) \cdot \vec{l}$, where $\vec{l}$ defines the propagation direction of the chosen laser.

After calculating $\Delta\vec{V}_{\text{lasers}}$ and updating the internal state of the atom accordingly we continue from equation 3.2. These simulation steps repeat until the desired simulation time

has been reached.

Chapter 4

Sisyphus Optical Lattice Decelerator

The Sisyphus Optical Lattice Decelerator (SOLD) is a proof-of-principle demonstration of a theoretical proposal designed to laser cool (anti)hydrogen [91]. Our demonstration is simplified by the use of strontium, which has easily accessible laser cooling transitions, quite in contrast to (anti)hydrogen. For us the SOLD promised to vastly increase the energy removed per laser-cooling photon and, as a consequence, allow us to reduce the laser power used in our steady-state architecture. We hoped that, with lower laser power, a longer lifetime of high phase-space density samples in our system would follow, ultimately allowing us to realize our main goal, producing the first steady-state BEC.

The perceptive reader will have already realized that we did not use the SOLD in the steady-state BEC experiment [37]. When we started working on this research there were many missing pieces left in the steady-state BEC puzzle. One of which was to slow the atoms in the transfer guide and load them into the reservoir. The SOLD was investigated as a possible solution to this challenge. However, the SOLD by itself proved insufficient to solve the puzzle and once we completed it, the SOLD was not required.

On a personal note , I am very happy with the end result. The SOLD is an additional valuable tool for atomic physicists, which will undoubtedly prove useful in other situations. Moreover, the SOLD was the first research project I worked on as part of the atom laser team at the University of Amsterdam. I still remember long weekends and long nights taking data for the publication presented here.

In the publication on the SOLD reproduced here, we present a novel cooling scheme, which in the future might be integrated into our experiment to achieve higher steady-state phase-space density.

Publication: Sisyphus Optical Lattice Decelerator

Chun-Chia Chen, Shayne Bennetts, Rodrigo González Escudero, Florian Schreck and
Benjamin Pasquiou*

*Van der Waals-Zeeman Institute, Institute of Physics, University of Amsterdam, Science Park 904,
1098XH Amsterdam, The Netherlands*

Leading tests of the Standard Model, like measurements of the electron electric dipole moment or of matter/antimatter asymmetry are built upon our ability to laser cool atoms and molecules to ultracold temperatures. Unfortunately, laser cooling remains limited to a minute collection of species with very specific electronic structures. To include more species, such as polyatomic molecules or exotic atoms like antihydrogen, new cooling methods are needed. Here we demonstrate a method based on Sisyphus cooling that was proposed for laser cooling antihydrogen. In our implementation, atoms are selectively excited to an electronic state whose energy is spatially modulated by an optical lattice, and the ensuing spontaneous decay completes one Sisyphus cycle. We show this method eliminates many constraints of traditional radiation pressure based approaches, while providing similar atom numbers with lower temperatures. This laser cooling method can be instrumental in bringing new exotic species and molecules to the ultracold regime.

4.1   Introduction

Precision measurement with cold atoms and molecules is allowing us to probe the validity and limitations of the Standard Model [112, 175], including searches for the electron electric dipole moment [176–178], for dark matter [4, 73], and for variations in fundamental constants [74, 76, 179]. Recent breakthroughs in laser cooling, focused on using molecules with close-to-diagonal Frank-Condon factors [180–183], have been crucial enablers for many of these experiments.

   Yet many of today's most exciting proposals require first extending these successes to efficiently cool new atomic and molecular species. For example, the ability to precisely compare the spectra of hydrogen with anti-hydrogen might shed light on one of the most important mysteries of physics today, the asymmetry between matter and antimatter. However, the ability to generate a robust trapped sample of ultracold antihydrogen [184–189] is strongly constrained by the limitations of current laser technology at 121.6 nm [190–193]. Other proposals call for ultracold samples of complex, polyatomic molecules [194–198]. While the use of radiation pressure has been wildly successful at slowing some atomic species, the need to scatter vast numbers of photons makes it difficult to apply these methods to slow species without very closed cycling transitions. Common molecules with a myriad of internal states and leaky transitions typically suffer from heavy losses. There remains a strong need for the continued development of new laser cooling methods in order to tackle these important frontiers.

   A range of approaches have been devised to achieve improved performance while relaxing constraints imposed by traditional Doppler cooling techniques. For example, rapid cycling using stimulated emission can provide stronger momentum transfer without spontaneous heating or loss from non-closed cycling transitions. This is demonstrated in bichromatic force cooling [199, 200], adiabatic rapid passage [201] and SWAP cooling [162] but it requires intense resonant light not available for some applications like at the 121.6 nm transition needed for antihydrogen. Alternatively, Sisyphus-like cooling methods [202], where kinetic energy is converted into potential energy, can function effectively even at very low excitation rates and are routinely applied to beat the Doppler temperature limit [203]. Examples of this approach include Zeeman-Sisyphus decelerators [204] and Rydberg-Stark decelerators [205, 206], where a photon excitation changes the internal state allowing a significant part of the slowing to be done by an externally applied electromagnetic field gradient.

   In this work, we present a proof-of-principle demonstration of a class of proposals developed to laser cool antihydrogen [91] and other species [207–209]. Our demonstration uses a Sisyphus-like deceleration mechanism to slow a continuous stream of strontium
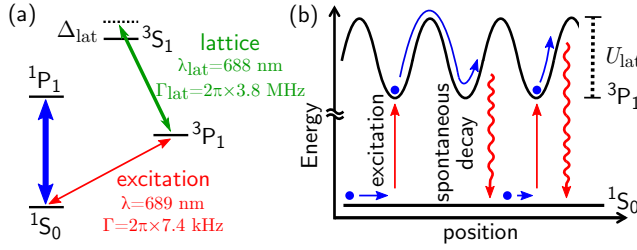
FIG. 4.1: SOLD working principle. (a) Relevant electronic levels of stron-
tium and the two transitions used for excitation and optical lattice creation,
both necessary for the SOLD. (b) Schematic of two typical cooling cycles,
from excitation to spontaneous decay.

atoms without using radiation pressure. The method uses a 1D optical lattice acting on the
excited $^3P_1$ electronic state, combined with a selective excitation mechanism that transfers
atoms to the lattice potential minimums. We explore the performance of this method,
which we name a Sisyphus Optical Lattice Decelerator (SOLD). To compare with traditional
radiation pressure schemes we also substitute the SOLD with a Zeeman slower using the
same transition as our excitation mechanism. In principle, by using a deep lattice very
few excitation photons can be sufficient to bring fast atoms to rest, making SOLD a good
decelerator candidate for exotic species and molecules without a closed cycling transition
[180–183, 194–198].

This paper is structured as follows. In Section 4.2 we present the working principle
of the SOLD. We describe in Section 4.3 our implementation to slow a beam of strontium
atoms and measure its performance. Section 4.4 describes the various parameter regimes
for the removal of an atom's kinetic energy, then elaborates on the SOLD efficiency in terms
of the required number of scattered photons. In Section 4.5 we explain the behavior of the
excitation rate, and from this analysis we provide a simple formula for the capture velocity
of this cooling method. We compare in Section 4.6 the SOLD performance with typical
radiation pressure based laser cooling. Last, in Section 4.7 we discuss eventual limitations
for the applicability of this method, and we conclude in Section 4.8.

4.2   Principle

The working principle of the SOLD relies on a 3-level system coupled by two optical transi-
tions, something ubiquitous for both atomic and molecular species. Our implementation
using strontium is depicted in Fig. 4.1(a). An optical lattice is formed using a pair of coher-
ent counter-propagating beams with a frequency in the vicinity of the $^3P_1 - {}^3S_1$ transition.
This produces a spatially modulated coupling between the $^3P_1$ and $^3S_1$ states and thus

a spatially modulated light shift on the excited $^3P_1$ state. The ground $^1S_0$ state remains essentially unaffected. By applying a laser resonant with the $^1S_0 - ^3P_1$ transition, atoms can be excited into the $^3P_1$ state where they experience the force associated with the lattice potential, see Fig. 4.1(b). If the linewidth Γ of the $^1S_0 - ^3P_1$ intercombination line is much smaller than the lattice height $U_{lat} \gg \hbar\Gamma$, this "excitation" laser can be tuned to selectively address the bottom of the lattice sites. For high enough velocity $v > \lambda_{lat}\Gamma$, atoms excited into $^3P_1$ will then climb a significant fraction of the lattice potential hills and lose kinetic energy before spontaneously decaying to the ground state as shown in Fig. 4.1(b). As atoms in $^1S_0$ propagate along the lattice axis, this cooling cycle repeats forming a Sisyphus mechanism. By creating a very high lattice, it is theoretically possible to remove most forward kinetic energy within distances of a few lattice periods or with a single cycle, as in Rydberg-Stark decelerators [205, 206]. The temperature limit for this scheme is the higher of an effective Doppler temperature depending on Γ [208], or the recoil temperature.

4.3 Experimental setup

To demonstrate the feasibility of the SOLD experimentally, we implement the setup shown in Fig. 4.2(a). We start with a magneto-optical trap (MOT) for ^{88}Sr operating in a steady-state regime on the 7.4 kHz-linewidth $^1S_0 - ^3P_1$ transition, as described in our previous work (configuration "Red MOT I" of [35]). We overlap this MOT with an optical dipole trap acting as a "transport" guide [36]. This 1D guide is $\sim 35\,\mu K$ deep at the MOT location and propagates horizontally along the z axis. By adding a "launch" beam resonant with the $^1S_0 - ^3P_1$ π transition and pointed at the overlap between the MOT and transport guide, we outcouple MOT atoms into the guide with a well-controlled mean velocity ranging from 0.08 to $0.25\,m \cdot s^{-1}$ [36]. Atoms then propagate along the guide for $\sim 3.7\,cm$ until they reach the decelerator region.

We produce a 1D lattice potential with a pair of counter-propagating laser beams whose frequency is blue-detuned by $\Delta_{lat} \approx 2\pi \times 30\,GHz$ from the $^3P_1 - ^3S_1$ transition. The lattice beams cross the transport guide at a shallow angle of $6°$, overlapping the atomic beam for about 3.4 mm. Excitation from the $^1S_0$ to $^3P_1$ state is provided by illuminating the atoms from the radial direction. This is implemented using a pair of counter-propagating horizontal beams and a single vertical beam propagating upward, with $1/e^2$ diameters of 28.8 mm and 36 mm, respectively. These "excitation" laser beams are 15 kHz red detuned from the π transition and their combined intensity corresponds to a saturation parameter of ~ 1. In addition to state excitation, these beams provide an optical molasses, which brings the atoms' radial temperature to $\sim 2\,\mu K$. Importantly, we don't apply any near-resonant light that would be capable of slowing atoms in the z axis in the absence of the SOLD optical
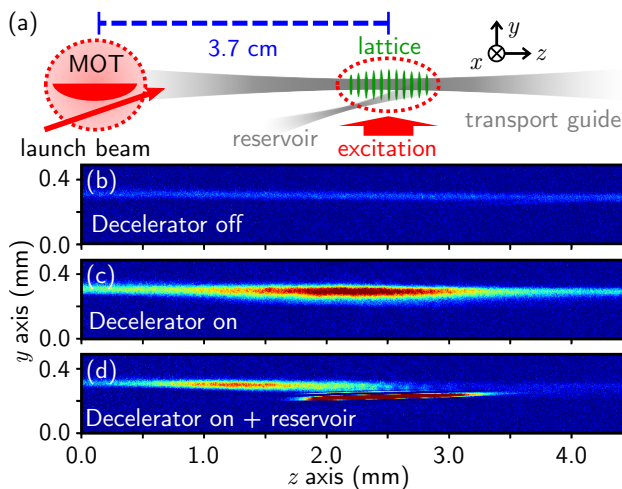
FIG. 4.2: (a) Side view of the setup. (b,c,d) $^1S_0 - ^1P_1$ absorption imaging pictures of the atomic beam at the decelerator location, (b) without lattice, (c) with lattice, and (d) with lattice and reservoir.

lattice. Despite the possibility for other orientations of the excitation beams, as suggested in Ref. [91], we initially chose the configuration described above in order to demonstrate that radiation pressure is not directly involved in the slowing of atoms, and just climbing the lattice potential removes kinetic energy.

We operate the decelerator on a guided atomic beam continuously fed by the MOT, with a homogeneous axial density across the full field of view of our imaging system, see Fig. 4.2(b). When the lattice is switched on, the density in the overlap region between the atomic and lattice beams sharply increases, suggesting an accumulation of slowed atoms, as shown in Fig. 4.2(c). Without either lattice beam or with a large (160 MHz) frequency difference between the two lattice beams, this feature vanishes. Fig. 4.2(c) also shows that some atoms travel completely across the lattice region due to incomplete slowing or by diffusion. Note that our slowing mechanism is fully compatible with a steady-state apparatus, and we perform our measurements after reaching steady state.

For better characterization of the SOLD, and since we are concerned about diffusion of slowed atoms, we add a second "reservoir" dipole trap beam. This beam crosses below the transport guide at the lattice location, with an offset adjusted to allow slow atoms to pass from the guide into the reservoir while not significantly disturbing the potential landscape of the guide. With the help of the radial optical molasses, the reservoir collects and stores slowed atoms 2 mm away from the crossing. We show one example of loading into this reservoir in Fig. 4.2(d), which also exemplifies a means of atom extraction from our ultracold atom source. We show in Fig. 4.3 the measured atom number loaded into
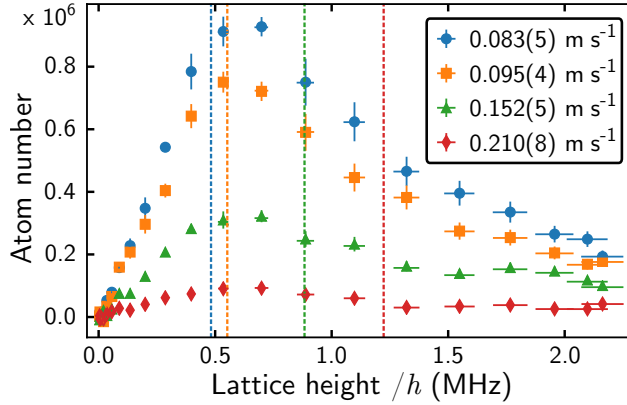
FIG. 4.3: SOLD efficiency. Measured steady-state number of atoms slowed by the SOLD and loaded in the reservoir, for varying lattice height and four different initial velocities. Dashed vertical lines give the criterion of Eq. (4.3) for $m = 1$. The vertical error bars represent standard errors from binned data points. The horizontal error bars origin is described in App. A.

the reservoir by the SOLD. The efficiency is poor for small lattices, as not enough kinetic energy is removed before atoms leave the lattice location. For increasing lattice height, we observe a clear loading optimum, followed by a slow decrease. As we will discuss later on in Section 4.5, these two features originate from the behavior of the excitation rate to $^3P_1$.

The SOLD deceleration scheme brings atoms ultimately to zero mean velocity in the reference frame of the lattice. By applying a small frequency difference between two lattice beams, a lattice will move at a well-controlled velocity [210, 211]. This implies that the SOLD can ideally decelerate or accelerate atoms to any desired velocity (see App. C). Here we use the moving lattice to characterize the reservoir dipole trap. The loading of this reservoir is both sensitive to the mean velocity of atoms and to the location they end up when reaching zero mean velocity. We characterize the velocity acceptance of the reservoir by varying the frequency difference between the two lattice beams. The loading efficiency of the reservoir depending on the lattice velocity is shown in Fig. 4.4. It can be fitted by a Gaussian whose width is $\sigma_v = 0.0084(4)\,\mathrm{m\cdot s^{-1}}$, centered at $v_R \sim -0.002\,\mathrm{m\cdot s^{-1}}$. This slight departure from zero velocity can be explained by the orientation of the reservoir relative to the guide, which favors the loading of atoms that move backward. The small velocity window for which the loading efficiency is substantial exemplifies the slowing effect of the SOLD.
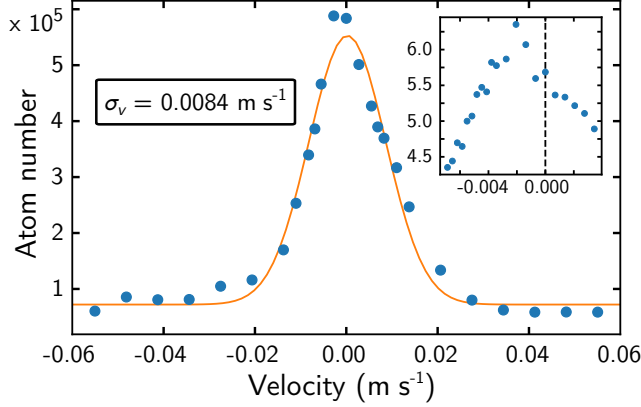
FIG. 4.4: Velocity selectivity of the reservoir loading, measured by varying the lattice velocity. The line is a Gaussian fit of the data with width σ_v. The inset shows the same type of measurement on a much narrower velocity range, highlighting the center velocity of about $v_R \sim -0.002\,\mathrm{m}\cdot\mathrm{s}^{-1}$.

4.4 Kinetic energy regimes and photon scattering efficiency

We can understand the SOLD slowing efficiency observed in Fig. 4.3 with a simple semi-classical model describing its various working regimes, which depend on the relative magnitude of the atoms' kinetic energy with respect to lattice height. Consider atoms initially excited into the $^3P_1$ state at the bottom of the lattice potential. In Fig. 4.5(a), we plot the dependence of the average energy lost per cooling cycle E_{lost} with incoming velocity v and lattice height. For high kinetic energies compared to the lattice height $\frac{1}{2}mv^2 \gg U_{\mathrm{lat}}$, atoms travel through several lattice sites and the energy lost tends to $E_{\mathrm{lost}} \to \frac{U_{\mathrm{lat}}}{2} / \left(1 + \left(\frac{\lambda_{\mathrm{lat}}\Gamma}{4\pi v}\right)^2\right)$, see App. B. When $v \gg \lambda_{\mathrm{lat}}\Gamma$, the energy lost saturates to $E_{\mathrm{lost}} \to U_{\mathrm{lat}}/2$. A striking feature of Fig. 4.5(a) is that E_{lost} exhibits an efficiency peak for $\frac{1}{2}mv^2 = U_{\mathrm{lat}}$. In this case, atoms have just enough energy to climb one lattice maximum, where they spend most of their time and are thus more likely to undergo spontaneous emission. The energy lost in this regime asymptotically reaches $E_{\mathrm{lost}} \to U_{\mathrm{lat}}$ for $v \gg \lambda_{\mathrm{lat}}\Gamma$, see App. B. Let us note that, in contrast to Ref. [91] that relies also on a spatial modulation of Γ, the effective rate of spontaneous emission in our case is higher on lattice hills only because of the increased time atoms spend there.

Laser cooling techniques can be benchmarked by the average number of photons that need to be scattered to slow atoms from some initial velocity to the technique's temperature limit. This is particularly relevant for species without a cycling laser cooling transition, like most molecules [180–183, 194–198], where there is a small, finite number of photons
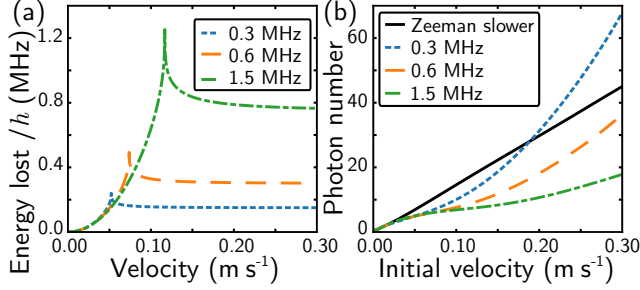
FIG. 4.5: Theoretical efficiency of our cooling scheme. (a) Average energy lost E_{lost} during a single cooling cycle, for varying velocity before excitation. (b) Total number of cycles/excitation photons needed for the SOLD compared with a Zeeman slower, depending on the initial velocity. The black line shows the ZS behavior, while the dotted, dashed and dash-dotted lines are for the SOLD with various lattice heights.

allowed to be scattered before the species decays to a dark state and is lost. Using the results of Fig. 4.5(a) repeated over several cycles with decreasing velocity, we calculate the number of excitation photons needed to reach a kinetic energy equivalent to a temperature below $2\,\mu$K and present it in Fig. 4.5(b). This temperature was arbitrarily chosen ~ 4 times larger than the recoil temperature for the $^1S_0 - ^3P_1$ transition, the relevant limit in our case. For comparison with radiation pressure based laser cooling methods, we also show in Fig. 4.5(b) the number of photons required in the case of a Zeeman slower (ZS) [212]. The SOLD always requires fewer cooling photons than the ZS for a lattice height satisfying $U_{lat}/h > v/\lambda_{lat}$.

4.5   Excitation rate and critical velocity

The SOLD ability to slow atoms with high incoming velocities is strongly dependent on the excitation rate. We model this rate by solving the optical Bloch equations for a two-level system corresponding to the $^1S_0$ and $^3P_1$ states, coupled by the excitation laser with Rabi frequency Ω. The time-dependent Schrödinger - von Neumann equation for the density operator ρ is

$$\frac{d\rho}{dt} = -\frac{i2\pi}{h}[H, \rho] + L, \tag{4.1}$$

with h the Planck constant, L the usual term to account for the spontaneous emission due to Γ, and with the Hamiltonian H written as

$$H = \begin{pmatrix} 0 & \Omega/2 \\ \Omega/2 & U_{lat}\sin^2(2\pi\,v\,t/\lambda_{lat}) \end{pmatrix}. \tag{4.2}$$
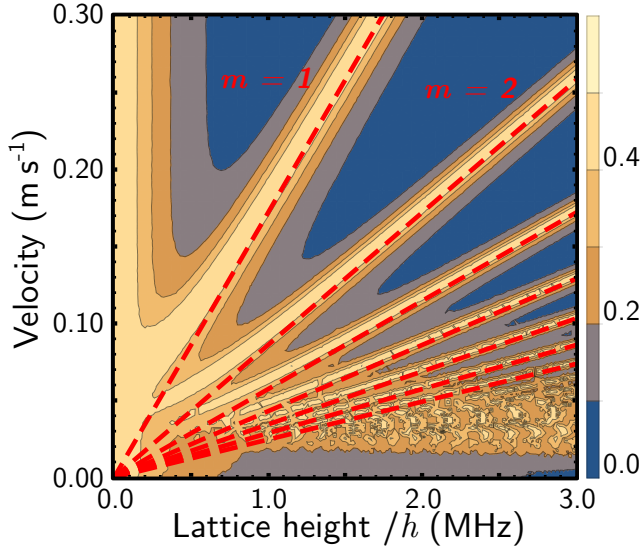
FIG. 4.6: Population transferred to the $^3P_1$ state depending on the lattice height and the atom velocity. For clarity of the figure, the population is calculated for a saturation parameter of the excitation transition of ~ 1600 instead of the $0.1 \sim 10$ typically used. Dashed red lines show the condition of Eq. (4.3) for $m \in \{1...7\}$.

We numerically solve Eq. (4.1) with time, starting with all the population in $^1S_0$ at $t = 0$. For this calculation, we assume a constant velocity v, which is valid for $\frac{1}{2}mv^2 \gg U_{\text{lat}}$. After a variable time, the $(\Omega, U_{\text{lat}}, v)$-dependent solution for the excited population reaches a steady-state only slightly perturbed by the time-dependent detuning produced by travelling within the lattice. Averaging over this small perturbation, we get the population in the $^3P_1$ state shown in Fig. 4.6. Let us note that solutions for Hamiltonians similar to Eq. (4.2) have been analysed before, in particular in the frequency domain [213].

The remarkable feature in Fig. 4.6 is the presence of multiple resonances where there are high excitation rates. These can be explained by in-phase multiple π-over-N pulses. Indeed, only at the bottom of a lattice site is the detuning small enough to excite a significant population to $^3P_1$. While the atoms propagate from one site to the next, the distributions in $^1S_0$ and $^3P_1$ states acquire different phases. Once at the next site, further population is efficiently excited to $^3P_1$ only if the dephasing is equal to multiples of 2π, in which case the steady-state excited population is high. This behavior can be confirmed by looking at the evolution of the Bloch vector associated with ρ, displayed in Fig. 4.7 for two cases.

We can give a simple quantitative criterion for the positions of these excitation rate resonances. The phase accumulated during the propagation through one lattice period is $\Phi = \Delta\, T$, with $T = \frac{\lambda_{\text{lat}}}{2v}$ the propagation time and Δ the dephasing, taken as the average
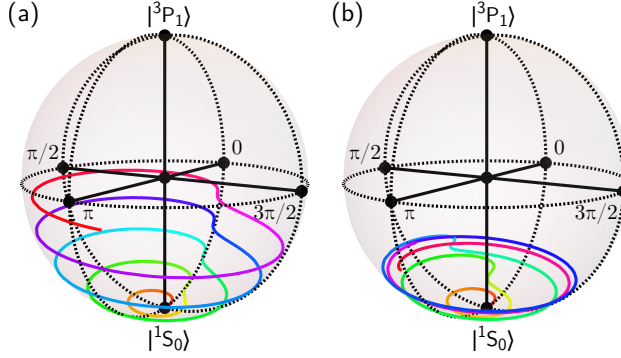
FIG. 4.7: Evolution of the Bloch vector on the Poincaré sphere, shortly (for 5 "pulses") after the application of the SOLD. Atoms begin in the $^1S_0$ state at the location of a lattice site. The saturation parameter of the excitation to $^3P_1$ is set for clarity to about 60, and the lattice height is $h \times 600\,\text{kHz}$. The velocity in (a) $v = 0.1035\,\text{m} \cdot \text{s}^{-1}$ is such that the accumulated phase during the travel time between two sites is close to $\Phi = 2\pi$, while in (b) where $v = 0.09\,\text{m} \cdot \text{s}^{-1}$ this condition is not met.

detuning due to the lattice, giving $\Delta = 2\pi \frac{1}{h} \frac{U_{\text{lat}}}{2}$. The condition $\Phi = m \times 2\pi$ (with $m \in \mathbb{N}$) leads to the relation

$$\frac{U_{\text{lat}}}{h} = m \times \frac{4v}{\lambda_{\text{lat}}}, \tag{4.3}$$

This criterion is shown as dashed red lines for $m \in \{1, ..., 7\}$ in Fig. 4.6. Due to the high density of the lines with $m > 1$, for low incoming velocities the loading efficiency optimums observed in Fig. 4.3 correspond mainly to fulfilling the criterion of Eq. (4.3) for the case $m = 1$.

   Including both the average lost energy E_{lost} and the excitation rate both depending on (U_{lat}, v), we model the behavior of the SOLD by solving classically the evolution of the atoms' velocity with time, under an effective force $F(U_{\text{lat}}, v) = -\Gamma \times \rho_{3P_1}(U_{\text{lat}}, v)\, E_{\text{lost}}(U_{\text{lat}}, v)$. We reproduce qualitatively all features of the experimental data, see App. B. The criterion of Eq. (4.3) with $m = 1$ effectively dictates the capture velocity of the SOLD

$$v_c = \frac{U_{\text{lat}}\lambda_{\text{lat}}}{4h} \tag{4.4}$$

Let us note that, for a lattice height thus matching the atoms' velocity, the condition $U_{\text{lat}}/h > v/\lambda_{\text{lat}}$ given in Section 4.4 is verified. Therefore, when working in nominal conditions, the SOLD requires less photons than standard radiation pressure based laser cooling methods like the ZS.

TABLE 4.1: Comparison of the SOLD and the Zeeman slower (ZS). The rows give steady-state atom numbers in the reservoir (when present), fluxes, $1/e$ loading times, and reservoir radial (axial) temperatures T_{rad} (T_z). The various configurations are, in order, the SOLD in the transport guide, the SOLD plus the reservoir (R), the ZS plus reservoir and the combination of both.

	SOLD	SOLD+R	ZS+R	SOLD+ZS+R
Atoms ($\times 10^6$)	0.78(01)	0.69(01)	1.87(04)	2.00(10)
Flux ($\times 10^6\,\mathrm{s}^{-1}$)	0.74(04)	0.65(03)	2.11(14)	2.80(15)
Loading (ms)	705(20)	625(52)	434(43)	507(55)
T_{rad} (µK)		1.53(02)	1.08(04)	1.34(02)
T_z (µK)		2.30(06)	5.67(94)	2.59(10)

4.6 Comparison with radiation pressure based cooling

We now experimentally compare the SOLD performance with that of a Zeeman slower. The varying magnetic field for the ZS is provided by the existing MOT quadrupole field, whose gradient in the guide axis is $0.23\,\mathrm{G}\cdot\mathrm{cm}^{-1}$. We then add a laser beam counter-propagating to the transport guide, focused in the SOLD region and with a circular polarization set to address the weak-field seeking $^3\mathrm{P}_1$ $m_{\mathrm{J}} = -1$ state. We demonstrated in previous work that it is possible to operate a ZS on the narrow Sr intercombination line [35]. In Table 4.1, we report a comparison between the two slowing methods. Both give similar results for fluxes and final atom numbers, with an advantage for the ZS, which we attribute mainly to the spatial selectivity of its optical excitation. However, we observe a clear difference in the final axial temperatures T_z within the reservoir, which effectively reflects the final mean velocities. For the SOLD, T_z is almost as low as the radial temperature T_{rad} provided by the molasses cooling, whereas T_z is 2.5 times hotter for the ZS. This is because a Zeeman slower is unable to decelerate atoms to zero velocity, as they remain somewhat resonant with ZS photons and are pushed backwards. By contrast, the final mean velocity for the SOLD is stationary in the frame of the optical lattice, which itself can be chosen arbitrarily [210, 211].

An additional difference is that, since the SOLD does not rely on radiation pressure from the excitation beam to cool, it is possible to use a much broader class of transitions than for standard laser cooling methods. It is for example also possible to use the ZS beam as an excitation beam that features both spatial and velocity selectivity. The lattice, now acting on atoms in $^3\mathrm{P}_1$ $m_{\mathrm{J}} = -1$, is the one charged with decelerating atoms to zero axial velocity. In presence of both lattice and ZS beams, we observe the best number of atoms in the reservoir, while keeping the low temperature T_z due to the SOLD, see Table 4.1.

4.7   Discussion

Let us now turn to considerations for further applications of this cooling scheme. Firstly, it is clear from Fig. 4.6 that, at high velocities, excitation rates are low unless the lattice height matches the conditions of Eq. (4.3). This can be dealt with by temporal modulation of the lattice intensity, which varies the resonance locations. Secondly, for lattices much higher than the transport guide depth, we observe a clear spread of the atomic beam out of the guide. This is due both to the radial anti-confinement from the blue-detuned lattice beams and the slight angle between lattice and transport beams. A red-detuned lattice could remedy this by confining the atoms radially, but this will make correctly tuning the excitation frequency dependent on the lattice intensity.

Thirdly, if the lattice detuning Δ_{lat} is insufficient, atoms in the $^3P_1$ state can be optically pumped by the lattice light to $^3S_1$. If this occurs, atoms can decay from $^3S_1$ to the metastable $^3P_0$ and $^3P_2$ states and exit the cooling cycle. Fig. 4.8 shows, for several lattice laser detunings Δ_{lat}, the effect of optical pumping to $^3S_1$ depending on the lattice height. For detunings that are a few GHz away from the $^3P_1 - ^3S_1$ transition, we see a clear reduction of the maximum atom number slowed and captured in the reservoir. For detunings above 20 GHz, the efficiency seems to converge toward a unique curve, indicating no significant optical pumping. A repumping scheme such as the one used in Ref. [87] can optically pump atoms back to $^3P_1$ in a time short compared to the propagation of the atoms along the lattice. Alternatively, a higher detuning with correspondingly increased intensity solves this issue. Aside from the data of Fig. 4.8, we operate at a lattice detuning of $\Delta_{\mathrm{lat}} \approx 2\pi \times 30$ GHz, for which optical pumping is negligible and the required optical power for best efficiency is only 1.2 mW for each of the two 100 μm-waist beams.

Finally, the initial velocities decelerated in this proof of principle are low compared with several applications of interest, in part due to the small lattice height and deceleration region used. In the proposal of Wu *et al.* [91], the lattice is 78.5 MHz high and the capture velocity is set to $v_{c,\bar{H}} \approx 25$ m $\cdot$ s^{-1}. This proposal is designed to cool trapped antihydrogen, with velocities up to 80 m $\cdot$ s^{-1} and long interaction times including several oscillations of particles in the trap. As a comparison attempt, it would take in these conditions about 20 photon scattering events for an equivalent SOLD setup to bring antihydrogen close to the recoil limit, which, as can be seen in Fig. 4.5(b), is similar to the numbers demonstrated in this work. Let us note that one strength of this laser cooling method is that the high optical power requirement is on the lattice transition and not on the, far more technologically challenging, 121.6 nm excitation transition.
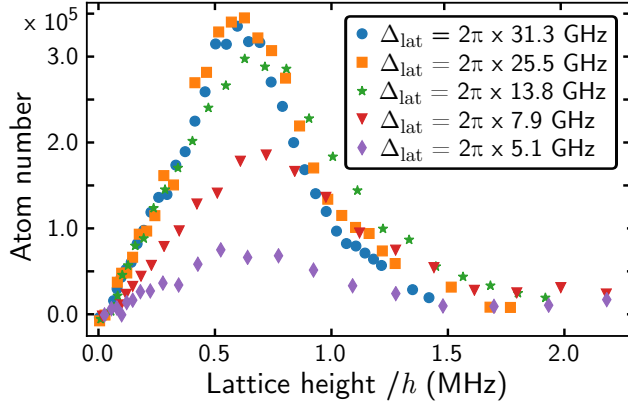
FIG. 4.8: Effect of optical pumping by the lattice light to the $^3S_1$ state. The data show the number of atoms loaded into the reservoir as a function of the lattice height for various detunings of the lattice laser from the $^3P_1 - {}^3S_1$ transition.

4.8 Conclusion

To summarize, we experimentally demonstrate a Sisyphus-like deceleration mechanism to slow and cool strontium atoms without using radiation pressure. Our work validates a class of proposals developed for laser cooling antihydrogen [91] and other species [207–209]. We characterize the SOLD technique in the steady-state regime both experimentally and theoretically. We compare the SOLD with a typical radiation pressure based scheme (Zeeman slower) and find similar atom numbers but lower axial temperature. By combining both techniques, we benefit from the ZS spatial/velocity selectivity and improved SOLD end temperatures. We also consider some improvements and applications to the case of antihydrogen.

Using the SOLD method requires only three easily-met conditions: a three level system, selective excitation in a lattice with $U_{\text{lat}} \gg \hbar\Gamma$, and an initial velocity satisfying $v > \lambda_{\text{lat}}\Gamma$. Such simple requirements can be fulfilled by many systems where laser cooling to the ultracold regime remains a challenge. Already, recent independent work has shown similar Sisyphus cooling effects in optical tweezers [214], and adapting the present laser cooling method to new exotic species and (polyatomic) molecules [180–183, 194–198] is the next logical step. Furthermore, by careful choice of the time sequence for the lattice velocity and intensity, a pulsed version of the SOLD could bring an atom wavepacket to any desired velocity while scattering only a handful of photons.

4.9   Acknowledgements

TABLE 4.2: Relative uncertainties on the relevant parameters used to calcu-
late the lattice height for the $^3P_1$ state.

	uncertainty
Lattice beam power	$\pm 3.0\,\%$
Lattice beam waist	$\pm 1.4\,\%$
Lattice frequency detuning Δ_{lat}	$\pm 0.1\,\%$
Total transition rate $A_{^3P_J-^3S_1}$	$\pm 1.0\,\%$
Total uncertainty	$\pm 4.2\,\%$

Appendix A: Lattice height determination

We need an accurate determination of the lattice height to characterize the SOLD. The
potential of a 1D lattice acting on the $^3P_1$ state depends on its dynamic dipole polarizability
α. In the two-level approximation, valid here because the lattice laser detuning Δ_{lat} is only
a few tens of GHz, the polarizability is given by

$$\alpha \approx \frac{3\epsilon_0 \lambda_{\text{lat}}^3}{8\pi^2} \frac{\Gamma_{\text{eff}}}{\Delta_{\text{lat}}},$$ (4.5)

where ϵ_0 is the vacuum permittivity. The effective rate $\Gamma_{\text{eff}} = \eta\, A_{^3P_1-^3S_1}$ is the effective
transition rate for the $5s5p\,^3P_1 - 5s6s\,^3S_1$ transition, with $\eta = 1/2$ due to the lattice laser
polarization. The relative uncertainties of the parameters contributing to the determination
of the lattice height are listed in Table 4.2. All parameters contributing to the lattice height
and their uncertainties are determined experimentally, except for $A_{^3P_1-^3S_1}$ that we derive
from literature in the following manner.

The branching ratios from the $^3S_1$ state to the three $5s5p\,^3P_J$ states can be calculated
taking into account the fine structure splitting that produces frequency dependent correction
factors. The resulting branching ratios are $^3S_1$ to $(^3P_0,\ ^3P_1,\ ^3P_2) = (12.02\,\%,\ 34.71\,\%,\ 53.27\,\%)$.
The transition rate for $5s5p\,^3P_0 - 5s6s\,^3S_1$ was precisely determined experimentally and
theoretically in Ref. [71, 215]. By scaling this known transition according to the branching
ratios, we arrive at a transition rate $A_{^3P_1-^3S_1} = 2.394(24) \times 10^7\,\text{s}^{-1}$.

Appendix B: SOLD Model

Here we give a description of our model of the SOLD that is an extended version of the
description given in the main text. In order to model our cooling scheme in an insightful
way, we split the problem into two parts: the average energy lost per cooling cycle and the
excitation rate. The excitation rate has been described extensively in the main text. As for

the energy lost, we give below more details than what has already been presented. We then use both energy lost and excitation rate results to simulate the time evolution of the atoms' velocity.

Energy lost

We begin with a study of the energy lost due to the presence of the lattice. We assume that the atoms are excited into the $^3P_1$ state at the bottom of the lattice and we solve the differential equation for the motion $z(t)$ along the lattice propagation axis:

$$\frac{1}{2}mv_0^2 = U_{\text{lat}} \sin^2 k_{\text{lat}} z + \frac{1}{2}m \left(\frac{dz}{dt}\right)^2, \ z(t=0)=0, \tag{4.6}$$

with m and v_0 being respectively the mass and the initial velocity of the atom. U_{lat} is the lattice depth and $k_{\text{lat}} = \frac{2\pi}{\lambda_{\text{lat}}}$ is the wave vector of the lattice light with wavelength λ_{lat}. The solution of this equation can be written in terms of the Jacobi amplitude J_A:

$$z(t) = \frac{1}{k_{\text{lat}}} J_A \left(k_{\text{lat}} v_0 \, t, \frac{2U_{\text{lat}}}{mv_0^2} \right). \tag{4.7}$$

Since the process relies on spontaneous emission towards $^1S_0$, we determine the average energy lost $E_{\text{lost}}(U_{\text{lat}}, v_0)$ by integrating the lattice height explored for a duration set by the natural linewidth Γ of the $^1S_0 - {}^3P_1$ transition,

$$E_{\text{lost}} = \Gamma \int_0^\infty e^{-\Gamma t} U_{\text{lat}} \sin^2(k_{\text{lat}} z(t)) \, dt. \tag{4.8}$$

In Fig. 4.5(a), we show the evolution of E_{lost} for several lattice heights and depending on the incoming velocity. We observe that for high incoming kinetic energies compared to the lattice height $\frac{1}{2}mv_0^2 \gg U_{\text{lat}}$, the energy lost E_{lost} saturates. In this case, atoms travel through several lattice sites, and their propagation tends to $z(t) \to \frac{1}{k_{\text{lat}}} J_A \left(k_{\text{lat}} v_0 \, t, 0 \right) = v_0 \, t$. Eq. (4.8) gives the relation $E_{\text{lost}} \to \frac{U_{\text{lat}}}{2} / \left(1 + \left(\frac{\Gamma}{2k_{\text{lat}} v_0} \right)^2 \right)$. In our experiment $v_0 \gg \lambda_{\text{lat}} \Gamma$, so the average energy lost saturates to $U_{\text{lat}}/2$. One striking feature of Fig. 4.5(a) is that the energy lost exhibits a sharp resonance for $\frac{1}{2}mv_0^2 = U_{\text{lat}}$, where cooling is the most efficient. In this case, atoms have just enough energy to climb on top of the first lattice hill, so they spend most of their time at this location, which makes them more likely to spontaneously emit there and therefore to lose most of their kinetic energy. Indeed, the explored lattice height becomes $U(t) \to U_{\text{lat}} \tanh^2(k_{\text{lat}} v_0 \, t)$, which for $v_0 \gg \lambda_{\text{lat}} \Gamma$ gives an average energy lost reaching asymptotically $E_{\text{lost}} \to U_{\text{lat}}$.
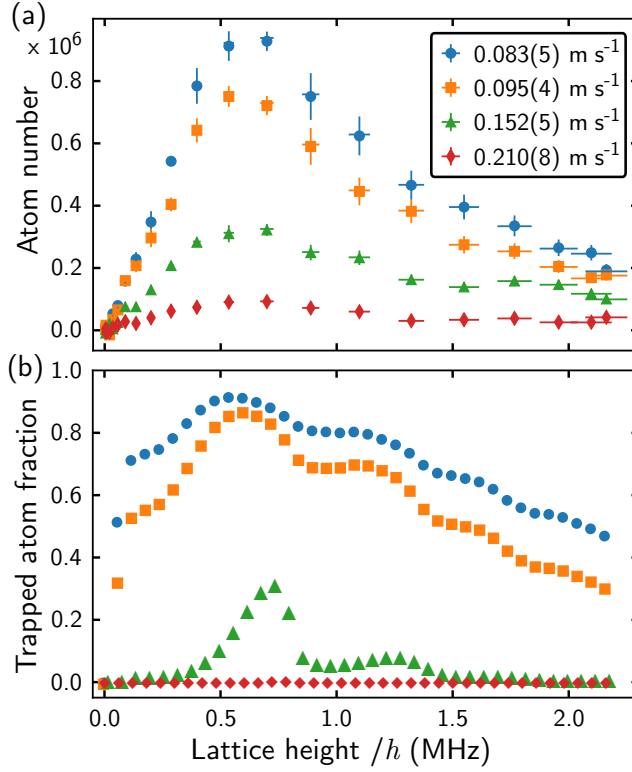
FIG. 4.9: Comparison between (a) the experimental data already shown in
Fig. 4.3 and (b) the results of the theoretical model (see text) for the same
initial mean velocities.

Overall evolution

In order to model the complete behavior of the SOLD, we solve classically the evolu-
tion of the atoms' velocity v with time, under an effective force $F(U_{\text{lat}}, v) = -\Gamma \times$
$\rho_{{}^3P_1}(U_{\text{lat}}, v) E_{\text{lost}}(U_{\text{lat}}, v)$. We carry out this calculation for a packet of atoms whose velocity
distribution follows a (1D) Boltzmann distribution corresponding to the temperature of our
MOT of $6\,\mu K$ summed with an offset corresponding to the measured mean velocity given
by the launch beam. The capture probability in our reservoir is determined by the velocity-
dependent efficiency extracted from the measurement shown in Fig. 4.4, corresponding to a
Gaussian function with a width $\sigma_v = 0.0084\,\text{m} \cdot \text{s}^{-1}$. We thus simulate the time evolution of
the loaded population in the reservoir depending on the lattice height, for the four mean
starting velocities shown in Fig. 4.3. In Fig. 4.9 we compare the results from this model with
our experimental data.

We see a good qualitative agreement concerning the overall behavior with both lattice

height and starting mean velocity. In particular, the locations of the optimums of loading efficiency are well reproduced by our model. These correspond to the case when the starting mean velocity v_0 verifies the criterion of Eq. (4.3) (with $m = 1$). Indeed, in that case atoms are efficiently excited to the $^3P_1$ state, and lose typically a significant amount of energy $U_{\text{lat}}/2$. After spontaneous emission, their velocity is much lower and atoms are in the (U_{lat}, v) region where the density of lines for $m \geq 2$ is high. They are therefore very likely to keep decelerating efficiently. On the contrary, for high velocity v_0, in the region $0 \ll \frac{U_{\text{lat}}}{h} \ll \frac{4v_0}{\lambda_{\text{lat}}}$, atoms will not get excited to $^3P_1$. Our model is thus able to estimate the capture velocity v_c of the SOLD, which is given by

$$v_c = \frac{U_{\text{lat}}\lambda_{\text{lat}}}{4h}. \tag{4.9}$$

Let us note that our model makes several approximations. Indeed the results of the calculations shown in Fig. 4.9(b) are given for one particular evolution time $t = 1.4\,\text{ms}$ that has been chosen for best match with the steady-state experimental data. Since no decay mechanism has been added in the model, the final loading would be with unity efficiency. This chosen deceleration time is rather short, because in this case the saturation parameter of the $^1S_0 - {}^3P_1$ transition is set to ~ 320, for which the calculations suffer less numerical errors compared to more realistic, lower saturation parameters. Nonetheless, the simulations always exhibit the same overall behavior no matter the value of the saturation parameter. Another limitation of our model is that no selection criteria have been chosen for the position of atoms, whereas they must be in the vicinity of the crossing between the transport guide and reservoir to be loaded. Similarly, atoms expelled from the guide by the barrier formed by the blue detuned lattice and the effects of the lattice's slight angle with the guide are not taken into account. Finally, the constant velocity approximation made when solving the optical Bloch equations is not valid for $\frac{1}{2}mv^2 \leq U_{\text{lat}}$. To obtain a better quantitative agreement, a more advanced theoretical study would be required [216].

Appendix C: Sisyphus Optical Lattice Accelerator

The SOLD deceleration scheme brings atoms ultimately to zero mean velocity in the reference frame of the lattice. By applying a small frequency difference between two lattice beams, a lattice will move at a well-controlled velocity. This implies that the SOLD can ideally decelerate or accelerate atoms to any desired velocity. We test this using a 1.53(2) µK stationary cloud produced by loading a MOT into a dipole trap, at the location of the lattice. We shine both lattice and excitation light onto this cloud for 100 µs, and after 20 ms observe the number of atoms in a displaced cloud corresponding to the moving lattice frame. The results are shown in Fig. 4.10. We observe an increase in the displaced fraction with lattice
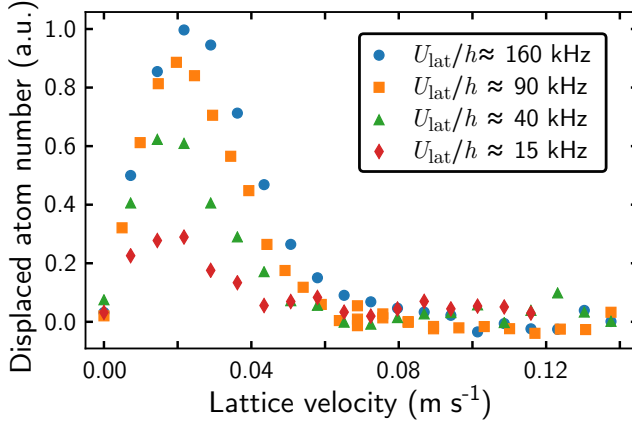
FIG. 4.10: Acceleration of a stationary strontium cloud by a moving lattice, for various lattice heights. The abscissa gives the lattice velocity and the ordinate, in arbitrary units, is proportional to the fraction of atoms in the moving frame measured after 100 μs of acceleration followed by 20 ms of evolution.

height, which we attribute to the increase in energy $\sim U_{\text{lat}}/2$ given to the atoms for each scattering event. We also observe an optimal lattice velocity for a given lattice height, which roughly corresponds to our model criterion of Eq. (4.3) with $m = 1$. The variation in the location of these efficiency peaks is more visible in Fig. 4.10 than in Fig. 4.3, because here the SOLD is pulsed for a short duration instead of operating in the steady-state regime, so the effects of each resonance corresponding to Eq. (4.3) are more pronounced. Note that due to the initial size of the cloud and its location with respect to the lattice, our estimation of the effective lattice depth is much rougher than for the data of Fig. 4.3.

Chapter 5

Outlook: Towards a steady-state atom laser

The main scientific goal of the experiment is to produce a steady-state atom laser. To do so, two critical steps need to be realized. First a steady-state BEC needs to be produced, then a continuous outcoupling scheme needs to be implemented (see chapter 1). During this thesis we succeeded in producing a steady-state BEC, see chapter 2. To produce a steady-state atom laser the final step is to devise a continuous outcoupling scheme compatible with our experimental architecture.

To outcouple the BEC, a small fraction of the condensate needs to be coherently and irreversibly transferred to an untrapped state without disturbing the rest of the condensate. Over the years different outcoupling schemes have been demonstrated, the majority of them involved transferring atoms in a magnetic trap from a trapped to an untrapped state. This transfer can be direct using RF radiation (RF outcoupling [25]), or via a virtual state (Raman outcoupling [24, 217]) . Because the ground-state of ^{84}Sr is non-magnetic and we trap our atoms using IR lasers these schemes cannot be implemented in our system. Additionally, atoms can be outcoupled in a quasi-continuous way by spilling them from optical [218] or magnetic traps [219]. Unfortunately, these schemes also cannot be extended to a fully steady-state system.

It has been suggested to use Bragg scattering [220] to outcouple BEC atoms from a dipole trap to produce an atom laser [44, 221]. The principle of Bragg scattering is shown in figure 5.1. Here momentum is imparted to the atoms via absorption and emission into two laser beams. The number of two-photon transfers, n, can be tuned by changing the relative frequency difference between the two laser beams, $\Delta\omega$, as $\Delta\omega = n\hbar k^2/2m$. Here $\hbar$ is the reduced Planck's constant, k is the wave-vector of the light and m is the particle's mass. The momentum imparted to the atoms of $2n\hbar k$ has to be sufficient to overcome the trap depth. In our experiment, confinement in the vertical direction is due to the reservoir
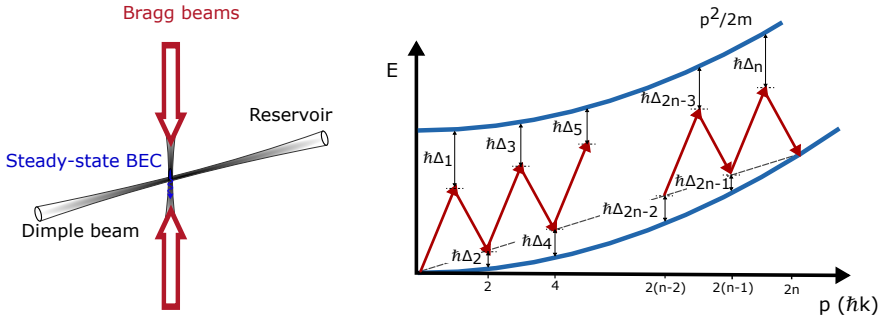
FIG. 5.1: Bragg outcoupling of a steady-state BEC. To the left: Sketch of the experimental architecture for the outcoupling scheme. To the right: Two counter-propagating beams with a relative frequency detuning impart a momentum of $2n\hbar k$.

trap. Its depth is $\sim 12\,\mu K$ so an induced momentum larger than $7\hbar k$ is required. Note that, momentum transfers larger than $7\hbar k$ have been reported [222–224], so outcoupling atoms from the trap is in principle possible.

This simple scheme might suffer from several limitations. First, because of the large detuning to the excited state, Bragg scattering is largely insensitive to the frequency of the addressed transition. Therefore atoms will continue to be addressed even when they leave the dipole trap. Atoms that leave the trap will change their velocity so other order multi-photon transitions might become resonant. Second, Bragg scattering does not change the internal state of the particle so atoms will be resonant to laser cooling light once they leave the trap, likely destroying the atom laser. Therefore along the path of the atom laser the laser cooling transition must be shifted out of resonance. The transition can be shifted, for example, by using a transparency beam (see section 2.2). However, implementing this solution without disturbing the rest of the experiment is technically challenging. Then, both thermal or BEC atoms will be outcoupled with roughly the same probability. In our system, where the BEC fraction is lower than 5 %, producing a pure atom laser necessarily requires addressing only BEC atoms. This problem is further exacerbated because this scheme does not provide any spatial selectivity. So atoms in the reservoir region will also be outcoupled. Finally, to our knowledge continuous outcoupling of a BEC using Bragg scattering has not been demonstrated, which is another concern.

To overcome these limitations we opted for an alternative approach, outcoupling atoms through the long-lived $^3P_0$ state. Our proposed scheme is shown in figure 5.2. This scheme is similar to previously demonstrated Raman output couplers and follows closely a theoretical proposal by Barker et al. [225]. Here we use a three-photon transfer of the atoms to the
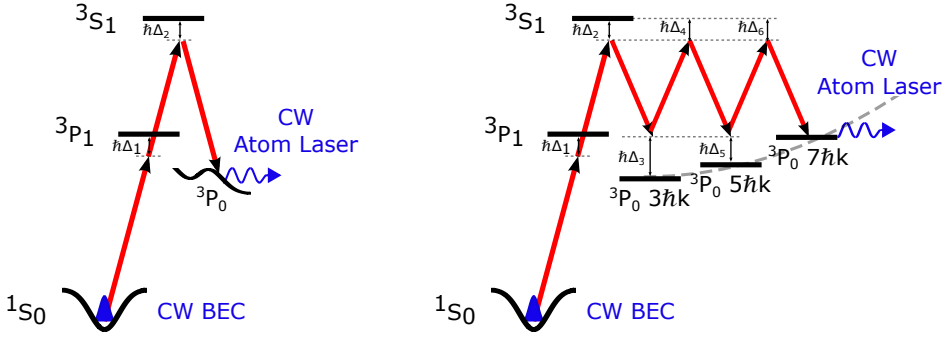
FIG. 5.2:   BEC outcoupling scheme. Here atoms are initially in the trapped
$^1S_0$ state and are transferred to the $^3P_0$ state using a multi-photon transition.
Left: using a blue-detuned laser from the $^3P_0 -^3 S_1$ transition, the $^3P_0$ state can
be rendered untrapped. Right: An additional Bragg-like four-photon transfer
can impart enough momentum for these atoms to leave the trap. The energy
differences in this diagram are not to scale.

$^3P_0$ state. To outcouple the $^3P_0$ atoms, an additional laser that is blue detuned from the
$^3P_0 - ^3S_1$ transition could create a repulsive that renders this state untrapped. Alternatively,
an additional 4 photon Bragg process (Right side of figure 5.2) could increase the velocity
of the atoms enough for them to leave the trap.

This scheme overcomes the previously mentioned limitations of the Bragg process. First,
as atoms leave the trap, they will become off-resonant due to the differential light-shift of
the $^1S_0 - ^3P_0$ transition. Second atoms populating the $^3P_0$ state will not be addressed by the
laser cooling light so no protection scheme will be required. Finally, the frequency of the
three-photon transfer can be tuned to spatially address atoms inside the trap. In addition if
the linewidth of the transfer is narrower than the difference between the chemical potential
of the BEC and the thermal cloud ($\sim 5\,\text{kHz}$), the BEC atoms can be selectively addressed,
producing a pure atom laser. Our scheme will be limited in the achievable atomic beam
density because of inelastic collisions between $^3P_0$ atoms, which have been shown to be
significant.

Another consideration is the achievable flux of the atom laser. The output flux will
be given by the Rabi frequency of the transfer Ω_{tr} and the number of addressed atoms N
as $\Phi \approx N \cdot \Omega_{\text{tr}}$. To avoid density fluctuations as well as other undesirable effects [226]
the atom laser must be operated in the weak-output coupling regime, which limits the
maximum Rabi frequency. Several criteria have been given in literature for this regime.
For us the most stringent of these, limits the Rabi frequency to be lower than the radial
trapping frequency ω_r. In our experiment $\omega_r = 2\pi \times 330\,\text{Hz}$. Assuming a Rabi frequency
of $\Omega_{\text{tr}} = 2\pi \times 100\,\text{Hz}$ and that we only address one-tenth of the atoms, the total atom

laser output flux will be of 4.6×10^5 atoms/s. Of course, it is an open question if we can produce a steady-state BEC with this additional loss mechanism. We have explored this question using the theoretical model presented in reference [37] and found that with slight improvements in the steady-state BEC scheme fluxes higher that 2×10^5 atoms/s are possible.

In the following, we briefly describe the laser system that we will use for the three-photon transfer. In a nutshell, we use two external cavity diode lasers (ECDLs) locked to an external cavity ($F \approx 1.3 \times 10^4$). These lasers are stabilized using the Pound–Drever–Hall technique [227]. The cavity length is stabilized to an external reference, the narrow-linewidth laser ($\approx 2\,\text{kHz}$) used to address the $7.5\,\text{kHz}$-wide $^1S_0 - {}^3P_1$ transition.[1] To stabilize the frequency of each ECDL we use two general-purpose digital PI controllers (*STEMlab 125-14*, AKA Red Pitaya). We chose these PID modules as a cost-effective solution.

As a preliminary characterization of the laser linewidth, we beat the output of a locked ECDL with the red narrow-linewidth laser. Here we tuned the ECDL's frequency to be similar to the frequency of the narrow-linewidth laser and we obtained a FWHM of around $\sim 15 - 20\,\text{kHz}$.

Several technical details concerning the STEMlab PI are critical to achieve this performance. These are documented with excellent detail by Preuschoff et al. [229] and will only be briefly mentioned here:

- It is critical to remove several resistors inside the Red Pitaya to suppress the noise of the output DAC [230].

- To further suppress the noise of the DAC it is key to attenuate the output of the PID as much as possible.

- Different PID actuators address different parts of the frequency spectrum to achieve optimal performance.

- The Red Pitaya is powered using a low noise power supply from a custom-made adapter board. This board also amplifies the error signal to match the input 1 V ADC of the Pitaya.

The $15\,\text{kHz}$ linewidth will not be narrow enough to provide selectivity between BEC and thermal atoms. Yet further improvements in performance might be possible with an upgraded PI scheme. The reported linewidth is narrow enough to provide spatial selectivity of atoms in the trap and it should be sufficient for a proof of principle demonstration of a CW atom laser.

---

[1] This laser was built before the author's arrival in the group. A description of it can be found in reference [228].

Bibliography

[1] A. Hees, J. Guéna, M. Abgrall, S. Bize, and P. Wolf. "Searching for an Oscillating Massive Scalar Field as a Dark Matter Candidate Using Atomic Hyperfine Frequency Comparisons", Phys. Rev. Lett. **117**, 061301, 2016 (cit. on p. 1).

[2] A. A. Geraci and A. Derevianko. "Sensitivity of Atom Interferometry to Ultralight Scalar Field Dark Matter", Phys. Rev. Lett. **117**, 261301, 2016 (cit. on p. 1).

[3] A. Derevianko and M. Pospelov. "Hunting for topological dark matter with atomic clocks", Nat. Phys. **10**, 933, 2014 (cit. on pp. 1, 6, 70).

[4] P. Wcisło, P. Morzyński, M. Bober, A. Cygan, D. Lisak, R. Ciuryło, and M. Zawada. "Experimental constraint on dark matter detection with optical atomic clocks", Nat. Astron. **1**, 9, 2016 (cit. on pp. 1, 6, 70, 102).

[5] B. Canuel et al. "Exploring gravity with the MIGA large scale atom interferometer", Sci. Rep. **8**, 14064, 2018 (cit. on pp. 1, 5, 38, 45).

[6] P. W. Graham, J. M. Hogan, M. A. Kasevich, and S. Rajendran. "New method for gravitational wave detection with atomic sensors", Phys. Rev. Lett. **110**, 171102, 2013 (cit. on pp. 1, 5, 37, 38, 45).

[7] S. Dimopoulos, P. W. Graham, J. M. Hogan, M. A. Kasevich, and S. Rajendran. "Atomic gravitational wave interferometric sensor", Phys. Rev. D **78**, 122002, 2008 (cit. on p. 1).

[8] N. Yu and M. Tinto. "Gravitational wave detection with single-laser atom interferometers", Gen. Relativ. Gravit. **43**, 1943, 2010 (cit. on pp. 1, 37, 38, 45).

[9] R. Bondarescu, A. Schärer, A. Lundgren, G. Hetényi, N. Houlié, P. Jetzer, and M. Bondarescu. "Ground-based optical atomic clocks as a tool to monitor vertical surface motion", Geophys. J. Int. **202**, 1770, 2015 (cit. on pp. 1, 6, 70).

[10] T. E. Mehlstäubler, G. Grosche, C. Lisdat, P. O. Schmidt, and H. Denker. "Atomic clocks for geodesy", Rep. Prog. Phys. **81**, 064401, 2018 (cit. on pp. 1, 6, 70).

[11] J. Grotti et al. "Geodesy and metrology with a transportable optical clock", Nat. Phys. **14**, 437, 2018 (cit. on pp. 1, 6, 38, 70).

[12] W. F. McGrew et al. "Atomic clock performance enabling geodesy below the centimetre level", Nature **564**, 87, 2018 (cit. on pp. 1, 6, 70).

[13] R. Geiger, A. Landragin, S. Merlet, and F. P. D. Santos. "High-accuracy inertial measurements with cold-atom sensors", AVS Quantum Science **2**, 024702, 2020 (cit. on pp. 1, 38).

[14] C. Jekeli. "Navigation Error Analysis of Atom Interferometer Inertial Sensor", Navigation **52**, 1, 2005 (cit. on p. 1).

[15] G. Santarelli, C. Audoin, A. Makdissi, P. Laurent, G. Dick, and A. Clairon. "Frequency stability degradation of an oscillator slaved to a periodically interrogated atomic resonator", IEEE Trans. Ultrason. Ferroelectr. Freq. Control. **45**, 887, 1998 (cit. on p. 1).

[16] M. Kasevich and S. Chu. "Atomic interferometry using stimulated Raman transitions", Phys. Rev. Lett. **67**, 181, 1991 (cit. on pp. 1, 4).

[17] A. D. Ludlow, M. M. Boyd, J. Ye, E. Peik, and P. O. Schmidt. "Optical atomic clocks", Rev. Mod. Phys. **87**, 637, 2015 (cit. on pp. 1, 6, 70, 71).

[18] G. J. Dick. "Local oscillator induced instabilities in trapped ion frequency standards", *Proc. Precise Time and Time Interval Meeting*. Ed. by Sydnow, R.L. US Naval Observatory, Redondo Beach California, 1987 (cit. on pp. 1, 5, 70).

[19] A. Quessada, R. P. Kovacich, I. Courtillot, A. Clairon, G. Santarelli, and P. Lemonde. "The Dick effect for an optical frequency standard", J. Opt. B: Quantum Semiclass. Opt. **5**, S150, 2003 (cit. on pp. 1, 70).

[20] J. Chen. "Active optical clock", Chin. Sci. Bull. **54**, 348, 2009 (cit. on pp. 1, 6, 37, 70).

[21] D. Meiser, J. Ye, D. R. Carlson, and M. J. Holland. "Prospects for a Millihertz-Linewidth Laser", Phys. Rev. Lett. **102**, 163601, 2009 (cit. on pp. 1, 6, 37, 70).

[22] N. Robins, P. Altin, J. Debs, and J. Close. "Atom lasers: Production, properties and prospects for precision inertial measurement", Phys. Rep. **529**, 265, 2013 (cit. on pp. 2, 5, 44).

[23] M.-O. Mewes, M. R. Andrews, D. M. Kurn, D. S. Durfee, C. G. Townsend, and W. Ketterle. "Output coupler for Bose-Einstein condensed atoms", Phys. Rev. Lett. **78**, 582, 1997 (cit. on p. 2).

[24] E. W. Hagley, L. Deng, M. Kozuma, J. Wen, K. Helmerson, S. L. Rolston, and W. D. Phillips. "A Well-Collimated Quasi-Continuous Atom Laser", Science **283**, 1706, 1999 (cit. on pp. 2, 120).

[25] I. Bloch, T. W. Hänsch, and T. Esslinger. "Atom Laser with a cw Output Coupler", Phys. Rev. Lett. **82**, 3008, 1999 (cit. on pp. 2, 120).

[26] Y. Castin, J. I. Cirac, and M. Lewenstein. "Reabsorption of light by trapped atoms", Phys. Rev. Lett. **80**, 5305, 1998 (cit. on pp. 2, 38).

[27] S. Stellmer, B. Pasquiou, R. Grimm, and F. Schreck. "Laser cooling to quantum degeneracy", Phys. Rev. Lett. **110**, 263003, 2013 (cit. on pp. 2, 11, 13, 16, 17, 18, 20, 21, 38, 40, 41, 61, 62, 72).

[28] A. Urvoy, Z. Vendeiro, J. Ramette, A. Adiyatullin, and V. Vuletić. "Direct laser cooling to Bose-Einstein condensation in a dipole trap", Phys. Rev. Lett. **122**, 203202, 2019 (cit. on pp. 2, 38, 44).

[29] J. Hu, A. Urvoy, Z. Vendeiro, V. Crépel, W. Chen, and V. Vuletić. "Creation of a Bose-condensed gas of ^{87}Rb by laser cooling", Science **358**, 1078, 2017 (cit. on p. 2).

[30] J. Grunert and A. Hemmerich. "Sub-Doppler magneto-optical trap for calcium", Phys. Rev. A **65**, 041401, 2002 (cit. on pp. 3, 4).

[31] T. Lahaye, Z. Wang, G. Reinaudi, S. P. Rath, J. Dalibard, and D. Guéry-Odelin. "Evaporative cooling of a guided rubidium atomic beam", Phys. Rev. A **72**, 033411, 2005 (cit. on pp. 3, 38, 44).

[32] S. E. Olson, R. R. Mhaskar, and G. Raithel. "Continuous propagation and energy filtering of a cold atomic beam in a long high-gradient magnetic atom guide", Phys. Rev. A **73**, 033622, 2006 (cit. on p. 3).

[33] M. Falkenau, V. V. Volchkov, J. Rührig, A. Griesmaier, and T. Pfau. "Continuous Loading of a Conservative Potential Trap from an Atomic Beam", Phys. Rev. Lett. **106**, 163002, 2011 (cit. on pp. 3, 4).

[34] V. V. Volchkov, J. Rührig, T. Pfau, and A. Griesmaier. "Sisyphus cooling in a continuously loaded trap", New J. Phys. **15**, 093012, 2013 (cit. on pp. 3, 4, 37, 38).

[35] S. Bennetts, C.-C. Chen, B. Pasquiou, and F. Schreck. "Steady-State Magneto-Optical Trap with 100-Fold Improved Phase-Space Density", Phys. Rev. Lett. **119**, 223202, 2017 (cit. on pp. 3, 4, 5, 10, 31, 37, 38, 40, 46, 67, 70, 71, 72, 74, 75, 85, 104, 111).

[36] C.-C. Chen, S. Bennetts, R. G. Escudero, B. Pasquiou, and F. Schreck. "Continuous guided strontium beam with high phase-space density", Phys. Rev. Appl **12**, 044014, 2019 (cit. on pp. 3, 5, 10, 11, 14, 15, 16, 31, 35, 38, 40, 46, 48, 70, 104, 137).

[37] C.-C. Chen, R. González Escudero, J. Minář, B. Pasquiou, S. Bennetts, and F. Schreck. "Continuous Bose-Einstein condensation", arxiv:2012.07605, 2020 (cit. on pp. 3, 4, 5, 11, 13, 20, 31, 33, 37, 72, 100, 123, 137).

[38] A. Frisch, K. Aikawa, M. Mark, A. Rietzler, J. Schindler, E. Zupani, R. Grimm, and F. Ferlaino. "Narrow-line magneto-optical trap for erbium", Phys. Rev. A **85**, 051401, 2012 (cit. on pp. 4, 87).

[39] T. Kuwamoto, K. Honda, Y. Takahashi, and T. Yabuzaki. "Magneto-optical trapping of Yb atoms using an intercombination transition", Phys. Rev. A **60**, R745, 1999 (cit. on p. 4).

[40] B. T. Seaman, M. Krämer, D. Z. Anderson, and M. J. Holland. "Atomtronics: Ultracold-atom analogs of electronic devices", Phys. Rev. A **75**, 023615, 2007 (cit. on p. 4).

[41] R. A. Pepino, J. Cooper, D. Z. Anderson, and M. J. Holland. "Atomtronic Circuits of Diodes and Transistors", Phys. Rev. Lett. **103**, 140405, 2009 (cit. on p. 4).

[42] C.-C. Chien, S. Peotta, and M. Di Ventra. "Quantum transport in ultracold atoms", Nat. Phys. **11**, 998, 2015 (cit. on p. 4).

[43] L. Amico et al. "Roadmap on Atomtronics: State of the art and perspective", arxiv:2008.04439, 2020 (cit. on p. 4).

[44] S. Bennetts. "1000 times closer to a continuous atom laser: Steady-state strontium with unity phase-space density". PhD thesis, University of Amsterdam, 2019 (cit. on pp. 4, 8, 10, 20, 31, 120).

[45] A. D. Cronin, J. Schmiedmayer, and D. E. Pritchard. "Optics and interferometry with atoms and molecules", Rev. Mod. Phys. **81**, 1051, 2009 (cit. on pp. 4, 37).

[46] C. Jönsson. "Electron Diffraction at Multiple Slits", Am. J. Phys. **42**, 4, 1974 (cit. on p. 5).

[47] H. Rauch and S. A. Werner. "Neutron Interferometry 2nd Edn", Oxford University Press, 2015 (cit. on p. 5).

[48] A. Shayeghi, P. Rieser, G. Richter, U. Sezer, J. H. Rodewald, P. Geyer, T. J. Martinez, and M. Arndt. "Matter-wave interference of a native polypeptide", Nat Commun **11**, 1447, 2020 (cit. on p. 5).

[49] L. Hackermüller, S. Uttenthaler, K. Hornberger, E. Reiger, B. Brezger, A. Zeilinger, and M. Arndt. "Wave Nature of Biomolecules and Fluorofullerenes", Phys. Rev. Lett. **91**, 090408, 2003 (cit. on p. 5).

[50] S. Gerlich, S. Eibenberger, M. Tomandl, S. Nimmrichter, K. Hornberger, P. J. Fagan, J. Tüxen, M. Mayor, and M. Arndt. "Quantum interference of large organic molecules", Nat Commun **2**, 263, 2011 (cit. on p. 5).

[51] K. S. Hardman, P. J. Everitt, G. D. McDonald, P. Manju, P. B. Wigley, M. A. Sooriyabandara, C. C. N. Kuhn, J. E. Debs, J. D. Close, and N. P. Robins. "Simultaneous Precision Gravimetry and Magnetic Gradiometry with a Bose-Einstein Condensate: A High Precision, Quantum Sensor", Phys. Rev. Lett. **117**, 138501, 2016 (cit. on p. 5).

[52] Z.-K. Hu, B.-L. Sun, X.-C. Duan, M.-K. Zhou, L.-L. Chen, S. Zhan, Q.-Z. Zhang, and J. Luo. "Demonstration of an ultrahigh-sensitivity atom-interferometry absolute gravimeter", Phys. Rev. A **88**, 043610, 2013 (cit. on p. 5).

[53] D. Savoie, M. Altorio, B. Fang, L. A. Sidorenkov, R. Geiger, and A. Landragin. "Interleaved atom interferometry for high-sensitivity inertial measurements", Sci. Adv. **4**, eaau7948, 2018 (cit. on pp. 5, 70).

[54] Y. Bidel, O. Carraz, R. Charrière, M. Cadoret, N. Zahzam, and A. Bresson. "Compact cold atom gravimeter for field applications", Appl. Phys. Lett. **102**, 144107, 2013 (cit. on p. 5).

[55] Q. Wang, Y.-G. Lin, F. Meng, Y. Li, B.-K. Lin, E.-J. Zang, T.-C. Li, and Z.-J. Fang. "Magic Wavelength Measurement of the ^{87}Sr Optical Lattice Clock at NIM", Chin. Phys. Lett. **33**, 103201, 2016 (cit. on p. 5).

[56] J. M. Hogan et al. "An atomic gravitational wave interferometric sensor in low earth orbit (AGIS-LEO)", Gen. Rel. Gravit. **43**, 1953, 2011 (cit. on p. 5).

[57] A. Arvanitaki, P. W. Graham, J. M. Hogan, S. Rajendran, and K. V. Tilburg. "Search for light scalar dark matter with atomic gravitational wave detectors", Phys. Rev. D **97**, 075020, 2018 (cit. on p. 5).

[58] M. G. Tarallo, T. Mazzoni, N. Poli, D. V. Sutyrin, X. Zhang, and G. M. Tino. "Test of Einstein Equivalence Principle for 0-Spin and Half-Integer-Spin Atoms: Search for Spin-Gravity Coupling Effects", Phys. Rev. Lett. **113**, 023005, 2014 (cit. on p. 5).

[59] S. Fray, C. A. Diez, T. W. Hänsch, and M. Weitz. "Atomic Interferometer with Amplitude Gratings of Light and Its Applications to Atom Based Tests of the Equivalence Principle", Phys. Rev. Lett. **93**, 240404, 2004 (cit. on p. 5).

[60] H. C. Lefèvre. "The fiber-optic gyroscope, a century after Sagnac's experiment: The ultimate rotation-sensing technology?", C. R. Phys. **15**, 851, 2014 (cit. on p. 5).

[61] iXblue. "Fiber optic gyroscopes technology". URL: https://www.ixblue.com/fiber-optic-gyroscopes-technology (cit. on p. 5).

[62] I. Dutta, D. Savoie, B. Fang, B. Venon, C. G. Alzar, R. Geiger, and A. Landragin. "Continuous Cold-Atom Inertial Sensor with 1 nrad/sec Rotation Stability", Phys. Rev. Lett. **116**, 183003, 2016 (cit. on p. 5).

[63] K. Bongs, M. Holynski, J. Vovrosh, P. Bouyer, G. Condon, E. Rasel, C. Schubert, W. P. Schleich, and A. Roura. "Taking atom interferometric quantum sensors from the laboratory to real-world applications", Nat. Rev. Phys. **1**, 731, 2019 (cit. on pp. 5, 37).

[64] P. Westergaard, J. Lodewyck, and P. Lemonde. "Minimizing the Dick effect in an optical lattice clock", IEEE Trans. Ultrason. Ferroelectr. Freq. Control **57**, 623, 2010 (cit. on pp. 5, 70).

[65] P. Cheiney, L. Fouché, S. Templier, F. Napolitano, B. Battelier, P. Bouyer, and B. Barrett. "Navigation-Compatible Hybrid Quantum Accelerometer Using a Kalman Filter", Phys. Rev. Appl **10**, 034030, 2018 (cit. on p. 5).

[66] A. Trimeche, M. Langlois, S. Merlet, and F. Pereira Dos Santos. "Active Control of Laser Wavefronts in Atom Interferometers", Phys. Rev. Applied **7**, 034016, 2017 (cit. on p. 5).

[67] T. Hensel, S. Loriani, C. Schubert, F. Fitzek, S. Abend, H. Ahlers, J.-N. Siemß, K. Hammerer, E. M. Rasel, and N. Gaaloul. "Inertial sensing with quantum gases: a comparative performance study of condensed versus thermal sources for atom interferometry", Eur. Phys. J. D **75**, 108, 2021 (cit. on p. 5).

[68] A. Gauguet, B. Canuel, T. Lévèque, W. Chaibi, and A. Landragin. "Characterization and limits of a cold-atom Sagnac interferometer", Phys. Rev. A **80**, 063604, 2009 (cit. on p. 5).

[69] W.-J. Xu et al. "Effects of wave-front tilt and air density fluctuations in a sensitive atom interferometry gyroscope", Opt. Express **28**, 12189, 2020 (cit. on p. 5).

[70] S.-Y. Lan, P.-C. Kuan, B. Estey, P. Haslinger, and H. Müller. "Influence of the Coriolis Force in Atom Interferometry", Phys. Rev. Lett. **108**, 090402, 2012 (cit. on p. 5).

[71] T. L. Nicholson et al. "Systematic evaluation of an atomic clock at 2×10^{-18} total uncertainty", Nat. Commun. **6**, 6896, 2015 (cit. on pp. 6, 72, 115).

[72] S. L. Campbell et al. "A Fermi-degenerate three-dimensional optical lattice clock", Science **358**, 90, 2017 (cit. on p. 6).

[73] P. Wcisło et al. "New bounds on dark matter coupling from a global network of optical atomic clocks", Sci. Adv. **4**, eaau4869, 2018 (cit. on pp. 6, 70, 102).

[74] C. J. A. P. Martins. "The status of varying constants: a review of the physics, searches and implications", Rep. Prog. Phys. **80**, 126902, 2017 (cit. on pp. 6, 70, 102).

[75] S. Blatt et al. "New limits on coupling of fundamental constants to gravity using ^{87}Sr optical lattice clocks", Phys. Rev. Lett. **100**, 140801, 2008 (cit. on pp. 6, 70).

[76] R. M. Godun, P. B. R. Nisbet-Jones, J. M. Jones, S. A. King, L. A. M. Johnson, H. S. Margolis, K. Szymaniec, S. N. Lea, K. Bongs, and P. Gill. "Frequency Ratio of Two Optical Clock Transitions in ^{171}Yb^{+} and Constraints on the Time Variation of Fundamental Constants", Phys. Rev. Lett. **113**, 210801, 2014 (cit. on pp. 6, 70, 102).

[77] T. Kessler, C. Hagemann, C. Grebing, T. Legero, U. Sterr, F. Riehle, M. J. Martin, L. Chen, and J. Ye. "A sub-40-mHz-linewidth laser based on a silicon single-crystal optical cavity", Nat. Photonics **6**, 687, 2012 (cit. on p. 6).

[78] D. G. Matei et al. "1.5 μm Lasers with Sub-10 mHz Linewidth", Phys. Rev. Lett. **118**, 263202, 2017 (cit. on p. 6).

[79] S. Häfner, S. Falke, C. Grebing, S. Vogt, T. Legero, M. Merimaa, C. Lisdat, and U. Sterr. "8 × 10^{-17} fractional laser frequency instability with a long room-temperature cavity", Opt. Lett. **40**, 2112, 2015 (cit. on p. 6).

[80] G. D. Cole, W. Zhang, M. J. Martin, J. Ye, and M. Aspelmeyer. "Tenfold reduction of Brownian noise in high-reflectivity optical coatings", Nat. Photonics **7**, 644, 2013 (cit. on p. 6).

[81] M. A. Norcia, M. N. Winchester, J. R. K. Cline, and J. K. Thompson. "Superradiance on the millihertz linewidth strontium clock transition", Sci. Adv. **2**, e1601231, 2016 (cit. on pp. 6, 7, 70, 71, 72, 87).

[82] M. A. Norcia and J. K. Thompson. "Cold-Strontium Laser in the Superradiant Crossover Regime", Phys. Rev. X **6**, 011025, 2016 (cit. on p. 7).

[83] "The iqClock Quantum Flagship consortium." https://www.iqclock.eu (cit. on pp. 7, 8, 70).

[84] "Ultra-stable superradiant laser based on ytterbium atoms". https://teams.femto-st.fr/equipe-ohms/yb-superradiant-laser/ (cit. on pp. 7, 70).

[85] J. A. Sauer, K. M. Fortier, M. S. Chang, C. D. Hamley, and M. S. Chapman. "Cavity QED with optically transported atoms", Phys. Rev. A **69**, 051804, 2004 (cit. on pp. 7, 88).

[86] J. Samland. "A 448nm repump for Strontium". MA thesis. University of Amsterdam, The Netherlands, 2019 (cit. on pp. 7, 8, 10).

[87] T. P. Dinneen, K. R. Vogel, E. Arimondo, J. L. Hall, and A. Gallagher. "Cold collisions of Sr$^{*}-$Sr in a magneto-optical trap", Phys. Rev. A **59**, 1216, 1999 (cit. on pp. 7, 36, 88, 112).

[88] T. van Leent. "Narrow-linewidth ECDLs for Atomic Physics". MA thesis. University of Amsterdam, 2017 (cit. on pp. 8, 10).

[89] C.-C. Chen. "An atomic marble run to unity phase-space density". PhD thesis, University of Amsterdam, 2019 (cit. on pp. 8, 10, 20, 31).

[90] R. González Escudero, C.-C. Chen, S. Bennetts, B. Pasquiou, and F. Schreck. "Steady-state magneto-optical trap of fermionic strontium on a narrow-line transition", Phys. Rev. Research **3**, 033159, 2021 (cit. on pp. 8, 67, 68, 69, 89, 92, 137).

[91] S. Wu, R. C. Brown, W. D. Phillips, and J. V. Porto. "Pulsed Sisyphus Scheme for Laser Cooling of Atomic (Anti)Hydrogen", Phys. Rev. Lett. **106**, 213001, 2011 (cit. on pp. 8, 100, 102, 105, 107, 112, 113).

[92] B. L. Augenbraun, J. M. Doyle, T. Zelevinsky, and I. Kozyryev. "Molecular Asymmetry and Optical Cycling: Laser Cooling Asymmetric Top Molecules", Phys. Rev. X **10**, 031022, 2020 (cit. on p. 9).

[93] C.-C. Chen, S. Bennetts, R. G. Escudero, F. Schreck, and B. Pasquiou. "Sisyphus optical lattice decelerator", Phys. Rev. A **100**, 023401, 2019 (cit. on pp. 10, 101, 137).

[94] S. Stellmer. "Degenerate quantum gases of strontium". PhD thesis, University of Innsbruck, 2013 (cit. on p. 13).

[95] W. Ketterle, K. B. Davis, M. A. Joffe, A. Martin, and D. E. Pritchard. "High densities of cold atoms in a dark spontaneous-force optical trap", Phys. Rev. Lett. **70**, 2253, 1993 (cit. on p. 15).

[96] D. M. Stamper-Kurn, H.-J. Miesner, A. P. Chikkatur, S. Inouye, J. Stenger, and W. Ketterle. "Reversible Formation of a Bose-Einstein Condensate", Phys. Rev. Lett. **81**, 2194, 1998 (cit. on pp. 17, 41).

[97] S. Stellmer, M. K. Tey, B. Huang, R. Grimm, and F. Schreck. "Bose-Einstein Condensation of Strontium", Phys. Rev. Lett. **103**, 200401, 2009 (cit. on p. 20).

[98] M. S. Safronova, Z. Zuhrianda, U. I. Safronova, and C. W. Clark. "The magic road to precision". 2015, arXiv:1507.06570, (cit. on p. 29).

[99] J. Samland. "Pumping the Zeeman slower". MA thesis. University of Amsterdam, 2019 (cit. on pp. 31, 36).

[100] F. Dalfovo, S. Giorgini, L. P. Pitaevskii, and S. Stringari. "Theory of Bose-Einstein condensation in trapped gases", Rev. Mod. Phys. **71**, 463, 1999 (cit. on p. 32).

[101] V. Schkolnik, J. R. Williams, and N. Yu. "Generating 500 mW for laser cooling of strontium atoms by injection locking a high power laser diode", arxiv:2004.11732, 2020 (cit. on pp. 36, 71).

[102] I. Bloch, J. Dalibard, and S. Nascimbène. "Quantum simulations with ultracold quantum gases", Nat. Phys. **8**, 267, 2012 (cit. on p. 37).

[103] M. D. Lachmann et al. "Ultracold atom interferometry in space", Nat. Commun. **12**, 1317, 2021 (cit. on p. 37).

[104] D. N. Aguilera et al. "STE-QUEST — test of the universality of free fall using cold atom interferometry", Class. Quantum Gravity **31**, 115010, 2014 (cit. on pp. 37, 38).

[105] J. Hartwig, S. Abend, C. Schubert, D. Schlippert, H. Ahlers, K. Posso-Trujillo, N. Gaaloul, W. Ertmer, and E. M. Rasel. "Testing the universality of free fall with rubidium and ytterbium in a very large baseline atom interferometer", New J. Phys. **17**, 035011, 2015 (cit. on pp. 37, 38).

[106] H. M. Wiseman. "Light amplification without stimulated emission: Beyond the standard quantum limit to the laser linewidth", Phys. Rev. A **60**, 4083, 1999 (cit. on p. 37).

[107] T. J. Baker, S. N. Saadatmand, D. W. Berry, and H. M. Wiseman. "The Heisenberg limit for laser coherence", Nat. Phys. **17**, 179, 2020 (cit. on pp. 37, 44).

[108] C. Liu, M. Mucci, X. Cao, M. V. G. Dutt, M. Hatridge, and D. Pekker. "A new quantum limit on laser linewidth", arxiv:2009.03333, 2020 (cit. on p. 37).

[109] C. Lisdat et al. "A clock network for geodesy and fundamental science", Nat Commun **7**, 12443, 2016 (cit. on p. 38).

[110] P. Adamson et al. "PROPOSAL: p-1101 matter-wave atomic gradiometer interferometric sensor (MAGIS-100)", Office of Scientific and Technical Information (OSTI) 2018 (cit. on pp. 38, 45).

[111]   L. Badurina et al. "AION: an atom interferometer observatory and network", J. Cosmol. Astropart. Phys. **2020**, 011, 2020 (cit. on pp. 38, 45).

[112]   M. S. Safronova, D. Budker, D. DeMille, D. F. J. Kimball, A. Derevianko, and C. W. Clark. "Search for new physics with atoms and molecules", Rev. Mod. Phys. **90**, 025008, 2018 (cit. on pp. 38, 102).

[113]   M. S. Safronova. "The search for variation of fundamental constants with clocks", Ann. Phys. (Berl.) **531**, 1800364, 2019 (cit. on p. 38).

[114]   S. Bhongale and M. Holland. "Loading a continuous-wave atom laser by optical pumping techniques", Phys. Rev. A **62**, 043604, 2000 (cit. on p. 38).

[115]   A. P. Chikkatur, Y. Shin, A. E. Leanhardt, D. Kielpinski, E. Tsikata, T. L. Gustavson, D. E. Pritchard, and W. Ketterle. "A Continuous Source of Bose-Einstein Condensed Atoms", Science **296**, 2193, 2002 (cit. on p. 38).

[116]   H.-J. Miesner, D. M. Stamper-Kurn, M. R. Andrews, D. S. Durfee, S. Inouye, and W. Ketterle. "Bosonic stimulation in the formation of a Bose-Einstein condensate", Science **279**, 1005, 1998 (cit. on pp. 38, 41, 58).

[117]   N. P. Robins, C. Figl, M. Jeppesen, G. R. Dennis, and J. D. Close. "A pumped atom laser", Nat. Phys. **4**, 731, 2008 (cit. on pp. 38, 44).

[118]   L. Deng, E. W. Hagley, J. Wen, M. Trippenbach, Y. Band, P. S. Julienne, J. E. Simsarian, K. Helmerson, S. L. Rolston, and W. D. Phillips. "Four-wave mixing with matter waves", Nature **398**, 218, 1999 (cit. on p. 38).

[119]   S. Inouye, T. Pfau, S. Gupta, A. P. Chikkatur, A. Görlitz, D. E. Pritchard, and W. Ketterle. "Phase-coherent amplification of atomic matter waves", Nature **402**, 641, 1999 (cit. on pp. 38, 58).

[120]   D. Schneble, Y. Torii, M. Boyd, E. W. Streed, D. E. Pritchard, and W. Ketterle. "The onset of matter-wave amplification in a superradiant Bose-Einstein condensate", Science **300**, 475, 2003 (cit. on p. 38).

[121]   J. Williams, R. Walser, C. Wieman, J. Cooper, and M. Holland. "Achieving steady-state Bose-Einstein condensation", Phys. Rev. A **57**, 2030, 1998 (cit. on p. 38).

[122]   J. I. Cirac, M. Lewenstein, and P. Zoller. "Collective laser cooling of trapped atoms", EPL **35**, 647, 1996 (cit. on p. 38).

[123]   G. R. Dennis, M. J. Davis, and J. J. Hope. "Quantum kinetic theory model of a continuous atom laser", Phys. Rev. A **86**, 013640, 2012 (cit. on pp. 40, 44).

[124]   P. W. H. Pinkse, A. Mosk, M. Weidemüller, M. W. Reynolds, T. W. Hijmans, and J. T. M. Walraven. "Adiabatically changing the phase-space density of a trapped Bose gas", Phys. Rev. Lett. **78**, 990, 1997 (cit. on p. 41).

[125]   S. Dutta and E. J. Mueller. "Kinetics of Bose-Einstein condensation in a dimple potential", Phys. Rev. A **91**, 013601, 2015 (cit. on pp. 41, 60).

[126]   S. A. Haine, J. J. Hope, N. P. Robins, and C. M. Savage. "Stability of continuously pumped atom lasers", Phys. Rev. Lett. **88**, 170403, 2002 (cit. on p. 44).

[127]   L. M. Sieberer, S. D. Huber, E. Altman, and S. Diehl. "Dynamical critical phenomena in driven-dissipative systems", Phys. Rev. Lett. **110**, 195301, 2013 (cit. on p. 44).

[128]   L. He, L. M. Sieberer, and S. Diehl. "Space-time vortex driven crossover and vortex turbulence phase transition in one-dimensional driven open condensates", Phys. Rev. Lett. **118**, 085301, 2017 (cit. on p. 44).

[129] S. S. Szigeti, M. R. Hush, A. R. R. Carvalho, and J. J. Hope. "Feedback control of an interacting Bose-Einstein condensate using phase-contrast imaging", Phys. Rev. A **82**, 043632, 2010 (cit. on p. 44).

[130] M. A. Kristensen, M. B. Christensen, M. Gajdacz, M. Iglicki, K. Pawłowski, C. Klempt, J. F. Sherson, K. Rzążewski, A. J. Hilliard, and J. J. Arlt. "Observation of atom number fluctuations in a Bose-Einstein condensate", Phys. Rev. Lett. **122**, 163601, 2019 (cit. on p. 44).

[131] M. T. Johnsson and S. A. Haine. "Generating quadrature squeezing in an atom laser through self-interaction", Phys. Rev. Lett. **99**, 010401, 2007 (cit. on p. 44).

[132] K. Beloy et al. "Frequency ratio measurements at 18-digit accuracy using an optical clock network", Nature **591**, 564, 2021 (cit. on p. 44).

[133] G. M. Tino et al. "SAGE: A proposal for a space atomic gravity explorer", Eur. Phys. J. D **73**, 228, 2019 (cit. on p. 45).

[134] Y. Castin and R. Dum. "Bose-Einstein condensates in time dependent traps", Phys. Rev. Lett. **77**, 5315, 1996 (cit. on pp. 57, 58).

[135] C. J. Bordé. "Amplification of atomic fields by stimulated emission of atoms", Phys. Lett. A **204**, 217, 1995 (cit. on p. 58).

[136] M. Kozuma, Y. Suzuki, Y. Torii, T. Sugiura, T. Kuga, E. W. Hagley, and L. Deng. "Phase-coherent amplification of matter waves", Science **286**, 2309, 1999 (cit. on p. 58).

[137] B. Jackson and E. Zaremba. "Modeling Bose-Einstein condensed gases at finite temperatures with N-body simulations", Phys. Rev. A **66**, 033606, 2002 (cit. on pp. 60, 62, 66).

[138] O. J. Luiten, M. W. Reynolds, and J. T. M. Walraven. "Kinetic theory of the evaporative cooling of a trapped gas", Phys. Rev. A **53**, 381, 1996 (cit. on p. 61).

[139] C. W. Gardiner, M. D. Lee, R. J. Ballagh, M. J. Davis, and P. Zoller. "Quantum kinetic theory of condensate growth: Comparison of experiment and theory", Phys. Rev. Lett. **81**, 5266, 1998 (cit. on p. 61).

[140] M. Holland, J. Williams, and J. Cooper. "Bose-Einstein condensation: Kinetic evolution obtained from simulated trajectories", Phys. Rev. A **55**, 3670, 1997 (cit. on p. 61).

[141] R. B. Dingle. "The Fermi-Dirac integrals", Appl. Sci. Res. **6**, 225, 1957 (cit. on p. 62).

[142] Y. N. Martinez de Escobar. "Bose-Einstein condensation of ^{84}Sr". PhD thesis, Rice University, 2012 (cit. on p. 64).

[143] S. Stellmer, R. Grimm, and F. Schreck. "Production of quantum-degenerate strontium gases", Phys. Rev. A **87**, 013611, 2013 (cit. on p. 64).

[144] E. Zaremba, T. Nikuni, and A. Griffin. "Dynamics of trapped Bose gases at finite temperatures", J. Low Temp. Phys. **116**, 277, 1999 (cit. on p. 66).

[145] M. J. Bijlsma, E. Zaremba, and H. T. C. Stoof. "Condensate growth in trapped Bose gases", Phys. Rev. A **62**, 063609, 2000 (cit. on p. 66).

[146] A. V. Taichenachev, V. I. Yudin, C. W. Oates, C. W. Hoyt, Z. W. Barber, and L. Hollberg. "Magnetic Field-Induced Spectroscopy of Forbidden Optical Transitions with Application to Lattice-Based Optical Atomic Clocks", Phys. Rev. Lett. **96**, 083001, 2006 (cit. on pp. 67, 70).

[147] J. P. Bartolotta, M. A. Norcia, J. R. K. Cline, J. K. Thompson, and M. J. Holland. "Laser cooling by sawtooth-wave adiabatic passage", Phys. Rev. A **98**, 023404, 2018 (cit. on pp. 68, 74, 75, 77, 79).

[148] S. Kolkowitz, I. Pikovski, N. Langellier, M. D. Lukin, R. L. Walsworth, and J. Ye. "Gravitational wave detection with optical lattice atomic clocks", Phys. Rev. D **94**, 124043, 2016 (cit. on p. 70).

[149]   M. Takamoto, I. Ushijima, N. Ohmae, T. Yahagi, K. Kokado, H. Shinkai, and H. Katori. "Test of general relativity by a pair of transportable optical lattice clocks", Nat. Photonics **14**, 411, 2020 (cit. on p. 70).

[150]   C. W. Chou, D. B. Hume, T. Rosenband, and D. J. Wineland. "Optical clocks and relativity", Science **329**, 1630, 2010 (cit. on p. 70).

[151]   M. A. Norcia, A. W. Young, W. J. Eckner, E. Oelker, J. Ye, and A. M. Kaufman. "Seconds-scale coherence on an optical clock transition in a tweezer array", Science **366**, 93, 2019 (cit. on p. 70).

[152]   M. Takamoto, T. Takano, and H. Katori. "Frequency comparison of optical lattice clocks beyond the Dick limit", Nat. Photonics **5**, 288, 2011 (cit. on p. 70).

[153]   M. Schioppo et al. "Ultrastable optical clock with two cold-atom ensembles", Nat. Photonics **11**, 48, 2016 (cit. on p. 70).

[154]   D. Meiser and M. J. Holland. "Steady-state superradiance with alkaline-earth-metal atoms", Phys. Rev. A **81**, 033847, 2010 (cit. on pp. 70, 71, 87).

[155]   J. G. Bohnet, Z. Chen, J. M. Weiner, D. Meiser, M. J. Holland, and J. K. Thompson. "A steady-state superradiant laser with less than one intracavity photon", Nature **484**, 78, 2012 (cit. on pp. 70, 71, 87).

[156]   M. A. Norcia, J. R. Cline, J. A. Muniz, J. M. Robinson, R. B. Hutson, A. Goban, G. E. Marti, J. Ye, and J. K. Thompson. "Frequency measurements of superradiance from the strontium clock transition", Phys. Rev. X **8**, 021036, 2018 (cit. on p. 70).

[157]   J. A. Muniz, J. R. K. Cline, M. A. Norcia, and J. K. Thompson. "An active optical frequency reference using a pulsed superradiant laser", *Optical, Opto-Atomic, and Entanglement-Enhanced Precision Metrology*. Vol. 10934. SPIE, 2019 (cit. on p. 70).

[158]   S. Origlia et al. "Towards an optical clock for space: Compact, high-performance optical lattice clock based on bosonic atoms", Phys. Rev. A **98**, 053443, 2018 (cit. on p. 70).

[159]   M. T. Georgy Kazakov and S. A. Schäffer. "Progress report on relevant real-life effects - iqClock period 1 report ". https://cordis.europa.eu/project/id/820404/results. Online; accessed 11 March 2021. 2021 (cit. on p. 70).

[160]   M. M. Boyd. "High Precision Spectroscopy of Strontium in an Optical Lattice: Towards a New Standard for Frequency and Time". PhD thesis, University of Colorado, 2002 (cit. on p. 71).

[161]   B. Lu, Y. Wang, J. Han, S. Zhang, J. Li, and H. Chang. "Exploration of the magnetic-field-induced $5s5p^3P_0$-$5s2^1S_0$ forbidden transition in bosonic Sr atom", J. Phys. Commun. **1**, 055017, 2017 (cit. on p. 72).

[162]   M. A. Norcia, J. R. K. Cline, J. P. Bartolotta, M. J. Holland, and J. K. Thompson. "Narrow-line laser cooling by adiabatic transfer", New J. Phys. **20**, 023021, 2018 (cit. on pp. 72, 74, 75, 89, 102).

[163]   H. Katori, T. Ido, Y. Isoya, and M. Kuwata-Gonokami. "Magneto-Optical Trapping and Cooling of Strontium Atoms down to the Photon Recoil Temperature", Phys. Rev. Lett. **82**, 1116, 1999 (cit. on p. 72).

[164]   J. A. Muniz, M. A. Norcia, J. R. K. Cline, and J. K. Thompson. "A robust narrow-line magneto-optical trap using adiabatic transfer", arxiv:1806.00838v1, 2018 (cit. on p. 74).

[165]   S. Snigirev, A. J. Park, A. Heinz, I. Bloch, and S. Blatt. "Fast and dense magneto-optical traps for strontium", Phys. Rev. A **99**, 063421, 2019 (cit. on pp. 74, 83, 89).

[166]   N. Petersen, F. Mühlbauer, L. Bougas, A. Sharma, D. Budker, and P. Windpassinger. "Sawtooth-wave adiabatic-passage slowing of dysprosium", Phys. Rev. A **99**, 063414, 2019 (cit. on pp. 74, 77).

[167]   G. P. Greve, B. Wu, and J. K. Thompson. "Laser cooling with adiabatic transfer on a Raman transition", New J. Phys. **21**, 073045, 2019 (cit. on p. 74).

[168] C. Zener. "Non-adiabatic crossing of energy levels", Proc. Royal Soc. A **137**, 696, 1932 (cit. on p. 75).

[169] M. Zhu, C. W. Oates, and J. L. Hall. "Continuous high-flux monovelocity atomic beam based on a broadband laser-cooling technique", Phys. Rev. Lett. **67**, 46, 1991 (cit. on p. 81).

[170] J. R. de Laeter, J. K. Böhlke, P. D. Bièvre, H. Hidaka, H. S. Peiser, K. J. R. Rosman, and P. D. P. Taylor. "Atomic weights of the elements. Review 2000 (IUPAC Technical Report)", Pure Appl. Chem. **75**, 683, 2003 (cit. on p. 85).

[171] T. Mukaiyama, H. Katori, T. Ido, Y. Li, and M. Kuwata-Gonokami. "Recoil-Limited Laser Cooling of ^{87}Sr Atoms near the Fermi Temperature", Phys. Rev. Lett. **90**, 113002, 2003 (cit. on p. 86).

[172] D. Dreon, L. A. Sidorenkov, C. Bouazza, W. Maineult, J. Dalibard, and S. Nascimbene. "Optical cooling and trapping of highly magnetic atoms: the benefits of a spontaneous spin polarization", J. Phys. B: At., Mol. Opt. Phys. **50**, 065005, 2017 (cit. on p. 87).

[173] K. Aikawa, A. Frisch, M. Mark, S. Baier, A. Rietzler, R. Grimm, and F. Ferlaino. "Bose-Einstein Condensation of Erbium", Phys. Rev. Lett. **108**, 210401, 2012 (cit. on p. 87).

[174] R. G. Escudero. "Monte-Carlo Simulation". https://github.com/GWleibniz/Fermionic_MOT_Monte_Carlo. 2021 (cit. on pp. 92, 97).

[175] D. DeMille. "Diatomic molecules, a window onto fundamental physics", Phys. Today **68**, 34, 2015 (cit. on p. 102).

[176] J. J. Hudson, D. M. Kara, I. J. Smallman, B. E. Sauer, M. R. Tarbutt, and E. A. Hinds. "Improved measurement of the shape of the electron", Nature **473**, 493, 2011 (cit. on p. 102).

[177] J. Baron et al. "Order of Magnitude Smaller Limit on the Electric Dipole Moment of the Electron", Science **343**, 269, 2013 (cit. on p. 102).

[178] W. B. Cairncross, D. N. Gresh, M. Grau, K. C. Cossel, T. S. Roussy, Y. Ni, Y. Zhou, J. Ye, and E. A. Cornell. "Precision Measurement of the Electron's Electric Dipole Moment Using Trapped Molecular Ions", Phys. Rev. Lett. **119**, 153001, 2017 (cit. on p. 102).

[179] J.-P. Uzan. "The fundamental constants and their variation: observational and theoretical status", Rev. Mod. Phys. **75**, 403, 2003 (cit. on p. 102).

[180] J. F. Barry, D. J. McCarron, E. B. Norrgard, M. H. Steinecker, and D. DeMille. "Magneto-optical trapping of a diatomic molecule", Nature **512**, 286, 2014 (cit. on pp. 102, 103, 107, 113).

[181] L. Anderegg, B. L. Augenbraun, E. Chae, B. Hemmerling, N. R. Hutzler, A. Ravi, A. Collopy, J. Ye, W. Ketterle, and J. M. Doyle. "Radio Frequency Magneto-Optical Trapping of CaF with High Density", Phys. Rev. Lett. **119**, 103201, 2017 (cit. on pp. 102, 103, 107, 113).

[182] A. L. Collopy, S. Ding, Y. Wu, I. A. Finneran, L. Anderegg, B. L. Augenbraun, J. M. Doyle, and J. Ye. "3D Magneto-Optical Trap of Yttrium Monoxide", Phys. Rev. Lett. **121**, 213201, 2018 (cit. on pp. 102, 103, 107, 113).

[183] S. Truppe, H. J. Williams, M. Hambach, L. Caldwell, N. J. Fitch, E. A. Hinds, B. E. Sauer, and M. R. Tarbutt. "Molecules cooled below the Doppler limit", Nat. Phys. **13**, 1173, 2017 (cit. on pp. 102, 103, 107, 113).

[184] G. B. Andresen et al. "Trapped antihydrogen", Nature **468**, 673, 2010 (cit. on p. 102).

[185] G. Gabrielse et al. "Trapped Antihydrogen in Its Ground State", Phys. Rev. Lett. **108**, 113002, 2012 (cit. on p. 102).

[186] M. Ahmadi et al. "Observation of the 1S-2S transition in trapped antihydrogen", Nature **541**, 506, 2017 (cit. on p. 102).

[187] M. Ahmadi et al. "Observation of the hyperfine spectrum of antihydrogen", Nature **548**, 66, 2017 (cit. on p. 102).

[188] M. Ahmadi et al. "Observation of the 1S-2P Lyman-α transition in antihydrogen", Nature **561**, 211, 2018 (cit. on p. 102).

[189] N. Masuhara, J. M. Doyle, J. C. Sandberg, D. Kleppner, T. J. Greytak, H. F. Hess, and G. P. Kochanski. "Evaporative Cooling of Spin-Polarized Atomic Hydrogen", Phys. Rev. Lett. **61**, 935, 1988 (cit. on p. 102).

[190] G. Gabrielse et al. "Lyman-α source for laser cooling antihydrogen", Opt. Lett. **43**, 2905, 2018 (cit. on p. 102).

[191] K. S. E. Eikema, J. Walz, and T. W. Hänsch. "Continuous Coherent Lyman-α Excitation of Atomic Hydrogen", Phys. Rev. Lett. **86**, 5679, 2001 (cit. on p. 102).

[192] I. D. Setija, H. G. C. Werij, O. J. Luiten, M. W. Reynolds, T. W. Hijmans, and J. T. M. Walraven. "Optical cooling of atomic hydrogen in a magnetic trap", Phys. Rev. Lett. **70**, 2257, 1993 (cit. on p. 102).

[193] P. H. Donnan, M. C. Fujiwara, and F. Robicheaux. "A proposal for laser cooling antihydrogen atoms", J. Phys. B **46**, 025302, 2013 (cit. on p. 102).

[194] I. Kozyryev and N. R. Hutzler. "Precision Measurement of Time-Reversal Symmetry Violation with Laser-Cooled Polyatomic Molecules", Phys. Rev. Lett. **119**, 133002, 2017 (cit. on pp. 102, 103, 107, 113).

[195] I. Kozyryev, L. Baum, K. Matsuda, and J. M. Doyle. "Proposal for Laser Cooling of Complex Polyatomic Molecules", ChemPhysChem **17**, 3641, 2016 (cit. on pp. 102, 103, 107, 113).

[196] T. A. Isaev and R. Berger. "Polyatomic Candidates for Cooling of Molecules with Lasers from Simple Theoretical Concepts", Phys. Rev. Lett. **116**, 063006, 2016 (cit. on pp. 102, 103, 107, 113).

[197] B. K. Stuhl, B. C. Sawyer, D. Wang, and J. Ye. "Magneto-optical Trap for Polar Molecules", Phys. Rev. Lett. **101**, 243002, 2008 (cit. on pp. 102, 103, 107, 113).

[198] I. Kozyryev, L. Baum, K. Matsuda, B. L. Augenbraun, L. Anderegg, A. P. Sedlack, and J. M. Doyle. "Sisyphus Laser Cooling of a Polyatomic Molecule", Phys. Rev. Lett. **118**, 173201, 2017 (cit. on pp. 102, 103, 107, 113).

[199] J. Söding, R. Grimm, Y. B. Ovchinnikov, P. Bouyer, and C. Salomon. "Short-Distance Atomic Beam Deceleration with a Stimulated Light Force", Phys. Rev. Lett. **78**, 1420, 1997 (cit. on p. 102).

[200] I. Kozyryev, L. Baum, L. Aldridge, P. Yu, E. E. Eyler, and J. M. Doyle. "Coherent Bichromatic Force Deflection of Molecules", Phys. Rev. Lett. **120**, 063205, 2018 (cit. on p. 102).

[201] X. Miao, E. Wertz, M. G. Cohen, and H. Metcalf. "Strong optical forces from adiabatic rapid passage", Phys. Rev. A **75**, 011402, 2007 (cit. on p. 102).

[202] J. Dalibard and C. Cohen-Tannoudji. "Laser cooling below the Doppler limit by polarization gradients: simple theoretical models", J. Opt. Soc. Am. B **6**, 2023, 1989 (cit. on p. 102).

[203] P. D. Lett, R. N. Watts, C. I. Westbrook, W. D. Phillips, P. L. Gould, and H. J. Metcalf. "Observation of atoms laser cooled below the Doppler limit", Phys. Rev. Lett. **61**, 169, 1988 (cit. on p. 102).

[204] N. J. Fitch and M. R. Tarbutt. "Principles and Design of a Zeeman-Sisyphus Decelerator for Molecular Beams", ChemPhysChem **17**, 3609, 2016 (cit. on p. 102).

[205] S. D. Hogan and F. Merkt. "Demonstration of Three-Dimensional Electrostatic Trapping of State-Selected Rydberg Atoms", Phys. Rev. Lett. **100**, 043001, 2008 (cit. on pp. 102, 104).

[206] S. D. Hogan, C. Seiler, and F. Merkt. "Rydberg-State-Enabled Deceleration and Trapping of Cold Molecules", Phys. Rev. Lett. **103**, 123001, 2009 (cit. on pp. 102, 104).

[207] R. Taïeb, R. Dum, J. I. Cirac, P. Marte, and P. Zoller. "Cooling and localization of atoms in laser-induced potential wells", Phys. Rev. A **49**, 4876, 1994 (cit. on pp. 102, 113).

[208] V. V. Ivanov and S. Gupta. "Laser-driven Sisyphus cooling in an optical dipole trap", Phys. Rev. A **84**, 063417, 2011 (cit. on pp. 102, 104, 113).

[209] V. V. Ivanov. "Continuous loading of an atom beam into an optical lattice", Opt. Commun. **324**, 258, 2014 (cit. on pp. 102, 113).

[210] M. Ben Dahan, E. Peik, J. Reichel, Y. Castin, and C. Salomon. "Bloch Oscillations of Atoms in an Optical Potential", Phys. Rev. Lett. **76**, 4508, 1996 (cit. on pp. 106, 111).

[211] S. R. Wilkinson, C. F. Bharucha, K. W. Madison, Q. Niu, and M. G. Raizen. "Observation of Atomic Wannier-Stark Ladders in an Accelerating Optical Potential", Phys. Rev. Lett. **76**, 4512, 1996 (cit. on pp. 106, 111).

[212] W. D. Phillips and H. Metcalf. "Laser Deceleration of an Atomic Beam", Phys. Rev. Lett. **48**, 596, 1982 (cit. on p. 108).

[213] C. S. E. van Ditzhuijzen, A. Tauschinsky, and H. B. van Linden van den Heuvell. "Observation of Stückelberg oscillations in dipole-dipole interactions", Phys. Rev. A **80**, 063407, 2009 (cit. on p. 109).

[214] A. Cooper, J. P. Covey, I. S. Madjarov, S. G. Porsev, M. S. Safronova, and M. Endres. "Alkaline-Earth Atoms in Optical Tweezers", Phys. Rev. X **8**, 041055, 2018 (cit. on p. 113).

[215] M. S. Safronova, S. G. Porsev, U. I. Safronova, M. G. Kozlov, and C. W. Clark. "Blackbody-radiation shift in the Sr optical atomic clock", Phys. Rev. A **87**, 012509, 2013 (cit. on p. 115).

[216] G. Grynberg and C. Robilliard. "Cold atoms in dissipative optical lattices", Phys. Rep. **355**, 335, 2001 (cit. on p. 118).

[217] N. P. Robins, C. Figl, S. A. Haine, A. K. Morrison, M. Jeppesen, J. J. Hope, and J. D. Close. "Achieving Peak Brightness in an Atom Laser", Phys. Rev. Lett. **96**, 140403, 2006 (cit. on p. 120).

[218] G. Cennini, G. Ritt, C. Geckeler, and M. Weitz. "Bose-Einstein condensation in a CO_2-laser optical dipole trap", Appl. Phys. B **77** 2003 (cit. on p. 120).

[219] V. Bolpasi, N. K. Efremidis, M. J. Morrissey, P. C. Condylis, D. Sahagun, M. Baker, and W. von Klitzing. "An ultra-bright atom laser", New J. Phys. **16**, 033036, 2014 (cit. on p. 120).

[220] D. M. Giltner, R. W. McGowan, and S. A. Lee. "Theoretical and experimental study of the Bragg scattering of atoms from a standing light wave", Phys. Rev. A **52**, 3966, 1995 (cit. on p. 120).

[221] R. Richberg and A. M. Martin. "Focusing of Bragg-outcoupled paraxial atom lasers", Phys. Rev. A **104**, 033314, 2021 (cit. on p. 120).

[222] G. D. McDonald, C. C. N. Kuhn, S. Bennetts, J. E. Debs, K. S. Hardman, J. D. Close, and N. P. Robins. "A faster scaling in acceleration-sensitive atom interferometers", EPL **105**, 63001, 2014 (cit. on p. 121).

[223] G. D. McDonald, C. C. N. Kuhn, S. Bennetts, J. E. Debs, K. S. Hardman, M. Johnsson, J. D. Close, and N. P. Robins. "80$\hbar k$ momentum separation with Bloch oscillations in an optically guided atom interferometer", Phys. Rev. A **88**, 053620, 2013 (cit. on p. 121).

[224] S.-w. Chiow, T. Kovachy, H.-C. Chien, and M. A. Kasevich. "102$\hbar k$ Large Area Atom Interferometers", Phys. Rev. Lett. **107**, 130403, 2011 (cit. on p. 121).

[225] D. S. Barker, N. C. Pisenti, B. J. Reschovsky, and G. K. Campbell. "Three-photon process for producing a degenerate gas of metastable alkaline-earth-metal atoms", Phys. Rev. A **93**, 053417, 2016 (cit. on p. 121).

[226]   N. P. Robins, A. K. Morrison, J. J. Hope, and J. D. Close. "Limits to the flux of a continuous atom laser", Phys. Rev. A **72**, 031606, 2005 (cit. on p. 122).

[227]   E. D. Black. "An introduction to Pound–Drever–Hall laser frequency stabilization", Am. J. Phys. **69**, 79, 2001 (cit. on p. 123).

[228]   B. Huang. "Linewidth Reduction of a Diode Laser by Optical Feedback for Strontium BEC Applications". MA thesis. University of Amsterdam, 2009 (cit. on p. 123).

[229]   T. Preuschoff, M. Schlosser, and G. Birkl. "Digital laser frequency and intensity stabilization based on the STEMlab platform (originally Red Pitaya)", Rev. Sci. Instrum. **91**, 083001, 2020 (cit. on p. 123).

[230]   "Red Pitaya DAC performance". https://ln1985blog.wordpress.com/2016/02/07/red-pitaya-dac-performance/. 2017 (cit. on p. 123).

[231]   "Gezelligheid - Wikipedia". https://en.wikipedia.org/wiki/Gezelligheid (cit. on p. 139).

List of publications

Publications with major contributions

Sisyphus Optical Lattice Decelerator [93]
Chun-Chia Chen, Shayne Bennetts, Rodrigo González Escudero, Florian Schreck, and Benjamin Pasquiou
Chapter 4 of this thesis. I was heavily involved in the investigation and data collection.

Continuous Bose-Einstein condensation [37]
Chun-Chia Chen, Rodrigo González Escudero, Jiří Minář, Benjamin Pasquiou, Shayne Bennetts, Florian Schreck.
Chapter 2 of this thesis. Together with Chun-Chia Chen performed the troubleshooting, investigation and data collection. Built part of the experimental apparatus.

Steady-state magneto-optical trap of fermionic strontium on a narrow-line transition [90]
Rodrigo González Escudero, Chun-Chia Chen, Shayne Bennetts, Benjamin Pasquiou, and Florian Schreck Chapter 3 of this thesis. Performed troubleshooting, investigation and data collection. Built required additional components of the experimental apparatus. Together with Benjamin Pasquiou wrote the manuscript.

Publications with minor contributions

Continuous guided strontium beam with high phase-space density [36]
Chun-Chia Chen, Shayne Bennetts, Rodrigo González Escudero, Benjamin Pasquiou, and Florian Schreck

Acknowledgements

The PhD track is a hard one with many challenges. I was very lucky to be surrounded by excellent people who helped me along the way. Without this support, finishing would have been almost impossible. Thanks to all of you.

Thanks to my supervisors Professor Florian Schreck and Dr. Benjamin Pasquiou. Florian is a brilliant and committed researcher, without him, none of the results presented here would have been possible. Benjamin not only has a deep understanding of all the aspects involving the experiment but he also is a great mentor. Working with him all of these years has been a pleasure. I wish him all the best in the future. One cannot say enough good things about Benjamin.

Thanks to the members of the strontium team at the University of Amsterdam, it has been a genuine delight working with you and I wish you the very best for the future. Special thanks to Francesca and Vincent. Francesca, as I write these pages, I cannot help but feel overwhelmed. I want to say so many good things about you I do not know where to start. You are the nicest person I have ever meet, a truly talented scientist, and a great friend. I am incredibly lucky to have met you. Thank you. Thanks Vincent for all of those lovely nights at Foeders. Hopefully we will come back soon, and we can enjoy many more beers. Yet I must thank you for much more than drunken nights. You listened to me, gave me advice, and patiently explained to me your research several times. I always felt comfortable talking with you and never regretted doing so.

Thanks to the microscope team. The microscope experiment and ours are in the same lab, so across these years I have worked very closely with them. Despite my horrible singing habit[2], we have a great atmosphere, with many (bad) jokes, and a lot of fun. Thanks Alex, Ivo, Thies, and Sergei for the great times. Not in the same room but just next door the RbSr team works. It is great to have them around. Thanks to all of you. Premjith you are a great researcher, a nice colleague, and a good friend. I am very happy you joined our group. Klaasjan you have a unique ability to cheer me up, you always have kind words and a smile. It has been a pleasure having you around all of these years. Mateusz you are a peculiar person with a strange sense of humor. The only one I know capable of doing

---

[2]*Wise man say only fools rush in . . .* ♩♪

worse jokes than me (Yes yes I know, a cactus is just a very aggressive cucumber). It is very nice to have you here. Thanks to Séverin for all of those evenings in the Brouwerij 't IJ.

Not next door but right across the corridor is the iqClock lab. Whether is sharing equipment, lending optics or electronics, and providing feedback you are always willing to help. You have helped me more times than I can count and you always done so with a smile. You guys are great and It is lovely to have you around. Thanks to all of you. Special thanks to Camila Stepan and Sheng. Thanks to the SrPAL team, without any of us so many amazing results would have been impossible. Thanks to Jiri, you are a very nice person and it is great to have you around.

Thanks to my colleagues at the Institute of Physics. The institute is very large so I had the luck of meeting many people. Special thanks to the Italian duo: Carla, *la donna malefica con el gato*, and Alvise, *il bello ragazzo*.[3] Thanks for those fun times, lovely dinners, and pleasant conversations. Carla thanks for patiently listening to me, for giving me advice, and pretending to enjoy my bacon-eggplant lasagna (I really thought this would work, also my lasagna is usually much better). Alvise I know you would not pretend to like that lasagna, yet it has been awesome having you around and I wish you the best in the future. Thanks to my roommate Sergio for the awesome dinner parties and the amazing nights at Soho. Thanks to Rebekka I really enjoyed those days when you were at home painting with Sergio it was very *Gezellig* [231] thanks for being there. Thanks to Enej, Neil, Yuan, and Oleksandr. I remember very fondly that snowball fight at 4 a.m. at Vincent's place. The posterior hangover, not so great.

Thanks to the atom-ion group. Henning, you are an awesome funny guy. Every time I see you I have an amazing time. Thanks Hendrik, Matteo, and Eleanor we have hung out so many times I lost count. Thanks to Professor Rene Gerritsma, you are an inspiring and charismatic academic and I am sure you will be even more successful in the future. Thanks to you and Professor Jook Walraven for allowing me to teach atomic physics to bachelor students. It was great to teach the brilliant minds that the university has to offer.

Thanks to all of my previous professors and supervisors. Thanks to my master thesis supervisor Dr. Sebastian Blatt. During my master thesis I learned more than in my whole Bachelor's degree combined. Thanks for spending that time with me. This knowledge helped me considerably during my PhD. Thanks to my high-school physics teacher Mercedes. You were an excellent teacher and I really appreciated that. Thanks to all of my university professors.

Thanks to my Spanish friends. Victor and Isma I really appreciated every time you came to visit. Especially the one time you came on my b'irthday. I was feeling down and you guys made me very happy. Jose, that impromptu bike trip to Spain was awesome, it helped

---

[3]Also thanks to google translate.

me relax and gave me so much energy. Overall I know I did a much better PhD because of this single trip. Thank you. Thanks also for helping me move. Probably should have used a truck and not just two bikes! Thanks Laura for coming, it was great. Come back soon! David and Juli I cannot overstress how happy I was to see you. It was great seeing you here, I will see you in Paris soon! Alfonso and Ignacio every time I go back it is a pleasure to meet you, have dinner, and enjoy some delicious wine. Alfonso thanks for listening to all my concerns. But especially thanks for being in the hospital these two years. I know you did an excellent job and you must be very proud. I know I can always trust you. Thanks to the lovely people I met in Munich. Thanks Annie, looking forward to your defense!

Thanks to the Dutch people, for being so open, inclusive and so delightfully weird. You have made me feel at home. Thanks to Marieke, my dutch teacher, for making the most boring thing (learning a language) actually fun. Thanks to the easylaughs community, you are an endless source of fun and humor. Thanks to Mathijs for going in this endless walks around science park with me and patiently listening to my rants.

The last two years have been particularly challenging for almost everyone because of the pandemic. However, for me, they have been some of the happiest of my life. This is all thanks to you Natacha, I love you. You have showed me that despite the stereotype of being cool rude and direct Dutch people can be sweet to. Thanks to all your family too, during these years, you have made me feel right at home. I truly appreciate that, thank you.

Gracias a mi madre por quererme de forma incondicional, a mi padre por ser tan pesado y a mi hermana por estar siempre cuando lo necesito. Se que siempre puedo contar con vosotros, os quiero mucho.

Finally, I would like to thank the reader, who undeterred by this thesis size has managed to read it in its entirety. I hope reading it for you, was as useful, interesting, and enjoyable as it was for me to write it.